Quantum dynamics in parametrically driven one-dimensional optical lattices

Dissertation

zur
Erlangung des Doktorgrades
der Naturwissenschaften
(Dr. rer. nat.)

der

Naturwissenschaftlichen Fakultät
der Universität Paderborn
vorgelegt von

USMAN ALI

Paderborn, 2025

Erklärung der Selbstständigkeit

Hiermit versichere ich, die vorliegende Arbeit selbstständig verfasst und keine anderen als die angegebenen Quellen und Hilfsmittel benutzt sowie die Zitate deutlich kenntlich gemacht zu haben.

Ort, Datum

Unterschrift

Vorsitzender der Promotionskommission: Prof. Dr. Cedrik Meier

Erstgutachter: Prof. Dr. Torsten Meier

Zweitgutachter: Prof. Dr. Martin Holthaus

Mitglied der Promotionskommission: Dr. Hendrik Rose

Zusammenfassung:

Das Zusammenspiel zwischen Bloch-Oszillationen und zeitperiodischer Modulation in räumlich inhomogenen optischen Gittern führt zu einer Vielzahl faszinierender dynamischer Phänomene. Durch theoretische Modellierung und numerische Simulationen zeigen wir zunächst, durch ein globales parabolisches Potential zusätzlich zu einem optischen Gitter eine räumliche Inhomogenität induziert, die traditionelle Bloch-Oszillationen verändert und neue Quanteneffekte wie Kollaps und Revival sowie dynamisches Tunneln von Wellenpaketen hervorruft. Zweitens offenbart diese Studie durch den Einsatz einer zeitperiodischen Modulation der parabolischen Falle weitere Modifikationen der Bloch-Oszillationen im inhomogenen System und eine Vielzahl unterschiedlicher dynamischer Effekte, die als Folge der Modulation auftreten. Die Floquet-Theorie bietet einen geeigneten Zugang, um diese Einteilchen-Bloch-Dynamik in getriebenen Gittern zu verstehen und vorherzusagen und ermöglicht tiefgehende Einblicke in die Kontrolle und die Manipulation von Quantenzuständen in maßgeschneiderten Potentiallandschaften.

Abstract:

The interplay between Bloch oscillations and time-periodic modulation in spatially-inhomogeneous optical lattices leads to a rich variety of fascinating dynamical phenomena. Through theoretical modeling and numerical simulations, we first demonstrate that the spatial inhomogeneity induced by a global parabolic trap over an optical lattice modifies traditional Bloch oscillations, introducing new quantum effects such as collapse and revival and dynamical tunneling of wave packets. Secondly, by employing a time-periodic modulation of the parabolic trap, this study reveals further modifications of Bloch oscillations in the inhomogeneous system and a rich variety of contrasting dynamical behaviors that emerge as a consequence of the modulation. Floquet theory provides a powerful framework for understanding and predicting these single-particle Bloch dynamics in driven lattices, offering deep insights into the control and manipulation of quantum states in spatially and temporally engineered potential landscapes.

List of Scientific Contributions

Peer-Reviewed Publications

1. **U. Ali**, M. Holthaus, and T. Meier, Wave packet dynamics in parabolic optical lattices: From Bloch oscillations to long-range dynamical tunneling, Physical Review Research **7**, 013141 (2025)
   - **Chapter 4** describes and extends the results of this publication.
2. **U. Ali**, M. Holthaus, and T. Meier, Floquet dynamics of ultracold atoms in optical lattices with a parametrically modulated trapping potential, New Journal of Physics **26**, 123016 (2024)
   - **Chapter 6** covers and extends the results of this publication.
3. **U. Ali**, M. Holthaus, and T. Meier, Chirped Bloch-harmonic oscillations in a parametrically forced optical lattice, Physical Review Research **5**, 043152 (2023)
   - **Chapter 5** is based on the results from this publication.

Conference and Workshop Presentations

1. **U. Ali**, M. Holthaus, and T. Meier, Controlled Dynamical Tunneling in Bichromatic Optical Lattices with a Parabolic Trap, DPG Spring Meeting of the Atomic, Molecular, Quantum Optics and Photonics Section (SAMOP), at University of Bonn, Germany, March 2025 (talk)
2. **U. Ali**, M. Holthaus, and T. Meier, Floquet dynamics of ultracold bosons in a parametrically driven optical lattice, Time Crystal Conference, at the Jagiellonian University Kraków, Poland, September 2023 (Poster)
3. **U. Ali**, M. Holthaus, and T. Meier, Floquet analysis of quantum dy- namics in periodically driven optical lattices, DPG School on Ultracold Atoms and Molecules, at the Physikzentrum Bad Honnef, Germany, August 2023 (Poster)
4. **U. Ali**, M. Holthaus, and T. Meier, Dynamics controlled by Floquet state occupation probabilities in a driven parabolic optical lattice, DPG Spring Meeting of the Atomic, Molecular, Quantum Optics and Photonics Section (SAMOP), at Leibniz University Hannover, Germany, March 2023 (talk)
5. **U. Ali**, M. Holthaus, and T. Meier, Super Bloch oscillations with a parametrically modulated parabolic trap, WE-Heraeus-Seminar on Ultracold Quantum Matter: Basic Research and Applications, at the Physikzentrum Bad Honnef, Germany, December 2022 (Poster)

Contents

Introduction

1

Since the advent of quantum theory, mankind has been eager to understand, control, and utilize quantum phenomena. Over the years, different approaches considering various paradigms have emerged, one of which involves cooling ensembles of gas to incredibly low temperatures. At room temperature, classical physics dominates the behavior of gases because thermal motion of particles outweighs any quantum effects. The large average distance between particles allows their quantum nature to be ignorable, and their statistical properties are well-described by the classical Boltzmann distribution. However, as temperature is lowered, quantum nature becomes manifest.

Quantum mechanics dictates that particles of the same type, i.e., atoms of a single element, are fundamentally identical and indistinguishable. This indistinguishability modifies the classical Boltzmann distribution into one of two quantum distributions: Fermi-Dirac for Fermions and Bose-Einstein for Bosons. Although this distinction is subtle at higher temperatures, it becomes significant in the ultracold regime. As the temperature approaches a critical point, the de Broglie wavelength of the atoms increases and becomes comparable to the distance between the particles. At this stage, quantum wave functions start overlapping and a striking phase transition occurs.

The phase transition corresponds to the emergence of Bose-Einstein condensate (BEC), a unique state of matter first predicted by Albert Einstein in 1925 [1] based on Satyendra Bose's earlier work on photon statistics [2]. In a BEC, a large number of particles condenses into the energetically lowest quantum state, exhibiting features of a single-coherent quantum entity. Individual particle wave functions merge giving rise to coherence at a macroscopic scale, which allows the collective behavior of particles to prevail. This fascinating state of matter allows the observation and study of quantum dynamics in ways that were previously unreachable.

Although the BEC state was predicted in the early days of quantum mechanics, achieving it experimentally was no small feat, instead it was the culmination of decades of work in atomic physics and optics. The key breakthrough that made this possible was the development of laser cooling and trapping techniques, which allow atoms to be slowed and confined using light. This approach has its genesis back in the Galilean era, when Kepler surmised that comets experience radiation pressure from the sun's radiation.

This idea was later formalized by James Clerk Maxwell, who mathematically calculated the radiation pressure in his famous theory of electromagnetism [3]. This was first experimentally explored at the beginning of 20th century by Lebedev who measured the effect of light force on a thin metallic plate [4]. Soon after, Nicols performed similar experimental investigations which led to the verification and measurement of the radiation pressure [5]. In the following years, Lebedev expanded this research to the exploration of radiation pressure on gas molecules [6]. Another significant leap occurred when Kapitza and Dirac theorized that a standing wave of light could act like a diffraction grating for electrons, further demonstrating the physical impact of light on particles [7]. At that time, the study of the interaction between light and atoms started gathering a lot of attention. In 1933, Frisch reported the first observation of the deflection of an atomic beam by resonant light from a sodium lamp [8]. This experiment was crucial in showing that the mutual exchange of momentum and energy between light and matter accounts for the mechanical action of radiation on atoms.

The momentum exchange takes place as the atoms absorb or emit photons, a concept that Einstein himself proposed in 1917 [9]. An atom absorbing photons gains momentum in the direction of the light beam, while the net momentum during emissions of photons is zero as they occur in random directions. Thus, the atom experiences a force, known as the spontaneous force or radiation pressure. Additionally, the dipole moment induced in the atom by the electric field of light provides another force that pushes the atom towards high or low intensity regions with a strength and direction that depend on the frequency of light. Atoms are drawn to regions of high intensity in the case of red-detuned light, while they are pushed towards low intensity regions for blue-detuned light.

These two fundamental forces, spontaneous force and the dipole force, have enabled both cooling and trapping of atoms. While the spontaneous force lowers the kinetic energy of atoms in subsequent events of absorption and emissions of light, thereby cooling them, the dipole force aids in confining the atoms to specific regions of space [10]. In 1970, Ashkin succeeded in trapping small particles using counter-propagating laser beams [11], thus giving access to confinement and control of atoms, molecules, nanoparticles, and miscoscopic biological entities. Later on, radiation pressure was used to cool neutral atoms [12] and ions [13] which caused a surge of activities in laser cooling and trapping.

Over the course of the following 20 years, it became feasible to cool atomic ensembles to temperatures just a few billionths of a degree above absolute zero as the laser cooling and trapping methods improved [14] and new techniques such as sisyphus and evaporative cooling were introduced. This outstanding accomplishment led to the first experimental realization of Bose-Einstein condensation in 1995 [15], when Cornell and his team created a BEC using a dilute rubidium atomic gas. Shortly thereafter, other teams were able to create BECs with several atomic species, such as sodium [16] and lithium [17]. These experiments validated the predictions made by Einstein and Bose around 70 years ago and marked the beginning of a new era in atomic, molecular, and optical physics.

The experimental realization of BECs in dilute alkali gases has also created new avenues for the investigation of many-body phenomena at a macroscopic scale. Unlike liquid helium [18], where strong interactions between particles obscure effects caused by condensation, the weak interactions in dilute gases set the stage for theoretical and experimental studies of matter waves. In such a scenario, the BEC is typically described by a single macroscopic wave function, representing the collective behavior and simplifying the analysis. This along with interatomic interactions treated as an additional potential leads to a particularly useful description, formalized as the Gross-Pitaevskii equation (GPE) [19, 20]. In the limits of minimal quantum correlations, the mean-field treatment of the GPE is viable in the weakly interacting regime. Moreover, the GPE does not take account for quantum fluctuations which are added as perturbations in accordance with the Bogoliubov theory [21]. Together, the GPE and Bogoliubov theory offer a robust framework for understanding the characteristic effects of BECs, forming the basis for much of the progress in quantum many-body physics.

In the early days of BECs, it was discovered that the inter-atomic interactions can be tuned using Feshbach resonances. An external magnetic [22,23] or optical field [24] fine-tunes the strength of the interactions up to an extent where they can be made stronger or essentially ignorable [25]. In the later scenario, the condensate displays characteristics identical to an ideal gas, giving access to a controllable-macroscopic quantum entity.

Soon after, it was also noted that loading the atomic condensate inside a periodic optical lattice potential influences the strength of inter-atomic interactions [25]. The depth of the periodic potential determines the way atoms are distributed within the lattice, which in turn affects the inter-atomic interactions. This initiated a search for methods to control interactions within these adjustable lattices, with the aim of tailoring atomic behavior and investigating various quantum effects.

Optical lattices are periodic potential structures formed by the interference of counter-propagating laser beams. Independent laser beams can be arranged in such a way that they interact at different angles, giving rise to various shapes and dimensionalities. The most frequently encountered lattices include one-dimensional, sinusoidal, square, and cubic configurations [26], as well as more advanced triangular [27], hexagonal [28], and kagomé [29] geometries. Optical lattices can also be generated by retro-reflection of laser beams. This technique, together with the application of a holographic mask on the reflected beam, has allowed the generation of nearly arbitrary potentials [30].

The scalability of optical lattices, which can trap large numbers of atoms in a well-defined periodic potential, makes them suitable for studying emergent phenomena arising from interactions between many particles [31]. Accordingly, models such as the (Fermi)-Hubbard model [32] and the Bose-Hubbard model [26] have been extensively investigated. Building on latter, a quantum phase transition from a superfluid to an insulating state, known as the Mott insulator transition, can be driven in the strong interaction regime. This transition, predicted theoretically by Fisher [33], was experimentally realized in a 3D lattice by M. Greiner and colleagues [26], providing a profound demonstration of interaction-induced localization in a controlled quantum system. Moreover, the Fermi-Hubbard model provides significant insights into fermionic correlations, antiferromagnetic ordering, and metal-insulator transitions.

Additionally, it was revealed that the inter-atomic interaction strength can be tuned significantly by the lattice depth, which is determined by the laser intensity, and additionally by employing Feshbach resonances [25]. Thus, ultracold atoms in optical lattices readily allow for the study of single-particle phenomena, as well as the effects of weak nonlinear interactions [34]. This level of control over the interactions and lattice dimensionality has enabled the exploration of noninteracting matter waves in reduced dimensions and the investigation of strongly correlated systems. Consequently, new insights and perspectives into quantum many-body physics and the nature of quantum dynamics in low-dimensional systems have been developed.

Probing the internal states of atoms with optical lattice fields, allows cold atoms to move in closed loops acquiring a geometric phase similar to the Aharonov-Bohm phase acquired by a charged particle in magnetic field. This technique marks the first creation of artificial gauge fields within optical lattices [35]. The generated strong magnetic fields have been used to study topological phases in optical lattices, including the realization of the Hofstadter model [36] and Chern insulator in cold atoms [37], where topologically protected edge states emerge. These advancements are pivotal in understanding topological materials and quantum Hall effects, as they enable the exploration of robust, dissipation-free edge transport. These new phases provide rich ground for exploring fundamental physics.

Moreover, optical lattice systems provide a high degree of isolation from external disturbances, which is crucial for observing delicate quantum effects that can be easily disrupted by environmental noise. As a result, phenomena such as quantum coherence, the generation of large-scale entanglement, and quantum measurements have been studied, all of which hold significant promise for applications in quantum computation and information science. Early work achieved controlled collisions to implement basic quantum gates, and creating Bell states showcased the potential of cold atoms as qubits [38]. More recent experiments have been scaled up to realize entanglement in atomic arrays and optical tweezers, which now routinely achieve defect-free atomic arrays and quantum entanglement in large ensembles [39,40]. These advancements have been further enhanced by the use of quantum gas microscopes, which allow for single-site resolution and precise manipulation of individual atoms within optical lattices [41,42]. With this level of control, researchers can directly image and manipulate atoms at distinct lattice sites, paving the way for quantum simulation and computation on the highly-controlled, single-atom level.

Ultracold atoms in optical lattices also play a crucial role in precision measurements. The high degree of control they enable makes them ideal for conducting high-precision measurements of fundamental constants [43,44] and testing the principles of quantum mechanics. Optical lattice clocks [45], which trap atoms in a lattice to reduce perturbations, are among the most accurate timekeeping devices that exist.

The periodic nature of optical lattices mimics crystalline structures found in solid-state physics, with the role of Bloch electrons played by ultracold atoms [46]. While lattice spacings in solids are generally measured in Angstroms, optical lattices feature lattice constants that are typically three orders of magnitude larger. Keeping in view, the atomic radii of commonly used atomic gases of few Angstroms and the size of an electron on the scale of one-tenth of a Fermi, the matter wave picture of de-Broglie is translated to hundred thousand times larger spatial scales. Moreover, in contrast to the usual many-body dynamics occurring in electronic systems on the extremely short time scales of femtoseconds, the time scale of the dynamics with ultracold atoms in optical lattices is on the order of milliseconds. Thus, ultracold atomic systems offer an almost one billion times longer interval for measurement and detection. Further, considering the recoil energy (E_R) of the commonly used Rubidium gas (Rb^{87}) subject to laser beam with wavelength $852nm$ amounts to 1.3×10^{-11} electron Volts (eV), and taking typical lattice depths of about $10E_R$, the use of ultracold atoms in optical lattices shifts down the usual eV-energy scale of solid state physics by no less than 10 orders of magnitude. Furthermore, one of the key advantages of optical lattices is their tunability. The depth, spacing, and geometry of these lattices can be precisely controlled by adjusting the intensity, wavelength, and polarization of the laser beams used to create them. This facilitates the realization of celebrated solid state phenomena like band structure [26], Anderson localization [47], Josephson junction [48], quantum Hall effect [49], Bose-glass phase [50], and Bloch oscillations [34].

Another freedom particular to optical lattices is the selective time-periodic modulation of the lattice parameters or the lattice geometry. The former is achieved by including specialized optical modulators, such as acousto-optic modulators, in the path of the optical laser beam, while the latter is accomplished either by adding non-static external potentials or by dynamically shifting the lattice phase. The phase-modulated optical lattice has enhanced the range of available synthetic fields by giving access to staggered magnetic fields and dynamical gauge fields and has also led to the realization of the topological Haldane model [51]. Also, amplitude-modulated optical lattices have been heavily investigated during the past two decades leading to the observation of superfluid to Mott-insulator transition in a driven system [52]. These twinkling lattices and shaken lattices also favor the exploration of driven dynamics and phenomena such as dynamical localization [53], chaos-assisted tunneling [54], and super-Bloch oscillations [55] have been observed. Recent experiments utilize simultaneous phase and amplitude modulation of optical lattices to optimally control dynamics, achieving effects such as chaos-assisted tunneling [56], the Hamiltonian ratchets [57], and efficient creation and manipulation of quantum states across the lattice band structure [58]. Thus, periodic driving has contributed to significant achievements, such as the creation of finite-momentum Bose-Einstein condensates and Floquet topological insulators, where new, exotic phases of matter emerge due to periodic modulation [27]. These periodically driven systems provide access to novel quantum states and facilitate studies of non-equilibrium dynamics, significantly enhancing our understanding of quantum matter under time-dependent driving. Research in this direction has advanced to employing driven bichromatic and multi-frequency lattices that induce disorder and, through dissipation processes, allow the exploration of fundamental questions in quantum statistics and thermodynamics. In these driven quasi-periodic optical lattices, topological pumping of bound states is also predicted to occur with the assistance of Bloch oscillations [59,60].

Bloch oscillation (BO) is a wave phenomenon manifesting in quantum systems with periodic potential and static field. This was first proposed by Felix Bloch in 1929 considering electrons in crystals [61]. During BOs electrons in solid crystals oscillate in the presence of a static external electric field. As per band theory, electrons in a periodic crystal lattice are quasi-particles forming bands of periodic energy structures which can be represented as a function of quasimomentum in the first Brillouin zone. An electron in the lowest band of the periodic lattice first accelerates due to the constant force of a static field and then oscillates with a periodic flipping of quasimomentum. In 1931, Zener inferred that the periodic modulation of quasimomentum manifests itself in terms of real-space oscillations. He also pointed out that the BOs display additional-decay features due to tunneling to higher bands as the strength of electric field increases [62,63]. The tunneling probability varies exponentially with the applied force indicating large variation in tunneling with small changes in field strength.

The oscillatory behavior in real space can be described by discrete energy levels known as Wannier-Stark ladders, as proposed by Wannier in 1960 [64]. In the tight-binding approximation, this results in Wannier-Stark states, which allow for an important analytical description of the system [65]. Additionally, the BOs are often discussed in terms of Wannier-Stark resonance states. Using perturbation techniques, this formalism also gives access to the study of the decay of BOs, where the energy spectrum becomes continuous [66].

Observing BOs in solid-state systems is quite challenging. Factors like scattering with impurities, defects, phonons, dielectric screening, dephasing, higher bands, and electron-electron interactions all disrupt the coherence necessary for realizing this oscillatory behavior. As a result, BOs are more easily detected in artificial highly-controlled environments. Specifically, these oscillations were first observed in artificial solids, so called semiconductor superlattices in 1992 [67], followed by observations of cold atoms in optical lattices in 1996 [68], and later in coupled optical waveguides in 1998 [69]. These developments highlight the increased interest in the phenomenon of BOs which has led to new perspectives, effects, and applications.

Building on the foundational concept of BOs, researchers have explored modified forms of these oscillations under various conditions such as breathing BOs [70], anharmonic BOs [71], and super-Bloch oscillations (SBOs) [55,72–76]. SBOs arise when an additional periodic driving field is applied to the system on top of the static field, creating a more complex modulation of the oscillatory behavior. In such cases, the periodic driving force interacts with the underlying BOs, resulting in oscillations that are typically larger in amplitude and have unique, tunable frequencies. Besides SBOs, the interaction between BOs and the modulation of field induces additional effects on top of BOs such as directed transport, ballistic spreading, and dynamical localization [73,74], enriching the possible applications and insights into the behavior of quantum particles in engineered potentials.

In short, BOs take the central stage in the exploration of various quantum phenomena, such as Landau-Zener tunneling, coherent oscillations or transport, breathing dynamics, dynamical localization, SBOs, collapse and revival dynamics, and chaotic oscillations.

Although SBOs occur under the modulation of the force, BOs have also been predicted for other related configurations, particularly those arising from the gradients of a parabolic potential [77] or even more complex higher-order gradients [78]. The parabolic potentials exist naturally in ultracold atomic systems where parabolic traps serve as an auxiliary element for confining and manipulating cold atoms. A one-dimensional periodic optical lattice becomes symmetrically curved when subjected to a global parabolic trap [79]. Thus cold atoms in the parabolic lattice experience a position-dependent force. However, in a specific region where the curvature of the parabolic potential varies sufficiently slowly, the force can be approximated as locally constant. Such a setting brings about dynamics very similar to BOs [79–81]. However, here the Bloch like dynamics dephases quite rapidly due to spatial variations in the strength of the force. As, during BOs, the wave packet only explores a limited number of lattice sites, the spatial variations remain small. In other words, the evolving wavepacket acquires different phases due to the anharmonic spectrum of the combined potential, leading to dephasing. The phase mixing leads to a decay of the coherent oscillations which is followed by periodic revivals as the phases re-accumulate.

In recent years, several experiments have investigated Bloch dynamics in periodic lattices subject to a parabolic trapping potential. This search has also led to the first ever experimental observation of BOs in real-space utilizing a deep optical lattice [77]. In the case with shallow optical lattices subjected to parabolic confinement, the multi-band structure becomes relevant. Such a regime has been considered for the production of coherent matter wave packets and the interband dynamics and collective oscillations were explored [82–84]. Similar setups also provide a cold atom analog of photoconductivity [85,86]. Further experiments in such a setting, demonstrate that by creating hybridized bands, time-dependent modulation of the parabolic lattice can generate ultrafast long-range transport across the lattice on top of BOs [87]. Another experiment reports that the phase of the external modulation brings about novel dynamics, which for one phase of the drive are fully coherent, while for another phase, exhibit a mixture of Bloch breathing and spreading dynamics [88]. This study also examines the observed contrasting dynamics using analytical theory specific to systems where a constant force is present, instead of the position-dependent force of a parabolic trap. Consequently, the model failed to describe all the observed effects. Although, these observations have attracted a lot of attention, a comprehensive analysis and further exploration remained elusive.

In this thesis, we examine Bloch dynamics in both static and periodically modulated one-dimensional parabolic optical lattices. Reviewing wave packet dynamics in parabolic optical lattices, we uncover long-range dynamical tunneling associated with BOs in these systems. By providing a detailed analysis of the driven dynamics, and introducing novel chirped Bloch-harmonic transport (CBHT) [79], we offer significant insights based on a generalized acceleration theorem. We solve the acceleration relation using appropriate approximations that yield transparent interpretations of the results. Beyond the semi-classical treatment of the acceleration theorem, we employ classical dynamical equations and phase space analysis to deduce the system's dynamics. We interpret the results using Floquet theory, which enables a deeper understanding and highlights important experimental implications. Experimental conditions and parameters relevant to these findings are also discussed.

In Chapter 2, we cover the foundational concepts of optical lattices by first analyzing how a single ultracold atom interacts with a classical standing wave field to generate a periodic optical potential. We then introduce essential topics such as Bloch and Wannier states, band structure, and the tight-binding approximation, setting the stage for our discussion of interacting atoms within the Bose-Hubbard model.

In Chapter 3, we introduce the single-particle dynamics in optical lattices, focusing primarily on BOs. We also describe driven dynamics, such as directed transport, oscillatory spreading, and dynamical localization. We then extend this discussion by examining how these dynamics build upon BOs, ultimately demonstrating the emergence of SBOs in a near-resonantly shaken optical lattice.

In Chapter 4, we analyze the impact of the spatial inhomogeneity in periodic lattices on BOs by considering examples of incommensurate and disordered lattices. We extend this discussion to include a spatially inhomogeneous force created by the parabolic trapping potential, which permits BOs in a specific region of lattice sites. While examining the effects of the spatial inhomogeneity on BOs, we also explore other related quantum dynamics. We analyze the spectral properties, which predict dynamical tunneling alongside with BOs. This dynamical tunneling is demonstrated through a phase space analysis of the quantum states and wave packet evolutions, including scenarios with on-site energy mismatch and interacting atoms. Some of these findings are described in our recently published paper [89].

In Chapter 5, we present the rich dynamics arising from the resonant driving of Bloch-like oscillations in a parabolic optical lattice. In this regime, we identify CBHT and highlight its differences from SBOs. Using a modified acceleration theorem, we explain the underlying CBHT dynamics and further demonstrate how these dynamics vary under different initial conditions.

These findings are also reported in our published paper [79].

In chapter 6, we analyze the complex phase-dependent Bloch dynamics in the driven parabolic optical lattice by using Floquet theory and classical dynamics of a driven pendulum. We discuss the construction and inspection of Floquet states, occupation probabilities of which reveal the emergence of distinct dynamics. A major part of these results is included in our published paper [90].

This thesis concludes in Chapter 7 with a summary of our main findings and an outlook on potential directions for future research.

Fundamentals

2

In this chapter, we discuss the fundamentals of optical lattices. We begin by discussing the basic theory of optical lattices, using the example of a single ultracold atom subjected to a classical standing wave field, which we solve in the interaction picture. Based on this analysis, we derive the explicit form of the optical potential experienced by the atom. Next, while describing the spectral properties of the single-particle system, we introduce Bloch states, Wannier states, the band structure, and the tight-binding approximation-topics that are crucial for our later analysis. We then consider interacting atoms in optical lattices and address the strong-interaction regime, which leads to the Bose-Hubbard model.

2.1 Optical Lattices

Optical lattices are ideal periodic potentials, offering exceptional precision and control for trapping and manipulating atoms which makes them a powerful tool for studying quantum phenomena and simulating complex physical phenomena. These potential fields are created through light-matter interactions, where the spatially-varying intensity of interfering laser beams induces a position-dependent potential for the atoms. This results in a periodic "potential landscape," with potential wells separated by distances on the order of the laser wavelength. The concept, originally proposed by Letokhov and Minogin in 1977 [91], has since become a central element in quantum simulation and ultracold physics research.

When an atom interacts with a laser field, the oscillating electric component of the laser light induces a dipole moment in the atom and shifts its energy levels through a phenomenon known as the optical Stark shift. The magnitude of this shift depends on the intensity and frequency of the laser relative to the frequency of a specific atomic transition. In a standing-wave configuration, the interference of laser beams produces a spatially varying light intensity, which gives rise to a periodic potential for the atoms. These aspects are described in detail in the following section.

2.1.1 Optical Stark Shift Potentials

Let us suppose a single ultracold atom is subjected to a classical standing wave field. The field is generated by counter-propagating laser beams along the x-axis, emerging from mirrors mounted in the yz-plane after retroflection of the incoming light, with parallel polarization. The Hamiltonian for the atom of mass M is given by

$$\hat{H}_A = \frac{\hat{\boldsymbol{p}}_x^2}{2M} + \sum_n \mathscr{E}_n |n\rangle\langle n|, \tag{2.1}$$

where $\hat{\boldsymbol{p}}_x$ represents the center of mass momentum operator for the atomic motion in the x-direction, and $|n\rangle$ denote the internal states of the atom with corresponding energies ε_n.

The interaction between the atom and the standing wave field is described in the dipole approximation as

$$\hat{H}_I = -\hat{\boldsymbol{d}}.\boldsymbol{E}(x,t), \tag{2.2}$$

with $\hat{\boldsymbol{d}}$ the dipole moment operator, and $\boldsymbol{E}$ representing the electric field associated with the standing wave. We express the electric field as

$$\boldsymbol{E}(x,t) = E_0 \sin(k_L x)(e^{-i\omega t} + e^{i\omega t})\boldsymbol{\varepsilon}_y, \tag{2.3}$$

where E_0 is the electric field amplitude, k_L is the laser wave vector, ω is the laser frequency and $\boldsymbol{\varepsilon}_y$ is the polarization vector of the lasers. The dipole operator can be expanded in the basis of the atomic states

$$\hat{\boldsymbol{d}} = \sum_{n,m} \boldsymbol{d}_{nm}|n\rangle\langle m|, \tag{2.4}$$

with $\boldsymbol{d}_{nm}$ denoting the matrix elements of the dipole operator.

Substituting the electric field and the dipole operator into the interaction Hamiltonian leads to the following expression

$$\hat{H}_I = -E_0 \sin(k_L x) \sum_{n,m} \left[(\boldsymbol{d}_{nm}.\boldsymbol{\varepsilon}_y)\, |n\rangle\langle m| \left(e^{-i\omega t} + e^{i\omega t} \right) \right]. \tag{2.5}$$

Further, it is assumed that the laser frequency is tuned close to an atomic transition, typically between the ground state $|n\rangle \equiv |g\rangle$ and an excited state $|m\rangle \equiv |e\rangle$. Under these conditions, solving the above equation in the rotating frame, the fast oscillating phases are neglected by applying the rotating wave approximation [92], and we arrive at

$$\hat{H}_I = -E_0 \sin(k_L x) \;\left[(\boldsymbol{d}_{eg}.\boldsymbol{\varepsilon}_y)\, |e\rangle\langle g| + \left(\boldsymbol{d}^*_{eg}.\boldsymbol{\varepsilon}_y \right) |g\rangle\langle e| \right]. \tag{2.6}$$

Introducing the space-dependent Rabi frequency,

$$\Omega(x) = 2E_0 \sin(k_L x)\, (\boldsymbol{d}_{eg}.\boldsymbol{\varepsilon}_y)/\hbar = 2\langle e|\hat{\boldsymbol{d}}.(E_0 \sin(k_L x)\boldsymbol{\varepsilon}_y)|g\rangle/\hbar, \tag{2.7}$$

which quantifies the strength of the atom-field coupling as a function of position. Equation (2.6) then simplifies to

$$\hat{H}_I = -\frac{\hbar}{2} \left[\Omega(x)|e\rangle\langle g| + \Omega^*(x)|g\rangle\langle e| \right]. \tag{2.8}$$

Taking into account a detuning $\delta = \omega_{eg} - \omega$ between the laser frequency and the atomic transition frequency, such that $|\delta| \gg |\Omega|$, the excited state is adiabatically eliminated [93]. In such a conservative interaction, the atomic ground state energy experiences a field-dependent shift, which can be calculated using second-order perturbation theory as

$$\mathscr{E}_g^{(2)} = \frac{|\langle e|\hat{H}_I|g\rangle|^2}{\hbar\delta} = \frac{\hbar|\Omega(x)|^2}{4\delta}. \tag{2.9}$$

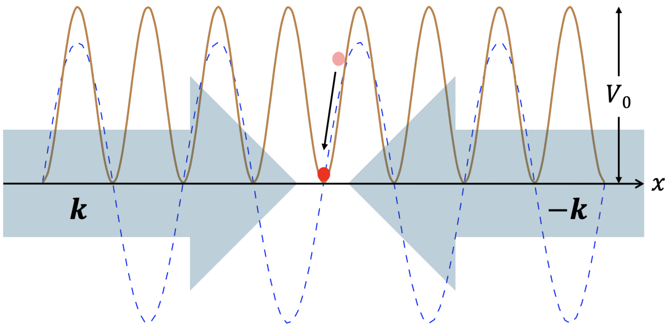

Figure 2.1: Schematic representation of a standing wave field formed by two counter-propagating laser beams, creating an AC Stark shift potential. The solid brown curve indicates the generated optical potential $V(x)$ experienced by the atom. The blue dashed curve represents the blue-detuned standing wave field, which confines the atoms towards its nodes. Note that the amplitudes are chosen arbitrarily; for a proper account of the amplitudes, we refer to the main text.

This is known as the AC Stark shift which is dependent upon the laser intensity I due to the relationship $I \propto \Omega^2$. Since the ultracold atom tends to remain in the ground state, the energy shift is equivalent to an optical potential experienced by the atom. This is schematically depicted in Fig. 2.1 where we have considered a blue-detuned standing wave field ($\delta < 0$) generated by the counter-propagating laser beams. The field periodically raises the ground state energy thereby creating potential wells at the nodes of the standing wave where the atoms are repelled by the potential. On the other hand, a red-detuned laser field ($\delta > 0$) lowers the ground state energy enabling attractive potentials which confine the atoms at the antinodes of the standing wave (not shown).

The periodic potential generated in the standing wave configuration has the form

$$V(x) = V_0 \sin^2(k_L x), \tag{2.10}$$

where V_0 denotes the depth of the optical potential, which is determined by the laser intensity I and the detuning δ. The lattice period $a = \pi/k_L$ is related to the laser wavelength λ by the relation $a = \lambda/2$.

Using additional laser beams intersecting at various angles allows for the creation of optical potentials in two or three dimensions. Furthermore, by adjusting the alignment and polarization of these beams, a wide range of intricate geometries can be formed within the periodic potential, greatly expanding the scope of possible experimental configurations and opportunities.

2.2 Single-Particle Physics

In optical lattices, cold atoms or even condensates can be experimentally tuned to behave as non-interacting particles by making inter-atomic interactions negligible. With this in mind, we first focus on the fundamental physics of non-interacting systems. We begin by exploring the single-particle physics in a one-dimensional periodic potential, leaving the effects of atom-atom interactions for later consideration. This approach allows us to establish a clear understanding of the basic principles before moving on to more complex many-body treatments.

2.2.1 Bloch's Theorem and Central Equation

Optical lattices complement conventional crystal structures by offering a means to create periodic potentials, where atoms, rather than electrons, interact with the potential. Neglecting the atom's internal degrees of freedom, many characteristics of optical lattices closely mirror those of traditional crystals, such as the periodicity of the potential landscape which leads to the formation of band structures. In this context, we build upon the work of Morsch and Oberthaler [94] and begin with a one-dimensional model of periodic potentials, which can be naturally extended to higher dimensions. The stationary Schrödinger equation for an atom in a potential $V(x)$ is given by

$$-\frac{\hbar^2}{2M}\frac{\partial^2\psi(x)}{\partial x^2}+V(x)\psi(x)=E\psi(x). \tag{2.11}$$

For the simple case where $V(x)=0$, the solutions to the above equation are plane waves. However, in the case of a periodic potential, $V(x+ma)=V(x)$ with lattice spacing a, the solution follows from the famous *Bloch's Theorem* [61, 95, 96]. By this theorem the eigenstates of a particle in a periodic potential can be expressed as a product of a plane wave and a periodic function

$$\psi_k^{(n)}(x)=e^{ikx}u_k^{(n)}(x), \tag{2.12}$$

where k is the crystal momentum and $u_k^{(n)}(x+a)=u_k^{(n)}(x)$ is periodic with the same period as the lattice. However, the Bloch states are quasi-periodic due to the modulation induced by the plane wave phase factor, and they are, in Bloch's own words, "de Broglie waves which are modulated in the rhythm of the lattice structure" [61]. The introduction of a periodic optical lattice transforms plane waves into Bloch states. Additionally, the presence of a periodic potential gives rise to forbidden energy zones, resulting from Bragg scattering of matter waves at the periodic potential. This phenomenon underpins the formation of the so-called *band structure* which is a fundamental concept in the study of wave packets in periodic potentials.

Using Fourier series, the Bloch states can also be written as

$$\psi_k^{(n)}(x)=e^{ikx}\sum_{l\in Z}c_{k,l}^{(n)}e^{ilGx}, \tag{2.13}$$

with the periodic functions $u_k^{(n)}(x)$ expanded as the sum of plane waves e^{ilGx} carrying momenta Gl, where l is an integer and $G=2\pi/a$ is the primitive reciprocal lattice vector.

In the same spirit, expanding the periodic potential $V(x)$

$$V(x)=\sum_{m\in Z}V_m e^{imGx}, \tag{2.14}$$

and using the Bloch states ansatz (2.13), the Schrödinger Eq. (2.11) recasts into a difference equation

$$\left[\frac{\hbar^2}{2M}(k+Gl)^2 - E_k^{(n)}\right] c_{k,l}^{(n)} + \sum_m V_m\, c_{k,l-m}^{(n)} = 0, \tag{2.15}$$

which is known as the central equation [95, 96]. This is a matrix equation with coupled coefficients for each k-value within the first Brillouin zone. The eigenvalues obtained by diagonalizing this equation, $E_k^{(n)}$, represent the energy bands labeled by the band index n.

The sinusoidal optical potential

When considering the case of a single atom in a one-dimensional sinusoidal optical lattice potential, as described in Eq. (2.10) in Section 2.1.1, the potential can be expressed as

$$V(x) = V_0\, \sin^2(k_L x) = \frac{V_0}{4}(2 - e^{2ik_L x} - e^{-2ik_L x}), \tag{2.16}$$

which includes only three terms, corresponding to the indices $m = 0, \pm 1$ in the Fourier expansion. Thus, in this case, the central equation reduces to

$$\left((k'+2l)^2 - \tilde{E}_{k'}^{(n)}\right) c_{k',l}^{(n)} - \frac{v_0}{4} c_{k',l-1}^{(n)} - \frac{v_0}{4} c_{k',l+1}^{(n)} = 0, \tag{2.17}$$

with $\tilde{E}_{k'} = E'_{k'} - v_0/2$ and using scaled variables. The energies E and potential depth V_0 are scaled in terms of the atomic recoil energy, $E_R = (\hbar k_L)^2/2M$, such that $E' = E/E_R$ and $v_0 = V_0/E_R$, and the quasimomentum k is scaled by the laser wave vector, expressed as $k' = k/k_L$.

The above equation is formally equivalent to the recursion relation satisfied by the Fourier coefficients of the Mathieu functions. Thus, the eigenvalue problem can be solved exactly by associating the undetermined coefficients with the Mathieu coefficients and the energies with the characteristic values of Mathieu functions [97]. In general, the characteristic values $\alpha_n(q)$ depend on the parameter q, which appears in the Mathieu equation and, in the present context, is related to the optical lattice depth by the relation $q = v_0/4$. Hence, the energies $E_{k'}$ are a function of the lattice depth.

The Mathieu functions can be expressed in the Floquet form, representing them as the product of periodic functions and exponential multipliers. These are known as Floquet solutions to the Mathieu equation [97], written as

$$\psi_n(x,\nu) = e^{i\nu x} \sum_{u=-\infty}^{+\infty} c_{u,\nu}^{(n)} e^{i2ux}, \tag{2.18}$$

where ν is the Floquet exponent. With the above solution, the characteristic values $\alpha_n(q,\nu)$ also become a function of ν, and the solutions strictly depend on whether ν is real or complex. The real ν constitute the so-called stable solutions, which form bands of eigenvalues. These bands are separated by gaps where no eigenvalue is obtained. Nonetheless, there exist unstable solutions in these domains for which ν is complex. These solutions are unbounded and non-

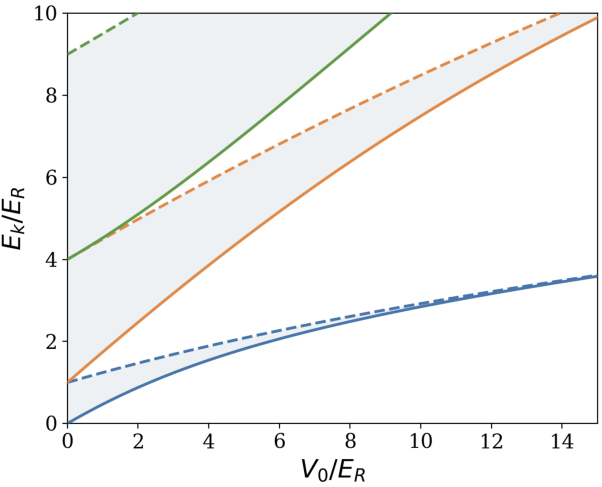

Figure 2.2: Energy spectrum for a one-dimensional optical lattice $V(x) = V_0 \sin^2(k_L x)$ as function of the lattice depth V_0. The lowest three energy bands are depicted, by the shaded regions between blue, orange and green curves representing the 1st-, 2nd-, and 3rd-band, respectively. Solid and dashed curves correspond to the modified Mathieu characteristic values a_0, a_2, a_4 and b_1, b_3, b_5, respectively. The eigenvalues are shifted by $v_0/2$, which modifies the characteristic values shown.

periodic, and therefore irrelevant to the lattice problem, so they are discarded here. Further, the integer values of ν correspond to periodic solutions, which for even values of ν are π-periodic and are 2π-periodic for odd values [97]. These solutions exist for certain values of α, designated as a_{2n} and b_{2n+1}, where $n = 0, 1, 2...$ is the band index. These outline the band edges where the lower edge emerge from the even functions and the upper edge is traced by the odd functions. For non-integer values of ν, there exist two independent solutions that span the space between the bands.

From Eqs. (2.13) and (2.18), it is clear that the Floquet exponent corresponds to the quasimomentum k in the lattice problem. Thus, the gaps are a hallmark of the band structure, where the real k values define the allowed bands. Taking into account the reduced Brillouin zone scheme, the quasimomentum k is restricted to the range $[-\pi/a, \pi/a]$. The values of k within this range span the corresponding energy bands. Moreover, $k = 0$ and $k = \pm\pi/a$ provides the lower and upper edges of the nth-band, alternating between each other.

While the Mathieu functions provide important knowledge on the spectral properties of the periodic optical lattice, instead of delving into their specifics, we numerically diagonalize Eq. (2.17) to obtain the eigenvalues and eigenstates.

The band spectrum is shown in Fig. 2.2 displaying the lowest three bands of the sine-squared lattice as a function of V_0. This shows that the band edges commensurate with the Mathieu characteristic values are shifted by $v_0/2$. Therefore, the band widths can be obtained by reading off the band spectrum. The band widths decrease by increasing the lattice depth and so the band gaps increases. Further, at high values of V_0, the band gaps become equally-spaced, similar to the energy spectrum of a harmonic oscillator. Thus, for such a deep lattice, the states are

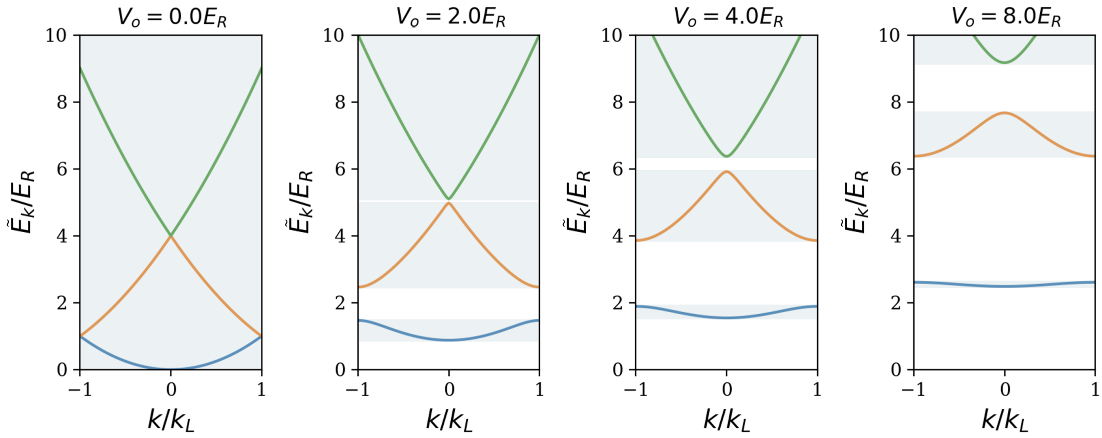

Figure 2.3: Energy band structure as a function of quasimomentum k within the first Brillouin zone. The band gaps increase with the lattice depth, as illustrated from left to right: the leftmost figure corresponds to zero lattice depth and the depth increases progressively in the subsequent figures in the right. The shaded regions highlight the band widths.

harmonic oscillator-like localized around each potential well of the periodic optical lattice.

Figure 2.3 presents the band structure as a function of quasimomentum. In the absence of the optical lattice, shown on the left, the eigenvalue Eq. (2.17) reproduces the dispersion curves of quadratically overlapping energies of the free particle. With the onset of a periodic optical lattice potential the overlapping energies start to form bands with subsequent band gaps. This is demonstrated in the subsequent figures in the right of first result. These figures also confirm the alternating lower and upper edges of the bands at $k/k_L = 0$ and ± 1.

Like eigen energies, the eigen states, corresponding to a particular band, depend upon the quasimomentum and have Bloch form. The eigenstate amplitude is given by the coefficients $c_{k,l}^{(n)}$ and the quasimomentum determines the plane wave envelope. In Fig. 2.4, we show the eigenstates associated with the edges of the ground band at $k = 0$ and π/a. This shows that the eigenstates corresponding to the band edges are stationary states, which for $k = 0$ are π-periodic, and for $k = \pm\pi/a$ are 2π-periodic [98]. Fig. 2.5 shows the probability density of these states for different lattice depths. This reveals that the probability density is concentrated around each lattice site inside the contiguous lattice wells. The result also exhibit that in the absence of the periodic lattice the eigenstates are plane waves extended in space and thus the probability density is constant. In the case of an optical lattice the eigenstates become localized in periodic lattice wells. The increased localization at higher depths of the periodic lattice is demonstrated. This effect is stronger for eigenstates with a finite quasimomentum, where the state at $k = \pi/a$ develops strong localization even at low lattice depths, due to its energetically high position within the band structure.

In Fig. 2.6, the eigenstates at the edges of the first band are shown for varying lattice depths. At low lattice depths, the states at $k = \pi/a$ are localized around the peaks of the optical potential. As the lattice depth increases, the eigenstates begin to develop two distinct peaks,

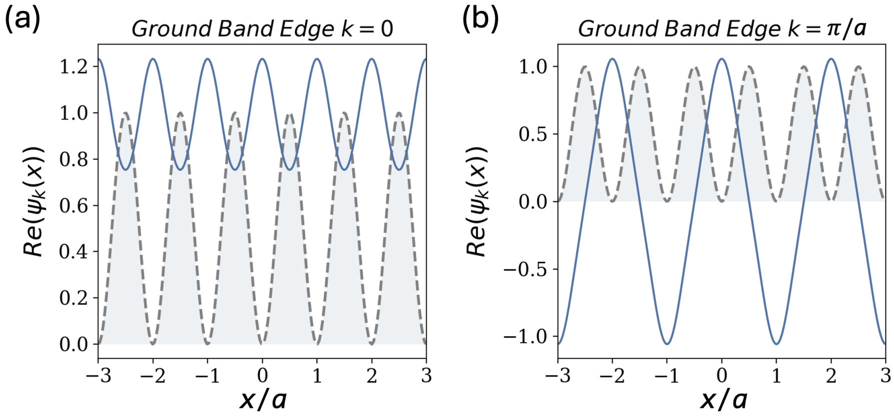

Figure 2.4: Real parts of the eigenstates corresponding to lower and upper edges of the ground band of the periodic optical lattice, at $k = 0$ (a) and $k = \pi/a$ (b), respectively. The shaded area and gray-dashed periodic curve depicts the optical potential.

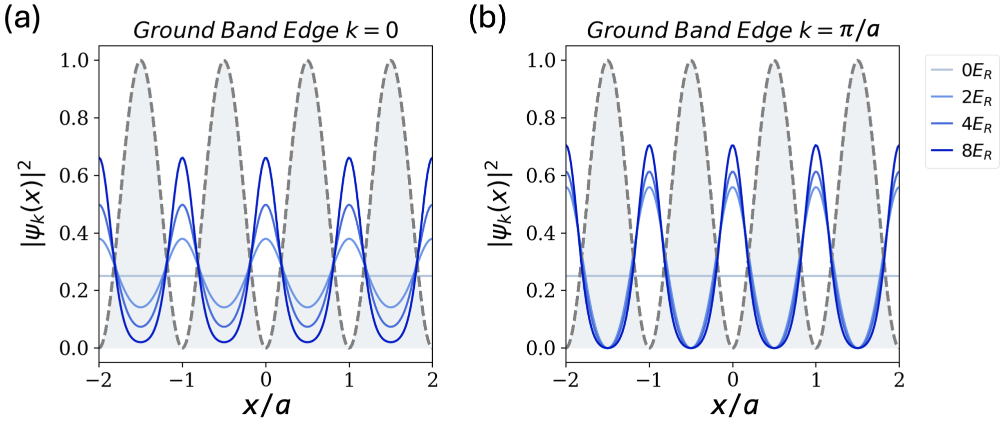

Figure 2.5: Absolute-squared values of the eigenstates corresponding to the lower and upper edges of the ground band at $k = 0$ (a) and $k = \pi/a$ (b), respectively, for different potential heights. The shaded area and gray-dashed periodic curve is shown to depict the optical potential. The eigenfunctions and optical potential in each case are normalized to unity.

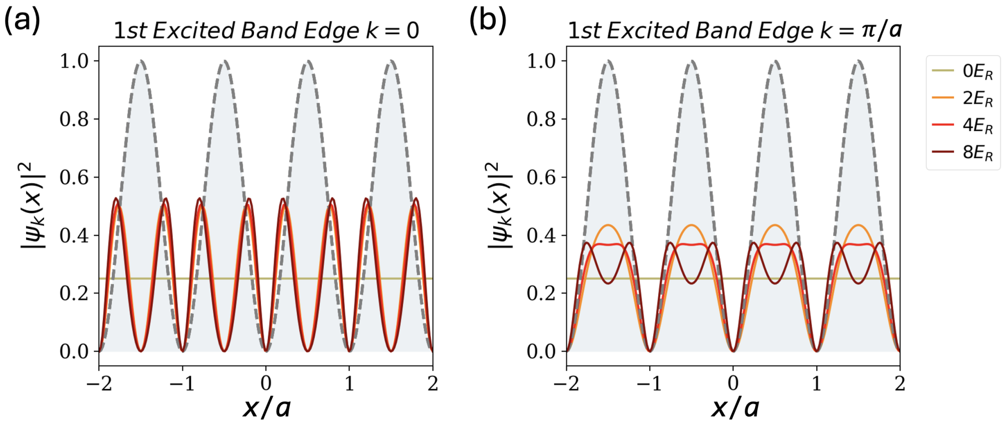

Figure 2.6: Absolute-squared values of the eigenstates corresponding to the upper and lower edges of the first excited band at $k = 0$ (a) and $k = \pi/a$ (b), respectively, for different potential heights. The shaded area and gray-dashed periodic curve depicts the optical potential. The eigenfunctions and optical potential in each case are normalized to unity.

which gradually grow in amplitude and shift toward the potential wells. At higher lattice depths, these states become localized along the sides of the potential wells.

The degree of eigenstate localization depends significantly on whether the state corresponds to the upper or lower band edge. For the first band, the upper edge is at $k = 0$ and states at this edge exhibit strong localization even at low lattice depths. This is evident in Fig. 2.6(a), where the eigenstates remain well-confined despite shallow lattice potentials. In contrast, for the lower band edge at $k = \pi/a$, strong localization develops more gradually as the lattice depth increases. This behavior is depicted in Fig. 2.6(b), showing a progressive confinement of the eigenstates as the lattice depth grows.

Similar to the trends observed across the lowest two bands, for the higher bands the probability density within the lattice varies across different positions. Accordingly, cold atoms loaded into an optical lattice distribute themselves based on the lattice depth, which also determines the wave packet localization and occupation of specific bands.

2.2.2 Wannier States

Wannier states are a complete, orthonormal set of maximally-localized wavefunctions, centered around lattice sites, that describe particles within a single energy band. They can be constructed as the superposition of all eigenstates corresponding to different k-values within a band, expressed as [99,100]

$$w^{(n)}(x - ja) = \frac{1}{\sqrt{L}} \sum_k \psi_k^{(n)}(x) e^{-ikaj}, \tag{2.19}$$

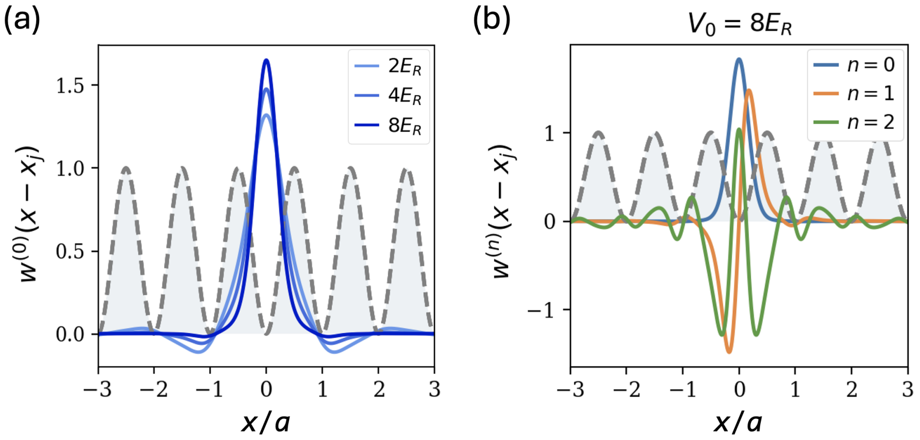

Figure 2.7: Ground band Wannier states at varying potential depths (a), together with Wannier states corresponding to the first two excited bands at a fixed potential depth $V_0 = 8E_R$ (b). The states are localized around $x_j = 0$. The shaded area and the gray-dashed periodic curve depicts the optical potential.

with the localized state centered around jth site in a lattice with L sites. Thus, Wannier states are related to the eigenstates of the periodic lattice through a Fourier transform and serve as an alternative yet equivalent basis. They provide a convenient basis for analyzing phenomena such as tunneling, particle interactions, and the effects of external forces.

The extent of localization of Wannier states is influenced by the lattice depth V_0 and varies significantly across different bands. At shallow lattice depths, corresponding to small V_0, Wannier states in the ground band are localized up to the extent that few lattice sites overlap. This reflects tunneling between adjacent wells. As the lattice depth increases, tunneling is suppressed, and Wannier states become sharply localized in individual wells. This transition illustrates the confinement of particles to single lattice sites with increasing lattice depth. Fig. 2.7(a) depicts this progression for the ground band Wannier states, illustrating the states increased localization as the lattice depth grows.

The localization of Wannier states also connect with the width of the associated band. Narrower bands lead to more localized Wannier states due to reduced energy spread. Conversely, broader bands yield less localized states. This dependence is evident in Fig. 2.7(b), which shows Wannier states for the lowest three bands at a fixed lattice depth. The ground band exhibits the highest localization, while higher bands display greater spatial extent, reflecting their wider bandwidths. Moreover, we note that the Wannier states for the ground band and second excited band are symmetric about their center, while the first excited band Wannier state has odd parity and is anti-symmetric. This reflects the underlying symmetry of the lattice potential inherited by Bloch states of the lower-lying bands.

2.2.3 Tight-Binding Model

The Wannier representation describes the most coveted positions of particles in a periodic lattice. The maximally-localized Wannier states delineate the distribution of the wavefunctions around fixed lattice sites. Restricting ourselves to the regime where the particle wavefunction in each well is not perfectly isolated but retains a finite overlap to the extent that the localized description of wavefunctions remains applicable. In such a regime, considering tunneling only between adjacent lattice sites and restricting the particle dynamics to a single band, the framework of constraints is commonly referred to as the tight-binding model. This framework is widely used to describe cold atom-lattice systems, even when the optical lattice is augmented by external potentials.

Assuming the cold atoms in the lowest band of the optical lattice and the external potential $V_{ext}(x)$ not strong enough to induce interband transitions, the atomic wavefunction can be expanded in terms of ground band Wannier states as

$$\Phi(x,t) = \sum_j \phi_j(t) w^{(0)}(x - ja). \tag{2.20}$$

The Schrödinger equation for a 1D optical lattice with the above wavefunctions leads to the following system of coupled linear equations, governing the time evolution of the amplitudes $\phi_j(t)$:

$$i\hbar \frac{\partial}{\partial t}\phi_j(t) = -J(\phi_{j+1}(t) + \phi_{j-1}(t)) + \varepsilon_j \phi_j(t), \tag{2.21}$$

with

$$J = -\int dx\, w^{(0)*}(x) \left(\frac{p^2}{2M} + V(x) \right) w^{(0)}(x - a), \tag{2.22}$$

and

$$\varepsilon_j = \int dx w^{(0)*}(x - ja) V_{ext}(x) w^{(0)}(x - ja) \approx V_{ext}(ja), \tag{2.23}$$

where J denotes the tunneling parameter between nearest-neighbor sites and ε_j represents the onsite energy shift caused by the external potential. In the context of the Wannier representation, Eq. (2.21) is referred to as the discrete Schrödinger equation or the tight-binding Schrödinger equation, which in the absence of an external potential leads to the energy dispersion relation $E_k = -2J\cos(ka)$.

Ground Band Tunneling Parameter

As discussed earlier, for a sine-squared lattice, i.e., $V(x) = V_0 \sin^2(k_L x)$, the solutions to the Schrödinger equation are Mathieu functions, and Mathieu characteristic values belonging to the periodic solutions provide the band edges. Therefore, one can use the asymptotic expressions for the even a_{2n} and odd b_{2n+1} characteristic values [97], which lead to the following expression for the bandwidths

$$\Delta^{(n)} \sim \frac{2^{3n+4}}{n!\sqrt{\pi}} \left(\frac{V_o}{E_R}\right)^{\frac{n}{2}+\frac{3}{4}} e^{-2\sqrt{\frac{V_o}{E_R}}} \left[1 - \frac{6n^2+14n+7}{16}\sqrt{\frac{E_R}{V_o}} + O\left(\frac{E_R}{V_o}\right)\right], \tag{2.24}$$

where $V_0 >> E_R$. Moreover, when using the definition of the Wannier states one can express the ground band tunneling parameter as

$$J = -\frac{1}{\sqrt{L}} \sum_k e^{ika} \int dx\, \psi_k^{(0)*}(x) \left(\frac{p^2}{2M} + V_o \sin^2(kx)\right) \psi_k^{(0)}(x) = -\frac{1}{\sqrt{L}} \sum_k E_k^{(0)}\, e^{ika}, \tag{2.25}$$

which leads to an analytical representation of ground band energy

$$E_k^{(0)} = -2J\cos(ka). \tag{2.26}$$

Therefore, the width of the ground band is related to the tunneling parameter as $\Delta^{(0)} = 4J$. Consequently, solving the expression (2.24) for the ground band, one has the ground band tunneling parameter, given by [101–104]

$$J \sim \frac{4}{\sqrt{\pi}} \left(\frac{V_o}{E_R}\right)^{\frac{3}{4}} e^{-2\sqrt{\frac{V_o}{E_R}}} \tag{2.27}$$

which is, thus, tunable through the optical lattice depth.

2.3 Bose-Hubbard Model

The present-day experimental advancements allow one to study ultracold atoms in optical lattices within the single-particle treatment, described above. However, regimes exist naturally where atom-atom interactions can be accessed. These interactions give rise to remarkable phenomena, such as the iconic superfluid to Mott insulator quantum phase transition [26]. This transition is captured by the Bose-Hubbard model, which describes interacting Bosons in a periodic potential. The model highlights the interplay between kinetic energy and interaction potential, central to the physics of strongly correlated Bosons. In the regime where the ratio of kinetic energy to interaction potential is large, Bosonic atoms delocalize across the lattice to minimize their kinetic energy, resulting in a superfluid phase characterized by a gapless excitation spectrum. Conversely, as the ratio approaches zero, on-site interactions suppress the tunneling, leading to the exponential localization of particles. Under these conditions, the energetically favorable configuration corresponds to an equal distribution of particles across the lattice sites, giving rise to the Mott insulating phase.

There has been extensive theoretical effort over the past decades to characterize the superfluid-to-Mott-insulator transition beyond these regimes. The challenge arises because the mean-field theory cannot be applied beyond the case of integer average filling factors and thus analytical solution become unachievable. Hence, various numerical techniques, such as renormalization group theories [33], strong-coupling expansions [105], and quantum Monte Carlo methods [106], have been developed. In particular, the density matrix renormalization group (DMRG) has been instrumental in providing deeper insights into the behavior of the system. More recently, advancements in hybrid numerical methods, such as the combination of tensor network techniques with Monte Carlo simulations [107] and machine learning algorithms [108] have further enhanced our understanding of the Bose-Hubbard model. These advanced methods have significantly contributed to the exploration of the Bose-Hubbard Hamiltonian.

Originally developed in the context of solid-state systems, the Bose-Hubbard model has also been applied to describe short correlation length superconductors [109], excitons in two-dimensional semiconductor lattices [110,111], Josephson junction arrays [112], the critical behavior of ^{4}He [113], and quantum phase transitions in photonic systems [114]. In the next subsection we review the basic properties of the Bose-Hubbard Hamiltonian.

Bose-Hubbard Hamiltonian

The many-body Hamiltonian of a cold spinless Bosonic gas subjected to an optical lattice potential can be formulated within the framework of a microscopic second-quantized description as

$$\begin{aligned}\hat{H} = \int dx\ \hat{\Phi}^\dagger(x)\left(-\frac{\hbar^2\nabla^2}{2M} +\ V(x)\right)\hat{\Phi}(x) + \int dx\ \hat{\Phi}^\dagger(x)V_{ext}(x)\hat{\Phi}(x)\\ +\frac{1}{2}\int dx\ dx'\ \hat{\Phi}^\dagger(x)\hat{\Phi}^\dagger(x')V_{atm}(x-x')\hat{\Phi}(x)\hat{\Phi}(x'),\end{aligned} \tag{2.28}$$

where $\hat{\Phi}^\dagger(x)$ is the Bosonic creation field operator, $V(x)$ is the periodic optical lattice potential, $V_{ext}(x)$ represents a weak external trapping potential that might be present and $V_{atm}(x)$ denotes a pseudo potential quantifying the inter-atomic interactions. It is known that for the ultracold atoms the inter-atomic interactions are dominated by the s-wave scattering length, a_s, and the interaction potential is given by

$$V_{atm}(x-x') = \frac{a_s h^2}{\pi M}\ \delta(x-x'). \tag{2.29}$$

with h denoting Planck's constant and M represents the mass of an atom.

As in the case of noninteracting atoms, where the single-particle wave function was expressed in Wannier functions, it is convenient to represent the field operators in the Wannier basis. With the considerations that the interaction potential is significantly smaller than the energy gap between the ground and first excited band and the strength of the external trapping potential is kept much smaller than the ground band width, the field operators can be expanded in terms of ground band Wannier functions as

$$\hat{\Phi}(x) = \sum_j \hat{a}_j w^{(0)}(x-ja), \tag{2.30}$$

with $\hat{a}_j$ the annihilation operator corresponding to site j in range $[-L/2, L/2]$. Using the above representation in Eq. (2.28) and restricting the atomic tunneling to nearest-neighbor sites, yields the Bose-Hubbard Hamiltonian

$$\hat{H}_{BH} = -J\sum_j(\hat{a}_j^\dagger\hat{a}_{j+1} + \hat{a}_{j+1}^\dagger\hat{a}_j) + \sum_j \hat{a}_j^\dagger\hat{a}_j\varepsilon_j + U\sum_j \hat{a}_j^\dagger\hat{a}_j^\dagger\hat{a}_j\hat{a}_j, \tag{2.31}$$

where the tunneling parameter J and the onsite energy ε_j correspond to the usual tight-binding parameters given in Eqs. (2.22) and (2.23) and U denotes the onsite interaction constant given by

$$U = \frac{a_s h^2}{\pi M}\int dx|w^{(0)}(x)|^4. \tag{2.32}$$

To calculate U, the Wannier states in Eq. (2.32) can be approximated using the Gaussian ground state of the local harmonic oscillator potential at a single lattice site, enabling the integral to be evaluated analytically which results in [46, 115]

$$U = \frac{4a_s}{h}(\pi M)^{\frac{1}{2}}(V_0 E_R)^{\frac{1}{4}}. \tag{2.33}$$

This relation offers the unique control of tuning the interaction strength through the optical lattice depth. In the next chapter, we first discuss the single-particle dynamics that arise when the external potential is assumed to be a potential that changes linearly with position, and describe the effects of interactions and time-periodic driving at a later stage.

Dynamics of Ultracold Atoms in Optical Lattices

3

Ultracold atoms in optical lattices can be described as matter-wave packets, resembling Bloch electrons in a periodic solid-state crystal. Consequently, the dynamics in a periodic optical potential are analogous to those of Bloch electrons. The ability to tune inter-atomic interactions to negligible strengths enables the realization of well-known phenomena such as Bloch oscillations, as well as more advanced super-Bloch oscillations, which so far have been observed exclusively in artificial crystals. These dynamics have been widely discussed for their potential to coexist with other familiar quantum dynamics and to give rise to novel quantum phenomena.

In this chapter, we introduce the reader to Bloch oscillations, super-Bloch oscillations, dynamical localization and other related dynamics.

3.1 Bloch Oscillations

Consider a single ultracold atom in a one-dimensional optical lattice, subjected to an external linear potential that tilts the lattice, creating a constant force (determined by the slope). The Hamiltonian is

$$H = \frac{p^2}{2M} + V(x) + Fx, \tag{3.1}$$

where F represents the constant force. Let us suppose that the lattice is described by Bloch bands and the time evolution of an initial wave packet comprising on a Bloch state $\psi_{k_0}^{(0)}(x, t = 0)$ is given by

$$\psi_{k_0}(x,t) = e^{-\frac{i}{\hbar}\left(\frac{p^2}{2M}+V(x)+Fx\right)t}\,\psi_{k_0}(x,0). \tag{3.2}$$

Introducing the translation in space by one lattice period, i.e., $x \to x + a$, gives

$$\psi_{k_0}(x+a,t) = e^{-\frac{i}{\hbar}\left(\frac{p^2}{2M}+V(x+a)+F(x+a)\right)t}\,\psi_{k_0}(x+a,0). \tag{3.3}$$

Employing the periodicity of the optical potential and the properties of Bloch states simplifies the above equation to

$$\psi_{k_0}(x+a,t) = \; e^{-\frac{i}{\hbar}\delta E\,t} e^{ik_0a}\psi_{k_0}(x,t), \tag{3.4}$$

with the energy shift $\delta E = Fa$, which corresponds to the phase shift $\delta Et/\hbar$. A 2π phase shift

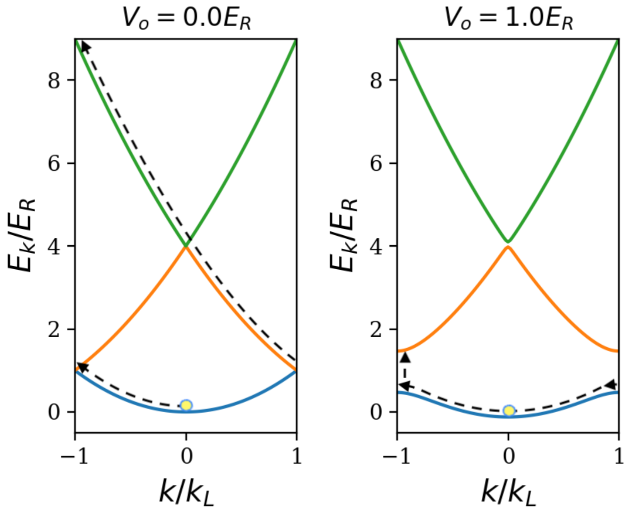

Figure 3.1: Schematic time evolution of a wave packet in the band structure of a sine-squared lattice under the influence of a constant force F: In the absence of a periodic optical lattice (left), the energy increases continuously without bound. In a periodic potential (right), energy gaps emerge between Bloch bands due to the band structure. The wave packet evolving in a particular band exhibits oscillatory motion, which decays when tunneling to higher band is not neglectable.

infers that the wave packet comes back to its initial position at time

$$T_B = \frac{2\pi\hbar}{Fa}, \tag{3.5}$$

known as the Bloch period. This provides an initial insight on the dynamics of wave packets effectuated by the constant force. The above result also relates the quasimomentum of the wave packet to the force as $k(t) = k_0 - Ft/\hbar$. This implies that the wave packet, with a slowly varying envelope centered around quasimomentum k, follows the classical acceleration law as the quasimomentum sweeps across a particular band. This semiclassical viewpoint on the coherent evolution of wave packets in periodic potentials is known as the acceleration theorem [70]. When the quasimomentum reaches the boundary of the first Brillouin zone, it inverts due to Bragg scattering, transforming the acceleration into a coherent oscillatory motion called Bloch oscillations (BOs). As during a BO, the energy shift is equal to the width of the band, therefore the available space L for the motion is given by [62]

$$L = \Delta/F, \tag{3.6}$$

where Δ is the bandwidth.

Figure 3.1 depicts the motion of the wave packet in k-space, for the propagation of the wave packet in the absence of a lattice (left) and with an optical lattice potential $V(x) =$

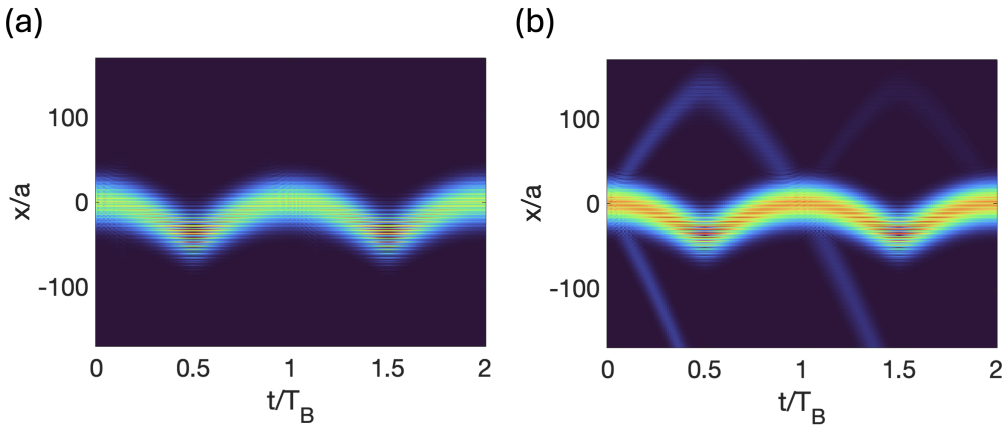

Figure 3.2: Absolute values of wave packet propagation in position space exhibiting center-of-mass Bloch oscillations in the ground band (left) and with including Landau-Zener tunneling to first-excited band (right). A Gaussian wave packet with width $\sigma = 10$ centered at $x_0 = 0$ and zero initial momentum is propagated. The system parameters are $F = 0.015\ (2V_0k_L)$, $V_0 = 1(E_R)$, $\hbar_{eff} = \sqrt{8E_R/V_0}$, and $a = 2\pi$.

$V_0\cos(2k_Lx)$ (right). The figure highlights the unbounded increase of the quasimomentum, upon the application of a force, in the lattice-free case and the periodic oscillations of the quasimomentum within a band when a periodic optical lattice is present. The band gaps play a significant role in the evolution of the wave packet and with a relatively small gap between the bands, the force couples the wave packet to the higher bands giving rise to Landau-Zener tunneling, by which the BOs decay. The tunneling probability is given by [116]

$$|T|^2 \approx \exp\left(\frac{\pi^2\Delta}{16Fa/E_R}\right), \tag{3.7}$$

which determines the transition rate [62]

$$R = \frac{1}{T_B}|T|^2. \tag{3.8}$$

The oscillatory dynamics in real space is shown in Fig. 3.2, which also exhibits Landau-Zener tunneling to higher-lying band. Fig. 3.2(a) displays the time evolution of the probability density of a broad Gaussian wave packet restricted to the ground band of the optical lattice. This reveals coherent center-of-mass BOs in the ground band. In Figure 3.2(b) Landau-Zener tunneling to first-exited band is revealed on top of BOs when all the bands of the periodic lattice are considered. The tunneling takes place initially and at each Bloch period. The tunneled fraction accelerates across the lattice covering large distances.

3.1.1 Group Velocity

Another quantity of interest for the wave packet propagation in periodic potentials is the group velocity. As noted by Jones and Zener (1934) [117], it is related to the energy dispersion relation via

$$v_g(t) = \frac{1}{\hbar}\frac{dE}{dk}. \tag{3.9}$$

This combined with the acceleration theorem provides a powerful approach to describe the Bloch dynamics. Considering the tight binding dispersion relation of a periodic lattice

$$E(k) = -2J\cos(ka), \tag{3.10}$$

the group velocity is

$$v_g(t) = \frac{2Ja}{\hbar}\sin(ka). \tag{3.11}$$

For a wave packet smoothly propagating in k-space; centered around the quasimomentum $k_c(t)$, the acceleration theorem reads

$$\hbar\dot{k_c}(t) = -F. \tag{3.12}$$

The group velocity evaluated at the quasimomentum $k_c(t)$ using perturbation method, yields

$$v_g(t) = \frac{2Ja}{\hbar}\sin(\omega_B t + k_c(0)a), \tag{3.13}$$

where $\omega_B = Fa/\hbar$ is the Bloch frequency. Integrating the above equation gives

$$x_c(t) = x_c(0) - \frac{2J}{F}\cos(\omega_B t + k_c(0)a), \tag{3.14}$$

which describes the center-of-mass BOs. This semi-classical approach is highly powerful in describing single-band tight-binding dynamics and later we will show that this approach works also well for the case of a time-modulated homogeneous force and even in a special case with a time-modulated spatially-inhomogeneous force.

3.1.2 Wannier-Stark Ladders

In order to further describe the phenomena occurring within a periodic lattice under the influence of constant external force, it is important to introduce the concept of the Wannier-Stark ladder. This concept first proposed by Wannier in 1960 [64] and it subsequently sparked a prolonged debate, the details of which are reviewed in [118, 119]. Though the Bloch dynamics are often described using band theory, the presence of an external force breaks the translational symmetry of the system, making the band picture inapplicable. Instead, a different form of quantization emerges, known as the Wannier-Stark ladder. In this formulation the solutions

$\varphi_n(x)$ of the Schrödinger equation

$$\left(\frac{p^2}{2M} + V(x) + Fx\right)\varphi_n(x) = E_n\varphi_n(x), \tag{3.15}$$

under translation $x \to x - la$, solve the same equation

$$\left(\frac{p^2}{2M} + V(x) + Fx\right)\varphi_n(x - la) = (E_n + laF)\varphi_n(x - la), \tag{3.16}$$

with eigen energies $E_{n,0}$ shifted to $E_{n,l} = E_{n,0} + laF$ forming an equispaced ladder-like structure of discrete energy levels. The wavefunctions $\varphi_{n,l}(x) = \varphi_n(x - la)$ are commonly known as Wannier-Stark states. This description readily allows an explanation of the dynamics in the titled periodic potential even at high strengths of the constant force. Despite, we restrict the discussion to the weak force case and describe the dynamics without considering the Landau-Zener tunneling and other decay processes. Thus, the index n representing the higher-lying ladders is suppressed.

Let us consider a wave packet expansion in terms of Wannier-Stark states

$$\Phi(x,t) = \sum_l c_l(t)\varphi_l(x), \tag{3.17}$$

which inserted into the Schrödinger equation gives

$$i\hbar\sum_l \dot{c}_l\varphi_l(x) = \sum_l (E_0 + laF)\, c_l\varphi_l(x). \tag{3.18}$$

The energies E_0 only contributes a global phase to the time evolution and is therefore omitted. Further assuming that the lattice is large enough to maintain the global translational symmetry and that the Wannier-Stark states are well-localized within individual wells of the tilted lattice at sites l, it follows that adjacent eigenstates of the Hamiltonian are effectively identical. This ensures that the orthogonality condition holds and the state $\varphi_j(x)$ is orthogonal to its left eigenstate $\varphi_l(x)$ for $l \neq j$. Thus, projecting the above equation with $\varphi_j^*(x)$ and integrating results in [120]

$$i\hbar\dot{c}_j = jaFc_j. \tag{3.19}$$

The above simple integrable model captures important features of the dynamics. To bring these to surface we decompose the coefficients into time dependent amplitudes and phases

$$c_j = \sqrt{\rho_j}\, e^{i\phi_j}, \tag{3.20}$$

which leads to

$$i\hbar\dot{\rho}_j - 2\hbar\dot{\phi}_j\rho_j = 2jaF\rho_j. \tag{3.21}$$

Separating real and imaginary parts and integrating yields the following solution for the amplitude

$$\rho_j(t) = \rho_j(t = 0), \tag{3.22}$$

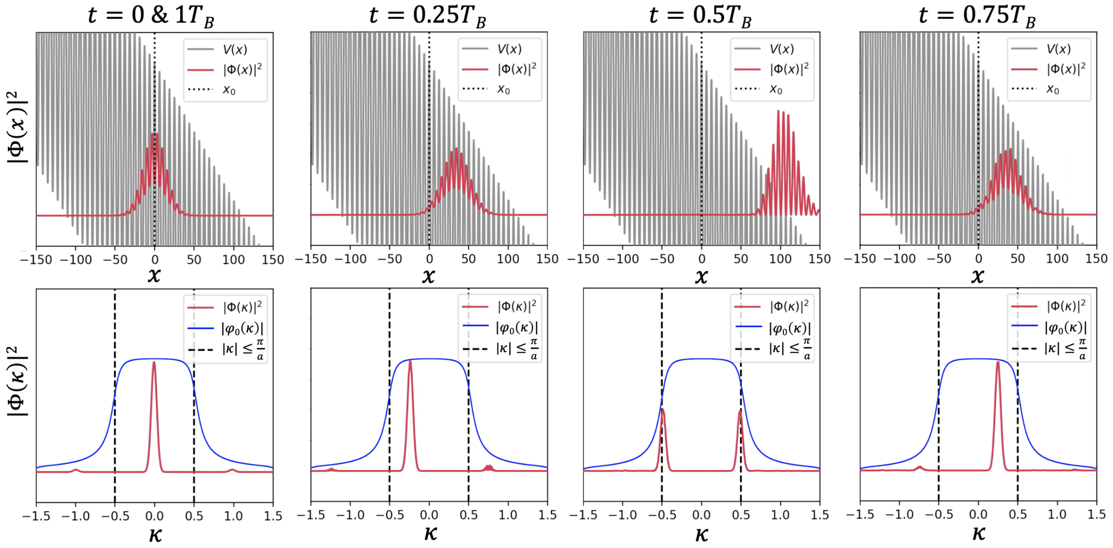

$t = 0$ & $1T_B$ $t = 0.25T_B$ $t = 0.5T_B$ $t = 0.75T_B$

Figure 3.3: Absolute-squared values of wave packet evolution in real and momentum space. Coherent center-of-mass Bloch oscillations for an initial broad Gaussian wave packet are shown. The dotted line mark the initial mean position of the wave packet and dashed line outline the boarders of the 1st Brillouin zone. The gray curves depict the periodic potential and blue curve shows the absolute value of Wannier state in momentum space.

and for the phase

$$\phi_j(t) = -j\frac{\delta Et}{\hbar}, \tag{3.23}$$

with the energy shift $\delta E = Fa$. These results explain the constant amplitude during center-of-mass BOs and the time-dependent phase shift originating from the energy shift at the respective site j.

A deeper understanding can be gained by examining the dynamics of the wave function in momentum space. This can be achieved with the approximate solutions derived earlier. Keeping in view, the spatial invariance of Wannier-Stark states, the Wannier-Stark states in the momentum space are represented as

$$\varphi_j(\kappa) = e^{-ij\kappa a}\varphi_0(\kappa), \tag{3.24}$$

where κ is the wave vector related to the true momentum. Hence, the time evolution of wave packet in momentum space is

$$\Phi(\kappa, t) = \varphi_0(\kappa)\sum_j \sqrt{\rho_j}e^{-ij(\kappa+Ft/\hbar)a}, \tag{3.25}$$

which can be expressed as

$$\Phi(\kappa, t) \sim \varphi_0(\kappa)\tilde{C}(\kappa + Ft/\hbar), \tag{3.26}$$

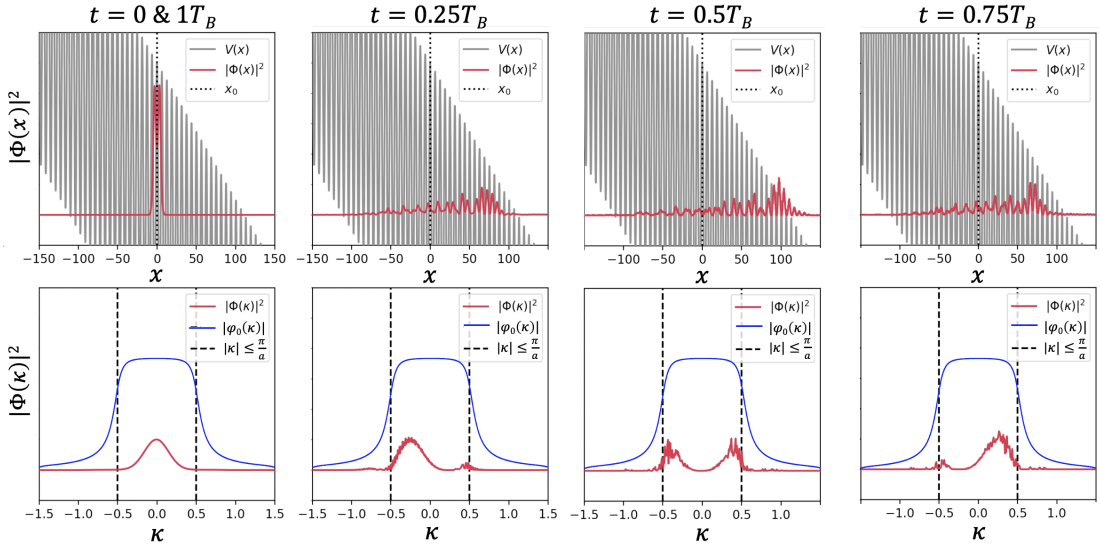

Figure 3.4: Absolute-squared values of wave packet evolution in real and momentum space. Bloch breathing oscillations for an initial sharply localized wave packet are shown. The dotted line mark the initial mean position of the wave packet and dashed line outline the boarders of the 1st Brillouin zone. The gray curves depict the periodic potential and blue curve shows the absolute value of Wannier state in momentum space.

where we have neglected a global phase. Here, $\tilde{C}(\kappa)$ represents the discrete Fourier transform of the real-space amplitude ρ_j. This evaluated at $\kappa + Ft/\hbar$ provides the time evolution of the wave packet in quasimomentum-space which remain under a time-independent complex function $\varphi_0(\kappa)$. The function $\tilde{C}(\kappa)$ is periodic in κ-space, meaning that $\tilde{C}(\kappa + j) = \tilde{C}(\kappa)$. Consequently, $\tilde{C}(\kappa + Ft/\hbar)$ is also periodic in time with a period equal to the Bloch period. For a broad Gaussian distribution with the amplitudes ρ_j, the discrete Fourier transform results in a comb function with peaks located at $\kappa = j$ [120]. These peaks, representing the wave packet in momentum space, evolve linearly in time under an envelope function given by $\varphi_0(\kappa)$. The comb and envelope function are illustrated in Fig. 3.3 and Fig. 3.4, where the absolute-squared value of the wave packet evolution is shown in real and momentum space along with the absolute value of the momentum space Wannier-Stark state $\varphi_0(\kappa)$. The periodic evolution of the wave packet in momentum space under an envelope function manifests as periodic BOs of the wave packet in real space.

We have seen already that the amplitude of a broad Gaussian wave packet which moves smoothly across the tilted lattice remains almost undisturbed. Although the amplitude of the momentum peaks changes under the envelope function, it remains almost constant as the wave packet translates through the Brillouin zone. The momentum space description also suggests that a sharply localized wave packet in real space would breathe due to a large spread of the wave packet density in momentum space. In such a case, the wave packet expectation values vanishes while the width oscillates periodically in time. These width oscillations are termed

Bloch breathing oscillations or Bloch breathing modes. The time evolution of the width and the expectation values can be obtained analytically. However, instead of delving deeper into this topic we only show the wave packet dynamics which we obtain numerically.

To demonstrate the two kind of Bloch motions, we show in Fig. 3.3 and Fig. 3.4 the real and momentum space dynamics by taking an initial Gaussian wave packet. Fig. 3.3 illustrate that for a broad Gaussian wave packet the dynamics is given by coherent center-of-mass BOs. In this motion, the wave packet accelerates in the direction of the force. As the momentum wave packet reaches the edge of Brillouin zone, its probability drops significantly while it increases at the opposite edge. Thus, with the inverted sign of momentum, the wave packet changes direction in real space and it again accelerates towards its outset. This motion is repeated with negligible width variations.

The wave packet evolution shown in Fig. 3.4 exhibit that instead of coherent center-of-mass motion a sharply-localized Gaussian wave packet performs periodic breathing motion in which the wave packet first expands and then it shrinks. The wave packet expands to the localization length at times equal to half of the Bloch period, then it shrinks returning to its original shape. The large spread of wave packet in momentum space causes the total density to explore opposite directions giving rise to breathing.

3.2 Driven Dynamics

Optical lattices also enable one to design time-periodically modulated potentials. The simplest setup one can implement is an oscillating periodic lattice driven by a time-periodic potential

$$V_{ext}(x,t) = Fx\sin(\omega t + \phi). \tag{3.27}$$

This potential imparts an oscillating force

$$F(t) = F\sin(\omega t + \phi), \tag{3.28}$$

which causes the quasimomentum to oscillate according to

$$\hbar\dot{k}_c(t) = -F(t). \tag{3.29}$$

As discussed in the previous chapter, an external linear potential, in general, makes the band picture inapplicable. However, the time-periodically driven force and particular resonances in the case with a constant force restores the band structure such that the driving compensates for the energy offset between neighboring wells in the lattice [121].

Thus, above Eq. (3.29) suggests that depending on the initial phase of the driving force, the oscillations of the quasimomentum are either uniform around the center of the Brillouin zone or shifted to one side. This is equivalent to a vanishing cycle-average momentum or a finite momentum experienced by the wave packet over each cycle. The latter results in a coherent directed transport along with small periodic oscillations.

In order to demonstrate these effects, we consider a single atom in a periodic optical lattice with atomic tunneling limited to nearest neighbors and the dynamics restricted to the low-

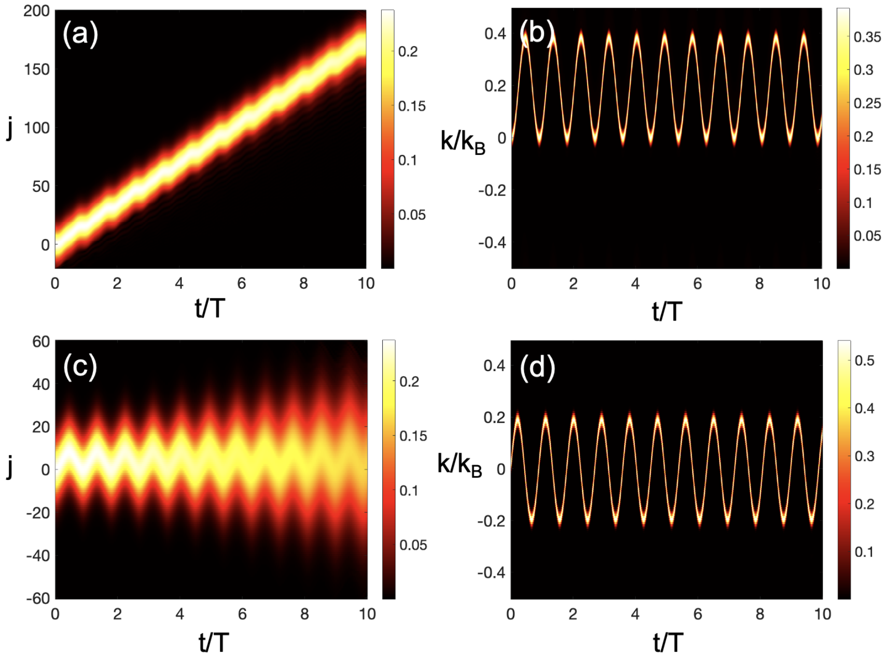

Figure 3.5: Absolute values of the wave packet evolution in real and quasimomentum space. Spreading and transport dynamics in the oscillating tight-binding lattice are shown for $\phi = 0$ ((a) and (b)) and $\phi = -\pi/2$ ((c) and (d)), respectively. A broad Gaussian wave packet with width $\sigma_0 = 10$, initial momentum $k_0 = 0$, and initial position $j_0 = 0$ is evolved. The system parameters are $J = 1.0E_R$, $Fa = 0.605E_R$, and $\hbar\omega = 0.5E_R$.

est band. The single-band tight-binding lattice in the presence of a time-periodic potential is described by the Hamiltonian

$$\widehat{H} = -J \sum_{j=-\infty}^{\infty} (|j+1\rangle\langle j| + h.c) + F(t)a \sum_{j=-\infty}^{\infty} j|j\rangle\langle j|, \tag{3.30}$$

where $|j\rangle$ represents the Wannier states localized at position $x = ja$. The initial state we choose as a broad Gaussian wave packet

$$|\Phi(t=0)\rangle = \sum_j \frac{1}{\sqrt{\sigma_0\sqrt{\pi}}} e^{-\frac{(j-j_o)^2}{2\sigma_0^2}} e^{-ik_0(j-j_o)}|j\rangle, \tag{3.31}$$

where j_0 represents the initial mean position, k_0 denotes the initial quasimomentum, and σ_0 corresponds to the wave packet width. We then solve the Schrödinger equation with Hamiltonian (3.30).

When considering the tight-bind dispersion relation for the ground band of the periodic lattice $E(k) = -2J\cos(ka)$, the effective dispersion relation for the driven system is given as [73,74]

$$\varepsilon(k) = \frac{1}{T}\int_0^T dt E(k_c(t)), \tag{3.32}$$

with $T = 2\pi/\omega$ representing the period of the drive. This leads to

$$\varepsilon(k) = -2J\mathcal{J}_0\left(\frac{Fa}{\hbar\omega}\right)\cos\left(k_c(0)a + \left(\frac{Fa}{\hbar\omega}\right)\cos(\phi)\right), \tag{3.33}$$

where $\mathcal{J}$ represents a Bessel function of the first kind. The above energy dispersion provides the average group velocity

$$\bar{v}_g = \frac{\partial\varepsilon}{\partial k_c(0)} = \frac{2Ja}{\hbar}\mathcal{J}_0\left(\frac{Fa}{\hbar\omega}\right)\sin\left(k_c(0)a + \left(\frac{Fa}{\hbar\omega}\right)\cos(\phi)\right). \tag{3.34}$$

Taking $k_c(0) = 0$, the above equation reveals a vanishing of the average group velocity for $\phi = \pm\pi/2$ and obtaining a constant value, i.e., $\frac{2Ja}{\hbar}\mathcal{J}_0\left(\frac{Fa}{\hbar\omega}\right)\sin\left(\frac{Fa}{\hbar\omega}\right)$, for $\phi = 0, \pm\pi$. This represents periodic oscillations at $\phi = \pm\pi/2$ and oscillatory directed transport for $\phi = 0, \pm\pi$. These dynamics are shown in Fig. 3.5 in both real and quasimomentum space. Figure 3.5(a) exhibits the directed transport on top of periodic oscillations for $\phi = 0$. These dynamics are related to periodic oscillations of quasimomentum, displayed in Fig. 3.5(b). The wave packet density exploring the quasimomentum values on one side of the Brillouin zone describes the accelerated transport. In Fig. 3.5(c) and (d), the dynamics obtained at $\phi = -\pi/2$ are shown. Fig. 3.5(c) also unveils a slow oscillatory spreading of wave packet on top of periodic oscillations. This spreading motion develops gradually as the wave packet oscillates in real and quasimomentum space. The dynamics of the quasimomentum are displayed in Fig. 3.5(d). The spreading motion is related to a constant band dispersion and an effective tunneling for $\phi = \pm\pi/2$, while the average group velocity becomes zero. We also note that both the transport and spreading reduces as the wave packet performs large amplitude oscillations inside the Brillouin zone at a stronger driving force.

3.2.1 Dynamical Localization

At specific values of the ratio between the driving strength and frequency, corresponding to the zeros of the Bessel function $\mathcal{J}_0$, both spreading and transport cease entirely. This phenomenon, known as dynamical localization characterizes a regime where tunneling is coherently suppressed and is linked to the band collapse signified by Eq. (3.33) [53]. Band collapse results in a complete decoupling between the lattice sites, with eigenfunctions becoming strictly localized onto individual sites. From a physical perspective, the application of a time-periodic drive induces coherence in the system, which in turn suppresses or can even eliminate tunneling between neighboring sites.

Figure 3.6 demonstrates the dynamical localization for the same Gaussian wave packet as employed in Fig. 3.5. It can be seen in Fig. 3.6(a) that the wave packet performs periodic oscillations in real-space even though the quasimomentum-space dynamics in Fig. 3.6(b) imply a cycle averaged momentum. Similarly, the slow oscillatory spreading is shown to die out com-

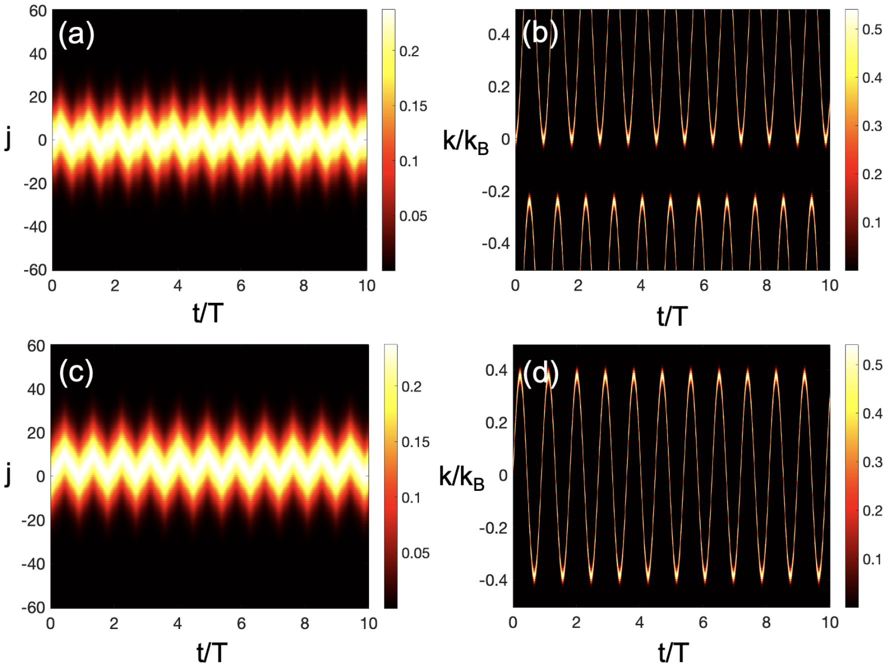

Figure 3.6: Absolute values of the wave packet evolution in real and quasimomentum space. Dynamical localization in the oscillating tight-binding lattice are shown for $\phi = 0$ ((a) and (b)) and $\phi = -\pi/2$ ((c) and (d)), respectively. The initial state and the system parameters remain the same as in Fig. 3.5, except that the wave packet, in this case, experiences a relatively stronger force $Fa = 1.2E_R$.

pletely in Fig. 3.6(c), although the quasimomentum-space dynamics in Fig. 3.6(d) are similar to Fig. 3.5(d).

3.2.2 Super-Bloch oscillations

The interplay of spreading dynamics, directed transport, and dynamical localization also manifests, on top of BOs, when an additional constant force is present along with the oscillating potential. At particular resonances, where the driving frequency is a rational multiple of the Bloch frequency, the modulation introduces additional small oscillations on top of the linear evolution of the quasimomentum. These oscillations depend on the initial phase of the drive. As already seen above, when the momentum distribution is symmetric around the center of the Brillouin zone, this results in the spreading of the wave packet [55]. Conversely, an asymmetric distribution produces a coherent directed transport.

For non-resonant driving, where the driving frequency slightly detunes from a rational multiple of the Bloch frequency, the quasimomentum oscillations gain a relative phase that sweeps across the Brillouin zone [75]. This leads to a unique transport behavior with the wave packet reversing its direction as the phase changes sign. The result is a slow oscillatory transport on top of Bloch oscillations, known as super-Bloch oscillations.

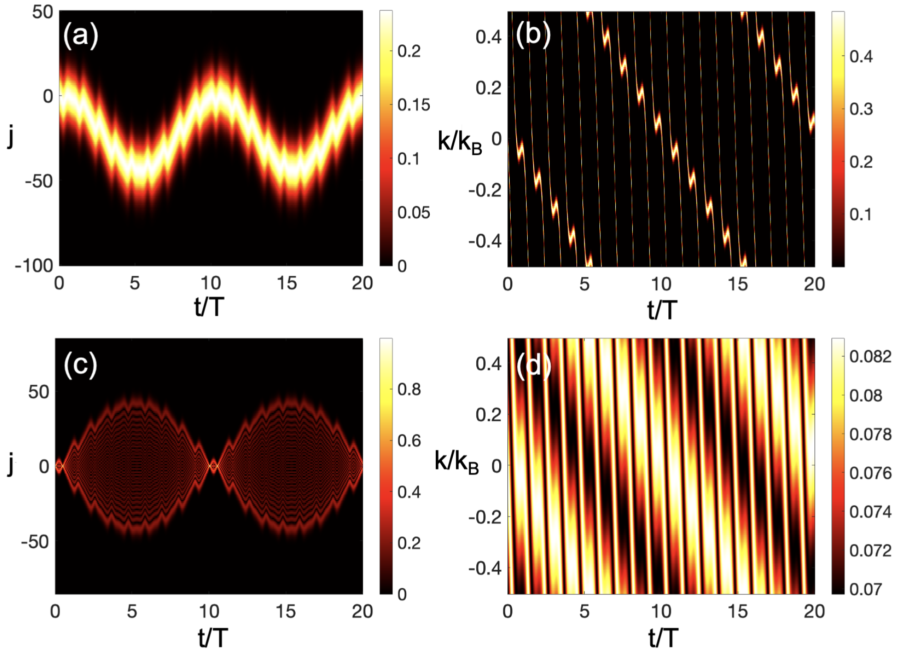

Figure 3.7: Absolute values of the wave packet evolution in real and quasimomentum space. Super-Bloch oscillations for the same broad Gaussian wave packet as employed in Fig. 3.5 ((a) and (b)) and a sharply localized initial state , i.e., $|\Phi_j(t=0)\rangle = \delta_{j0}$ ((c) and (d)), respectively. The system parameters are $J = 1.0E_R$, $Fa = 0.605E_R$, $F_0a = 0.5E_R$, $\hbar\omega = 0.45E_R$, and thus $\delta\omega = 0.05$.

To describe these dynamics, we account for the constant force by defining the periodically modulated force as $F(t) = F_0 + F\sin(\omega t + \phi)$, where the driving frequency is tuned near a rational multiple of the Bloch frequency, such that $F_0a = \hbar(r\omega + \delta\omega)$. Then, the solution to the acceleration relation in Eq. (3.32) is

$$k_c(t) = k_c(0) - (r\omega + \delta\omega)t - \frac{Fa}{\hbar\omega}\cos(\omega t + \phi) + \frac{Fa}{\hbar\omega}\cos(\phi). \tag{3.35}$$

Accordingly, the effective dispersion relation takes the form

$$\varepsilon(k) = -\frac{2J}{T}\int_0^T dt \cos\left(k_c(0) - (r\omega + \delta\omega)t - \frac{Fa}{\hbar\omega}\cos(\omega t + \phi) + \frac{Fa}{\hbar\omega}\cos(\phi)\right), \tag{3.36}$$

which can be solved by integrating over the fast oscillating phases with ω and treating $t' \equiv \delta\omega t$ as a constant term, since $t' \ll t$ due to $\delta\omega' \ll 1$. Thus, the solution to above equation is approximately given by [73]

$$\varepsilon(k) \simeq -2J\mathcal{J}_r\left(\frac{Fa}{\hbar\omega}\right)\cos\left(k_c(0)a + \delta\omega t + \left(\frac{Fa}{\hbar\omega}\right)\cos(\phi) - r(\phi + \frac{\pi}{2})\right), \tag{3.37}$$

from which the average group velocity follows as

$$\bar{v}_g(t) \simeq \frac{2Ja}{\hbar}\mathcal{J}_r\left(\frac{Fa}{\hbar\omega}\right)\sin\left(k_c(0)a + \delta\omega t + \left(\frac{Fa}{\hbar\omega}\right)\cos(\phi) - r(\phi + \frac{\pi}{2})\right). \tag{3.38}$$

These results highlight that in the presence of a static force, the tunneling parameter for a near-resonant driving from a fixed resonance r scales with Bessel functions $\mathcal{J}_r\left(\frac{Fa}{\hbar\omega}\right)$, rather than being renormalized solely by $\mathcal{J}_0\left(\frac{Fa}{\hbar\omega}\right)$, as observed in the case of an oscillating force. Thus, in the Bloch oscillating system, dynamical localization occurs at zeroes of the Bessel function $\mathcal{J}_r$ determined by whether a primary resonance for $r = 1$ or other secondary resonances are triggered. The time-dependent average group velocity in the presence of detuning also reveals oscillatory transport, which takes place irrespective of the drive phase. For $\delta\omega = 0$, the above equation suggests spreading and transport dynamics along with BOs, which are determined by the phase shift $(Fa/\hbar\omega)\cos(\phi)$.

Integrating above equation one obtains the time evolution of the cycle-averaged position

$$\begin{aligned}\bar{x}(t) \simeq \frac{2Ja}{\hbar\delta\omega}\mathcal{J}_r\left(\frac{Fa}{\hbar\omega}\right)\Bigg[&\cos\left(k_c(0)a + \delta\omega t + \left(\frac{Fa}{\hbar\omega}\right)\cos(\phi) - r\left(\phi + \frac{\pi}{2}\right)\right)\\ &- \cos\left(k_c(0)a + \left(\frac{Fa}{\hbar\omega}\right)\cos(\phi) - r\left(\phi + \frac{\pi}{2}\right)\right)\Bigg],\end{aligned} \tag{3.39}$$

which depends on the detuning $\delta\omega$. This signifies the strongly amplified spatial motion with small detuning and period $T_{SBO} = 2\pi/\delta\omega$ much larger than the period of BOs T_B.

The super-Bloch oscillations (SBOs) is shown in Fig. 3.7. The slow oscillatory transport with an amplitude much longer than the ordinary BOs is visible in Fig. 3.7(a). The detuning is 10 times smaller than the Bloch frequency, which corresponds to a super-Bloch period of $T_{SBO} = 10T_B$. Keeping in view the ratio $J/F_0 = 2$, the Wannier-Stark interval $L = 8$ is much smaller than the amplitude of super-Bloch oscillations in Fig. 3.7(a). The quasimomentum-space dynamics shown in Fig. 3.7(b) illustrates the modulation induced rapid oscillations of the quasimomntum, on top of its linear increase, which move inside the Brillouin zone with a constant relative phase. The oscillations of the quasimomentum appear only once every Bloch period in the case of a primary resonance. Moreover, a super-Bloch period is completed as the meta-stable momentum completes one round inside the Brillouin zone. Fig. 3.7(c) and (d) exhibit super-Bloch dynamics for a sharply localized initial wave packet, which performs breathing SBOs due to its large spread in momentum spread. The quasimomentum dynamics reveal a large spread at the metastable-momenta that results in an amplified oscillatory breathing motion.

Impact of Spatial Inhomogeneity on Bloch Oscillations

4

Bloch oscillations typically emerge in a spatially-homogenous periodic lattice under the influence of a constant force. However, real physical systems often exhibit spatial inhomogeneities, such as intrinsic disorders in solid-state crystals or optically-tunable disorders engineered in optical lattice systems. Thus, the fundamental question of how Bloch oscillations are modified by these lattice inhomogeneities arises.

In this chapter, we discuss Bloch oscillations in spatially-inhomogeneous lattices. We first describe the influence of local and quasiperiodic disorder on Bloch oscillations, thus by providing initial understanding and context. Subsequently, we extend our analysis to globally inhomogeneous lattices by considering the example of a parabolic optical lattice. While this analysis highlights the modifications in Bloch oscillatory dynamics induced by the global inhomogeneity, other related dynamics in the parabolic lattice system are also revealed. Finally, these dynamics are investigated for interacting atoms.

4.1 Bloch Oscillations in a Disordered Lattice

In an ideal periodic lattice, Bloch oscillations continue indefinitely without fading. However, the presence of spatial disorder significantly alters the dynamics, leading to dephasing and other complex effects. In this section, we discuss Bloch oscillations in a disordered lattice, focusing on two distinct types of inhomogeneities: the first induced by an incommensurate optical potential and the second resulting from randomly placed impurity atoms in a periodic potential.

4.1.1 Disorder Induced by an Incommensurate Optical Potential

A simple way to introduce disorder in an optical lattice is by combining it with an additional incommensurate potential, which results in a quasi-disordered lattice. Let us consider the superposition of an optical potential $V_0(x)$ with a weaker incommensurate periodic potential $V_1(x)$, such that the period of $V_0(x)$ is twice the period of $V_1(x)$, resulting into a quasiperiodic structure, as illustrated in Fig. 4.1 (left panel). This configuration effectively maps onto a period-doubled tight-binding model carrying an energy mismatch ε between neighboring site, describing a binary lattice [123]. The binary lattice subjected to a constant force is described by the Hamiltonian

$$\widehat{H} = -J \sum_{j=-\infty}^{\infty} (|j+1\rangle\langle j| + h.c) + \sum_{j=-\infty}^{\infty} (F_0 a + \frac{\varepsilon}{2}(-1)^j)|j\rangle\langle j| \, . \tag{4.1}$$

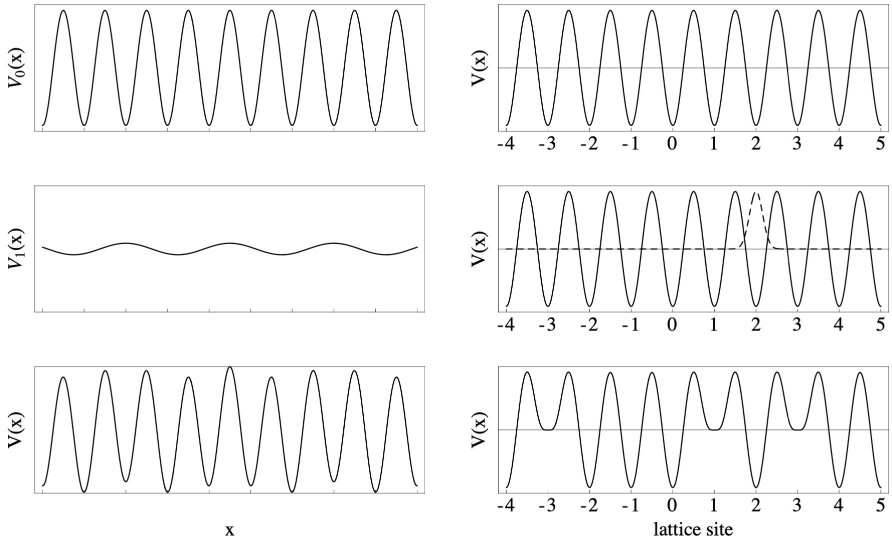

Figure 4.1: Schematic diagram showing two kind of disorders in a periodic lattice. Left panel: A periodic optical lattice $V_0(x)$ is depicted at the top. The middle shows a much weaker potential $V_1(x)$ with a period almost twice the period of the main lattice. This potential induces disorder and the resulting quasiperiodic lattice $V(x)$ is shown at the bottom. Right panel: Again, a periodic lattice $V(x)$ in the top, which is shown superposing with a Gaussian impurity (dashed line) in the middle. The bottom figure shows a disordered lattice in the presence of randomly placed impurities. Taken from [122].

As seen in Fig. 4.2(a) and (b), Bloch oscillations in the binary lattice exhibit rapid dephasing followed by periodic revivals. In real space, the wave packet initially follows standard Bloch oscillatory motion, although as it evolves, the quasi-disorder causes parts of the wave packet to accumulate phase shifts at different rates, leading to dephasing. However, since the lattice furnishes a quasiperiodic structure rather than being purely random, the wave packet eventually undergoes constructive interference, resulting in a partial revival.

In quasimomentum space, the dynamics follow a similar trend, displaying dephasing followed by revivals. This behavior suggests that while the disorder causes a decay of Bloch oscillations, the quasi-periodicity allows for wave packet reconstruction at later times.

4.1.2 Disorder introduced by Localized Impurity Atoms

Another form of disorder arises from localized impurities embedded within the lattice. In our analysis, we again consider the tight-binding lattice with a constant force and represent the impurity atoms using a Gaussian potential

$$V_{\text{imp}}(j) = A\, e^{-\frac{(j-j_i)^2}{2\sigma_i^2}}, \tag{4.2}$$

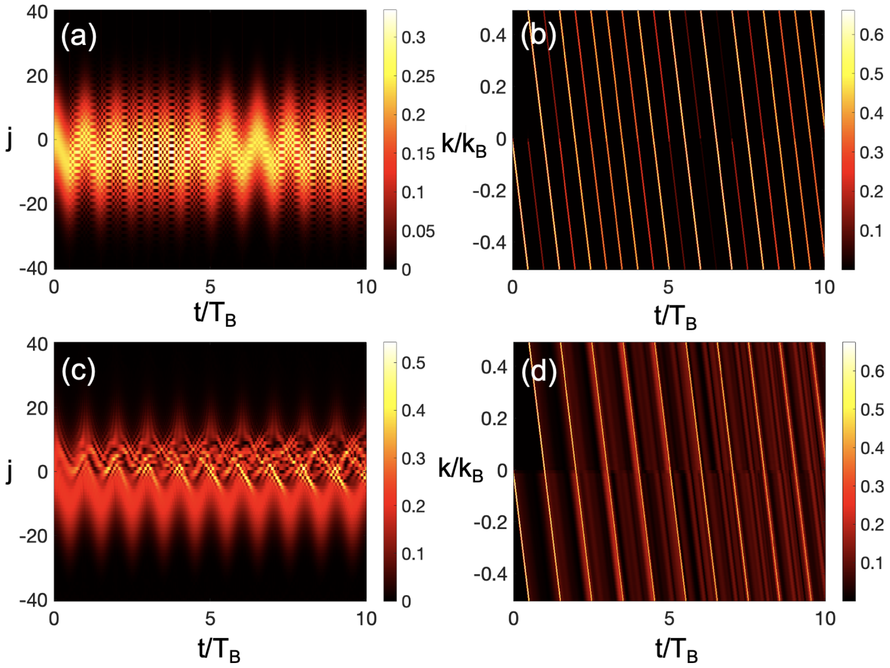

Figure 4.2: Absolute values of the wave packet evolution in real and quasimomentum space. Bloch oscillations in the quasi-disordered lattice ((a) and (b)) and in a locally disordered lattice with Gaussian potential at j_i ((c) and (d)), respectively. A broad Gaussian wave packet with width $\sigma_0 = 10$, momentum $k_0 = 0$, and position $j_0 = 0$ is evolved. The system parameters are $J = 1.0E_R$, $F_0 a = 0.5E_R$, $\varepsilon = 10^{-2}E_R$ and the Gaussian potential is specified by $A = 10^{-2}E_R$, $\sigma_i = 1$, and $j_i = 5$.

centered at lattice site j_i, as depicted in Fig. 4.1 (right panel). This impurity acts as a local perturbation, influencing the wave packet dynamics in a distinct manner compared to an incommensurate potential.

As shown in Fig. 4.2(c), initially some fractions of wave packet density diminish as they encounter the disorder at j_0. This leads to a phase difference, creating interference between evolving fractions of density. These fractions are progressively and periodically affected by the disorder, causing the interference effects to grow and ultimately leading to the partial collapse of the total density. As successive portions of the wave packet reach the impurity, they continue to split and interfere with previously scattered components. This repeated interference results in progressive dephasing of the oscillations. However, the unaffected part of the wave packet performs coherent oscillations.

Fig. 4.2(d) displays the quasimomentum-space representation of these dynamics. The k-space evolution highlights the fractions of density that separate from the wave packet at the beginning of the evolution and at every Bloch period. These fractions evolve alongside the coherent density, eventually causing multiple interferences as time progresses. Unlike the incommensurate potential case, where revivals are prominent, the localized impurity leads to a more continuous decay. Although the decay feature can be quantified by calculating the expectation values and the dynamics of the width, and the revival times can be predicted analytically, here we focus instead on providing a qualitative analysis of Bloch dynamics in disordered lattices.

In conclusion, the introduction of disorder in a periodic lattice significantly influences Bloch oscillations. An incommensurate optical potential induces quick dephasing followed by revivals, preserving the underlying coherence of the system to some extent [124]. In contrast, a localized impurity causes progressive dephasing through repeated wave packet splitting and interference. These findings highlight the sensitivity of Bloch oscillations to different forms of lattice inhomogeneity and provide insight into their behavior in realistic experimental setups.

4.2 Bloch Oscillations in Parabolic Optical Lattices

Similar to the disordered lattice a global inhomogeneity of an optical lattice modifies the Bloch dynamics. If the external parabolic trapping is relatively strong an inhomogeneous periodic lattice naturally exists which is often termed as parabolic optical lattice. In the presence of a global harmonic trap the lattice is symmetrically curved which gives rise to rich dynamics and Bloch oscillations-like dynamics exists in a regime of weakly curved periodic wells of the parabolic lattice [79]. In this section, we mainly focus on Bloch oscillations in the parabolic lattice system, while discussing some other aspects of the dynamics as well.

Parabolic Optical Lattice

The parabolic lattice system consists of ultracold atoms confined in an axially symmetric crossed optical dipole trap which provides weak confinement in the axial direction in contrast to the strong confinement along the transverse plane. In the regime of strong transverse confinement, the effective potential along the axial direction varies parabolically. Additionally, a 1D-optical lattice is superimposed on the parabolic potential, creating a symmetrically curved periodic potential. In dipole and rotating wave approximations, the dynamics of ultracold atoms in the axial direction is effectively governed by the Hamiltonian

$$H = \frac{p^2}{2M} + \; V_o \; \sin^2\left(\frac{\pi}{a}x\right) + \frac{1}{2}M\omega_\tau^2 x^2, \tag{4.3}$$

where ω_τ denotes the frequency of the parabolic trap. The wave packet dynamics we discuss is assumed to start by a sudden displacement of the center of the parabolic potential at $t = 0$. This shift moves the atomic cloud into the curved periodic wells of the parabolic lattice, from where begins evolution.

Single Particle Treatment

Let us assume that interatomic interactions are eliminated using Feshbach resonance tuning. Under this condition, the behavior of noninteracting ultracold atoms can be analyzed within the single-particle framework. Moreover, if the lattice depth is much larger than the recoil energy $E_R = h^2/8Ma^2$ and the strength of the parabolic potential remains significantly weaker than the tunneling, the Hamiltonian (4.3) can be described using the single-band tight-binding approximation as [89]

$$\widehat{H}_{TB} = -J \sum_{j=-\infty}^{\infty} (|j+1\rangle\langle j| + |j\rangle\langle j+1|) + \Omega \sum_{j=-\infty}^{\infty} j^2 |j\rangle\langle j|, \tag{4.4}$$

where $|j\rangle$ are the ground band Wannier functions and $\Omega = M\omega^2 a^2/2$ represents the strength of the parabolic potential. The wave function $|\Phi\rangle$ can be represented as a superposition of Wannier states as

$$|\Phi(t)\rangle = \sum_j \phi_j(t)\,|j\rangle. \tag{4.5}$$

Substituting this into the Schrödinger equation with the Hamiltonian (4.4), leads to a system of coupled linear differential equations that describe the time evolution of the complex amplitudes $\phi_j(t)$

$$i\hbar\dot{\phi}_j = -J(\phi_{j+1} + \phi_{j-1}) + \Omega\, j^2 \phi_j. \tag{4.6}$$

This system allows for stationary solutions of the form $\phi_j^\ell(t) = \varphi_j^\ell e^{-iE_\ell t/\hbar}$, where φ_j^ℓ represents the ℓth eigenstate in Wannier space, and E_ℓ is the corresponding eigenenergy. Substituting this ansatz into Eq. (4.6) leads to the eigenvalue equation

$$E_\ell \varphi_j^\ell = -J(\varphi_{j+1}^\ell + \varphi_{j-1}^\ell) + \Omega\, j^2 \varphi_j^\ell. \tag{4.7}$$

To further analyze these eigenstates, we represent them as Fourier coefficients of a π-periodic function $\psi^\ell(\theta)$, expressed as

$$\varphi_j^\ell = \frac{1}{\pi}\int_0^\pi d\theta\ \psi^\ell(\theta) e^{-2ij\theta}. \tag{4.8}$$

This recasts Eq. (4.7) into a Mathieu equation [97],

$$\left[\frac{\partial^2}{\partial\theta^2} + \left(\frac{4E}{\Omega}\right) - 2\left(\frac{-4J}{\Omega}\right)\cos(2\theta)\right]\psi^\ell(\theta) = 0, \tag{4.9}$$

with Mathieu characteristic parameters $4E/\Omega = \alpha$ and $4J/\Omega = q$. The above equation is formally equivalent to the Schrödinger equation for a quantum pendulum with the Hamiltonian

$$\hat{\mathcal{H}} = \frac{\Omega}{4}\hat{L}^2\ - 2J\cos(2\theta), \quad \hat{L} = -i\frac{\partial}{\partial\theta}, \tag{4.10}$$

where L_z denotes the angular momentum of the pendulum. Thus, one can interpret the dynamics generated by the tight-binding system (4.4) in terms of the pendulum. Also, the above Hamiltonian corresponds exactly to equation (4.4) represented in the Bloch basis. In this mapping, the pendulum momentum L_z is equivalent to the scaled position $2x/a$, while the phase θ of the pendulum is related to the quasimomentum k via $\theta = ka/2$.

Accordingly, the functions ψ are $\pi-$periodic Mathieu Functions [97], which for even and

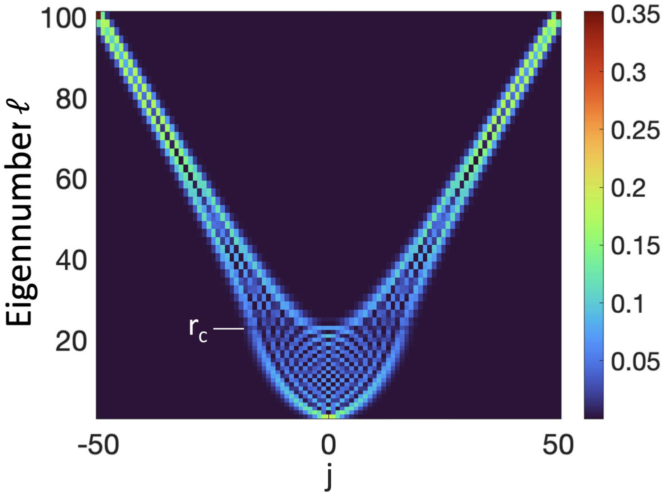

Figure 4.3: Probability density of the lowest 100 eigenstates of the parabolic lattice in the single-band tight-binding approximation. The eigenstates are obtained by diagonalizing Eq. (4.4). Each eigenstate is shifted along the y-axis based on its corresponding eigennumber ℓ, with ℓ_c marking the critical point above which the eigenstates change from harmonic oscillator-like states to Wannier-Stark-like states. The parametric values are $J = 2.4 \times 10^{-2} E_R$ and $\Omega = 3.2 \times 10^{-4} E_R$. This figure is taken from [89] with permission.

odd values of the quantum number ℓ are written as

$$\psi^{\ell}(\theta) = \begin{cases} \sqrt{\frac{2}{\pi}} ce_{\ell}(\theta, -q), & even \\ \sqrt{\frac{2}{\pi}} se_{\ell+1}(\theta, -q), & odd \end{cases}, \tag{4.11}$$

with $\ell = 0, 1, 2, ...$, and the energies are given by

$$E_{\ell} = \begin{cases} \frac{\Omega}{4} a_{\ell}(q), & even \\ \frac{\Omega}{4} b_{\ell+1}(q), & odd \end{cases}, \tag{4.12}$$

where $a_{\ell}(q)$, $b_{\ell+1}(q)$ represent the characteristic values of α. Re-substituting the solution for $\psi^{\ell}(\theta)$ into Eq. (4.8) gives (see Appendix A.1 for details)

$$\varphi_j^{\ell} = \begin{cases} \frac{1}{\pi}\sqrt{\frac{2}{\pi}} \int_0^{\pi} ce_{\ell}(\theta, -q) \cos(2j\theta)\, d\theta, & \text{even} \\ \frac{1}{\pi}\sqrt{\frac{2}{\pi}} \int_0^{\pi} se_{\ell+1}(\theta, -q) \sin(2j\theta)\, d\theta, & \text{odd} \end{cases}, \tag{4.13}$$

which are the symmetric and anti-symmetric π-periodic solutions for the real-space wave function amplitudes. The spatially-extended nature of Mathieu functions, suggests that their Fourier coefficients are strongly localized functions [97, 125]. These localized functions manifest as eigenstates, resembling harmonic oscillator eigenfunctions concentrated around the

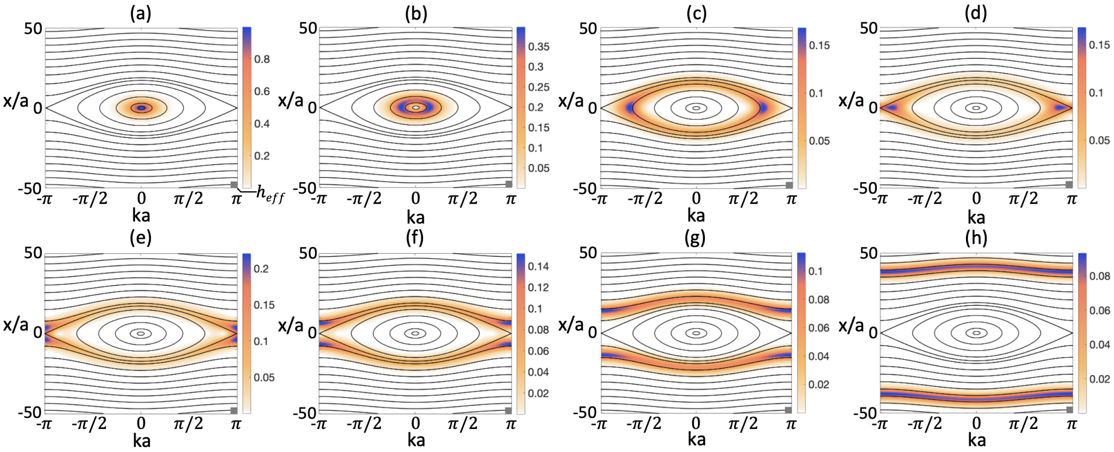

Figure 4.4: Husimi-Q representations of eigenstates displayed in panels (a) to (h) for $\ell = 0, 1, 15, 20, 24, 25, 35,$ and 80, respectively. The classical phase space of the pendulum Hamiltonian (4.10) is superimposed on each result for comparison. The width of the coherent states is $\sigma_x = 2.23$ and the system parameters remain the same as were in Fig. 4.3. This figure is taken from [89] with permission.

trap origin and Wannier-Stark-like localized states positioned away from the trap center [89, 126–129]. The Wannier-Stark-like states emerge as the energy E_ℓ exceeds the energy $2J$ corresponding to the band edge of the uniform lattice potential. The critical energy eigen number at which the character of eigenstates changes is $\ell_c = ||\sqrt{q}||$, where $||x||$ denotes the nearest integer to x. In Fig. 4.3 the probability density of the lowest 100 eigenstates is shown, which we obtain from the eigenvectors of Eq. (4.4), as the eigenvectors correspond to the eigenstates in the Wannier representation. The resemblance of the states below ℓ_c to the well-known harmonic oscillator spectrum of states and the states above ℓ_c localized on both sides of the parabola in a Wannier-Stark-like manner is visualized. The simultaneous occupation of both sides of the parabola highlight that the Wannier-Stark-like eigenstates are (almost) two-fold degenerate, where the localization of a state increases on both sides as the local tilt induced by the parabolic potential becomes increasingly steep, and the localized densities are pushed one lattice site further with each increase in r.

In order to describe the dynamical features of the system, we analyze the dynamics of the eigenstates by comparing them against the pendulum dynamics. This is done by tracing the phase space distributions of eigenstates and comparing them against the phase space generated by the pendulum Hamiltonian (4.10). To obtain the phase space distributions of eigenstates we consider the Husimi-Q function [130] which is constructed through the overlap

$$Q_\chi(x, k) = |\langle \alpha_{x,k} | \chi \rangle|^2, \tag{4.14}$$

where $\alpha_{x,k}$ represents coherent states with a maximal density at the coordinates x, k. The coherent states in position representation can be expressed as

$$\alpha_{x,k}(x') = \langle x'|\alpha_{x,k}\rangle = \frac{1}{\sqrt{\sigma_x\sqrt{\pi}}}\,\mathrm{e}^{-\frac{(x'-x)^2}{2\sigma_x^2}}\,\mathrm{e}^{-ik(x'-x)}. \tag{4.15}$$

Figure 4.4 presents the results of our comparison, where the Husimi-Q functions are obtained by setting $|\chi\rangle = |\varphi_j^\ell\rangle$ for a few selected values of ℓ. The Husimi distributions are depicted intersecting with the phase space of the pendulum, which consists of regions with open and closed curves. These regions are separated by a special curve known as the separatrix. The separatrix is defined as the curve where the energy of the pendulum equals the saddle-point energy $2J$. Hence, the separatrix is expressed as

$$x_c = a\sqrt{\frac{2J}{\Omega}(1+\cos(ka))}. \tag{4.16}$$

The results in Fig. 4.4 showcase harmonic oscillator-like states clinging to the closed curves, few intermediate states lying around the separatrix curve, and the Wannier-Stark like states evolving as per vibrational trajectories in pendulum phase space. This reveals that the dynamics of harmonic oscillator-like states are analogous to vibrations of the pendulum, while the time evolution of Wannier-Stark-like states resembles rotations of the pendulum. The vibrational regime of the pendulum is equivalent to the harmonic oscillations of the wave packet across the center of the parabolic lattice in real space and around the center of the Brillouin zone in quasimomentum space. Also, the momentum preserving its sign and the phase folding back onto itself during full rotations of the pendulum manifests in the lattice problem as periodic oscillations of the localized state in real-space and almost linear translation in the quasimomentum-space. This is equivalent to a Bloch oscillations-like motion in a locally linear potential on one side of the parabolic lattice. As the eigenstates for $\ell > \ell_c$ are strongly localized at positions $x = \pm\ell a/2$, the locally static force experienced by a Wannier-Stark-like state ℓ is given by $F = \pm\Omega\ell/a$.

Thus, harmonic oscillator-like and Wannier-Stark-like states exist below and above x_c, respectively. Hence, an ultracold atomic wave packet occupying harmonic oscillator-like states with an initial shift below x_c exhibits harmonic-oscillator-like dynamics around the center of the parabolic lattice, while a wave packet triggering Wannier-Stark-like state in the presence of a large shift in position, i.e., above x_c, performs Bloch oscillations-like dynamics on one side, unless $x_0 < x_{max}$, where $x_{max} = \sqrt{\Omega/4J}$ defines the maximum shift above which Landau-Zener tunneling to higher bands sets in [89]. Note that $j_{max} = 129$ for the parameters adopted in the present work. The Bloch oscillations-like dynamics are shown in Fig. 4.5 for a broad Gaussian wave packet, as defined in Eq. (3.32), with width $\sigma_0 = 2.23$ and initial position $j_0 = 30$. For the parameters stated in Fig. 4.3, and with $k = 0$ the separatrix lies at $x_c \approx 17$. Thus, for $j_0 = 30$ the wave packet performs Bloch oscillations-like dynamics which dephase quite rapidly. This leads to a collapse of the Bloch dynamics which is followed by periodic revivals [131], as shown in Fig. 4.5(a). Figure 4.5(b) also highlight the linear evolution of the quasimomentum in the first Brillouin zone. The dephasing and revival are also

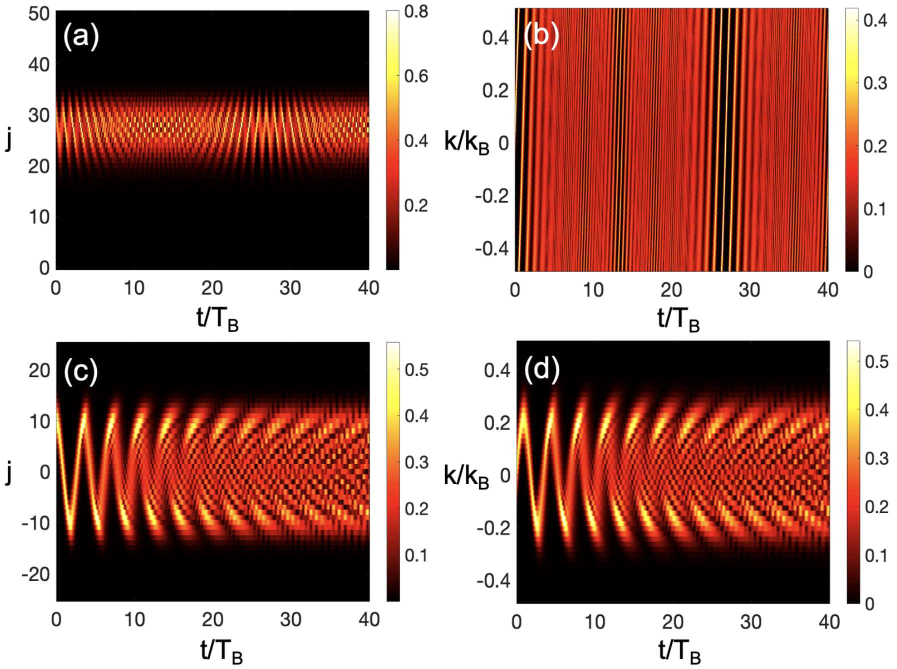

Figure 4.5: Absolute values of the wave packet evolution in real and quasimomentum space. The dynamics resemble Bloch oscillations and dipole oscillations for a Gaussian wave packet in the parabolic optical lattice with width $\sigma_0 = 2.23$, initial momentum $k_0 = 0$, and initial position $x_0 = 30$ in (a) and (b), followed by $x_0 = 10$ in (c) and (d), respectively. The system parameters remain the same as in Fig. 4.3.

visible in the quasimomentum-space dynamics. In Fig. 4.5(c) harmonic oscillator-like dynamics around the center of the parabolic lattice are obtained at $j_0 = 10$. The corresponding oscillations of the quasimomentum around the center of the Brillouin zone are also seen in the quasimomentum-space dynamics, shown in Fig. 4.5(d). Similar to the Bloch oscillation-like dynamics the dipole oscillations also dephase, however, the revival times are much longer than the revival in Fig. 4.5(a). The revival phenomenon is the outcome of the finite number of discrete lattice sites explored by the wave packet and is captured by the mean atomic velocity [80]

$$\bar{v}(t) = -\frac{2Ja}{\hbar}\sum_{m=-\infty}^{\infty}\exp\left\{-\frac{((m+1)^2+(m)^2)}{2\sigma_0^2}\right\}\sin\left((k_0a+\nu t)+\frac{2\Omega t}{\hbar}m\right). \tag{4.17}$$

where $m = j - j_0$ and ν represents the frequency of oscillations which is given by $\nu_B = 2\Omega j_0/\hbar$ for Bloch-like oscillations and $\nu_D = \sqrt{4J\Omega}/\hbar$ for dipole oscillations. Replacing the sum by an integral and solving yields

$$\bar{v}(t) \approx -\frac{2\sqrt{\pi}Ja\sigma_0}{\hbar}\exp\left\{-\left(\frac{t^2}{\tau_\sigma^2}-\frac{1}{2\sigma_0^2}\right)\right\}\sin\left(k_0a+\nu t\right). \tag{4.18}$$

where $\tau_\sigma = \beta\hbar/\Omega\sigma_0$ represents the dephasing time, with constant factor $\beta = 1$ for Bloch-like oscillation and $\beta = 8$ for dipole oscillations. The above result suggests a quadratically increasing exponential decay of oscillations caused by the dephasing. Moreover, Eq. (4.18) predicts an irreversible decay of oscillations due to the approximation of the sum by an integral and thus misses the revival phenomenon.

4.2.1 Local Acceleration Theorem

To further explain the dynamics we present a simple analytical model, which provides interesting perspective on Bloch and dipole oscillations. We consider the tight binding Hamiltonian (4.4) expressing it in Bloch basis, leading to the energy function

$$E(k) = -2J\cos(ka) + \Omega(x/a)^2. \tag{4.19}$$

Thus, one can define the Bloch acceleration

$$\hbar\dot{k} = -\frac{\partial E(k)}{\partial x} = -\left(\frac{2\Omega}{a^2}\right)x, \tag{4.20}$$

which can be rewritten as

$$k_c(t) = k_c(0) - \frac{2\Omega}{a^2}\int_0^t x_c(t')\,dt'. \tag{4.21}$$

Taking into account the Bloch oscillatory motion away from the center of parabolic trap and ignoring the dephasing, the time-dependent evolution of the wave packet's center can be represented as $x_c(t) = x_c(0) + \Delta x\cos(\nu_B t + k_c(0)a)$. Substituting this ansatz into Eq. (4.16) we have

$$k_c(t) = k_c(0) - \frac{2\Omega x(0)}{a^2\hbar}t - \frac{2\Omega\Delta x}{a^2\hbar\nu_B}\sin(\nu_B t + k_c(0)a). \tag{4.22}$$

With $\nu_B = 2\Omega x(0)/a\hbar$ the above equation gives

$$k_c(t) = k_c(0) - \frac{\nu_B}{a}t - \frac{\Delta x}{x(0)a}\sin(\nu_B t + k_c(0)a). \tag{4.23}$$

For $x(0) \gg \Delta x$ the last term becomes negligible, and thus $k_c(t)$ evolves linearly in time, exhibiting Bloch oscillations-like dynamics, as seen in Fig. 4.5(a-b). The oscillation amplitude is given by $\Delta x = Ja^2/2\Omega x(0)$.

Similarly, one can follow the same procedure for the dipole oscillations using the ansatz $x_c(t) = x_c(0)\cos(\nu_D t + k_c(0)a)$. In this case Eq. (4.16) reduces to

$$k_c(t) = k_c(0) - \frac{2\Omega x_c(0)}{a^2\hbar\nu_D}\left[\sin(\nu_D t + k_c(0)a) - \sin(k_c(0)a)\right]. \tag{4.24}$$

This represents periodic oscillations in quasimomentum-space with frequency $\nu_D = \sqrt{4J\Omega}/\hbar$ and amplitude determined by $\frac{x_c(0)}{a^2}\sqrt{\frac{\Omega}{J}}$.

Classical Dynamical Equations

The acceleration relation and the group velocity calculated for the energy function in Eq. (4.16) transforms back into classical equations of motion by replacing the mean values x_c and k_c by classical variables x and $p = \hbar k$. Thus, one can write

$$\dot{p} = -\frac{2\Omega}{a^2}\, x, \tag{4.25}$$

and

$$\dot{x} = 2J\lambda \sin\left(p\lambda\right) , \tag{4.26}$$

where $\lambda = a/\hbar$. The above coupled equations results in an oscillator equation

$$\ddot{p}(t) = -\left(\frac{4J\Omega\lambda}{a^2}\right) \sin(p\lambda) , \tag{4.27}$$

which can be solved using the time dependent ansatz $p(t) = p_0 \sin(\nu_D t)$ [10]. Substituting the ansatz above equation reduces to

$$\begin{aligned} p_0 \nu_D^2 \sin(\nu_D t) &= \frac{4J\Omega\lambda}{a^2} \sin(p_0\lambda \sin(\nu_D t)) \\ &= \frac{8J\Omega\lambda}{a^2} \sum_{n=0}^{\infty} J_{2n+1}(p_0\lambda) \sin[(2n+1)\nu_D t] \ . \end{aligned} \tag{4.28}$$

Comparing the coefficients of $\sin(\nu_D t)$ on both sides we get

$$\nu_D^2 = \frac{8J\Omega\lambda}{a^2 p_0} J_1(p\lambda), \tag{4.29}$$

Thus, the frequency of the oscillator depends upon momentum p_0. For p_0 approaching to zero, we get

$$\nu_D = \frac{\lambda}{a}\sqrt{4J\Omega}\ . \qquad \left(\because \quad \lim_{p_0\to 0}\left\{\frac{J_1(p_0\lambda)}{p_0\lambda}\right\} = \frac{1}{2}\right) \tag{4.30}$$

Finally, the solution for $p(t)$ and $x(t)$ is

$$p(t) = p_0 \sin(\nu_D t) \ , \tag{4.31}$$

$$x(t) = -\left(\frac{p_0 a^2 \nu_D}{2\Omega}\right) \cos(\nu_D t) \ . \tag{4.32}$$

Hence, in the phase space, $(x, p = \hbar k)$, the particle with a finite momentum p, effectively follows rotational dynamics with frequency ν_D and maximum displacement

$$x_c = \pm\sqrt{\frac{2Jp_0\lambda a^2}{\Omega} J_1(p_0\lambda)}. \tag{4.33}$$

4.2.2 Dynamical Tunneling atop Bloch Oscillations

The simultaneous population of Wannier-Stark-like localized states on both sides of the parabolic lattice in Fig. 4.4 suggests the tunneling between symmetry-related pairs of states, which takes place in the presence of a small energy splitting ΔE. Such a tunneling-like response between classically disconnected regions of phase space, in the absence of a potential barrier, is known as dynamical tunneling [132]. The tunneling time is determined by the energy splitting as given by

$$T_{tun} = \frac{\pi\hbar}{\Delta E} \, . \tag{4.34}$$

The asymptotic expansions of the Mathieu functions reveal an intrinsic minuscule splitting scaling with $q^{\ell}/\ell^{(\ell-1)}$ for $\ell \gg \sqrt{q}$ [97]. We also mention that this minute energy splitting is not resolved in our numerical computations. Thus, dynamical tunneling is not seen in the wave packet dynamics shown in Fig. 4.5.

Manipulating the Tunneling Times with Lattice Incommensurability

Employing an incommensurate potential, as already introduced in Sec. 4.1, one can effectively enhance the energy splitting. By introducing a secondary, significantly weaker lattice with twice the periodicity of the primary lattice, an energy offset ε is created between adjacent sites, as described by the modified tight-binding Hamiltonian

$$\widehat{H}' = -J \sum_{j=-\infty}^{\infty} (|j+1\rangle\langle j| + h.c) + \sum_{j=-\infty}^{\infty} (\Omega j^2 + \frac{\varepsilon}{2}\,(-1)^j)|j\rangle\langle j| \, . \tag{4.35}$$

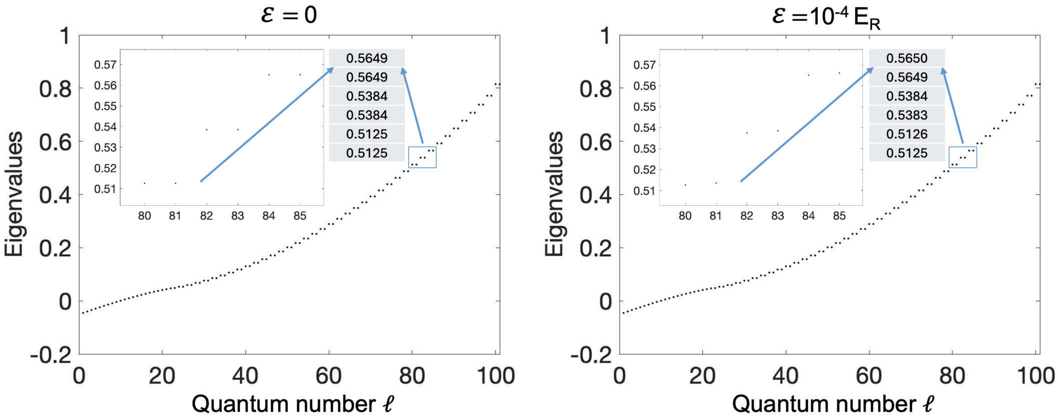

Figure 4.6: Eigenvalue spectrum of the parabolic lattice without an energy mismatch (left) and with the energy mismatch (right). Other parameters remain the same as in Fig. 4.3.

For the energy mismatch to be significantly large, the binary lattice possesses two Bloch bands, offering one of the simplest setups for investigating interband tunneling effects [123].

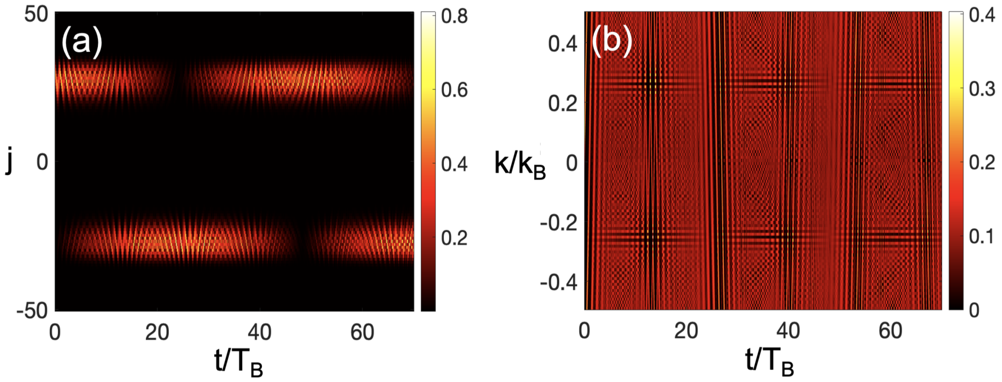

Figure 4.7: Absolute values of the wave packet evolution in (a) real and (b) quasimomentum space. Dynamical tunneling on top of Bloch oscillations-like dynamics for a Gaussian wave packet in a parabolic optical lattice with width $\sigma = 2.23$, initial momentum $k_0 = 0$, and initial position $x_0 = 30$. The system parameters remain the same as in Fig. 4.3. Moreover, the energy mismatch is chosen as $\varepsilon = 3.6 \times 10^{-4} E_R$. The figure is reproduced with permission from Ref. [89].

In contrast we keep the mismatch to be very small, $\varepsilon \ll J$, such that the lattice can still be described by a single band. However, the mismatch still induces a considerable shift in the on-site energies while preserving the two-fold degeneracy of the eigenstates. This is depicted in Fig. 4.6, where we present the eigenvalue spectrum of the system without a mismatch and in the presence of a mismatch. Without an energy shift Fig. 4.6 exhibits doubly degenerate states for $\ell > 24$, while with an energy shift Fig. 4.6 reveals an energy difference between otherwise degenerate states. The tunneling time is approximately given by

$$T_{tun} \approx \frac{\pi\hbar}{\varepsilon} \,, \tag{4.36}$$

allowing one to tune T_{tun} through ε.

Figure 4.7 illustrates the tunneling, where a Gaussian wave packet is initially centered at $n_0 = 30$ with an initial quasimomentum $k_0 = 0$, i.e, positioned it well above the separatrix. As a result, the wave packet undergoes Bloch oscillations confined to one side of the parabolic lattice. Over time, however, it gradually tunnels to the other side, and reappears on the other arm. This process is cyclic, with the wave packet continuously oscillating between the two arms while preserving coherence across significant distances, as seen in Fig. 4.7(a). The computed tunneling time for $\varepsilon = 3.6 \times 10^{-4} E_R$ is approximately 7.18 dipole periods, which aligns well with the theoretical estimate in Eq. (4.36). Additionally, the momentum-space evolution depicted in Fig. 4.7(b) which reveals that upon tunneling, the wave packet acquires an opposite momentum, causing oscillations on the second arm to occur in the reverse direction relative to its initial motion.

4.2.3 Dynamics in the Presence of Atom-Atom interactions

We analyze the dynamics governed by Hamiltonian (4.3), considering interacting atoms within the framework of the 1D Gross-Pitaevskii equation [94, 133],

$$i\hbar\frac{\partial\psi(x,t)}{\partial t} = H\psi(x,t) + g_{1\mathrm{D}}|\psi(x,t)|^2\psi(x,t), \tag{4.37}$$

where $g_{1\mathrm{D}} \sim a_s\omega_\perp N$, with a_s representing the s-wave scattering length, $\omega_\perp$ denoting the trapping frequency along the transverse plane, and N indicating the total number of atoms.

For comparison with the single-particle dynamics described above, we again restrict ourselves to the single-band tight-binding approximation, under which Eq. (4.37) takes the form

$$i\hbar\dot{\phi}_j = -J(\phi_{j+1} + \phi_{j-1}) + \Omega\, j^2\phi_j + g|\phi_j|^2\phi_j, \tag{4.38}$$

where $g = g_{1\mathrm{D}}\int|\psi_j(x)|^4\,dx \sim a_s\omega_\perp N/a$.

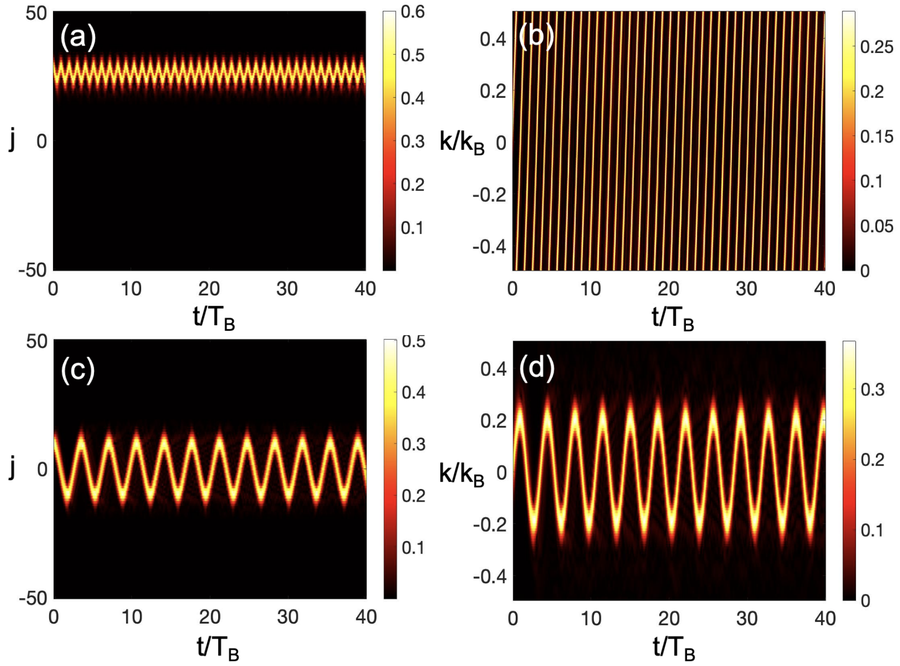

Figure 4.8: Absolute values of the wave packet evolution in real and quasimomentum space. Bloch oscillations and dipole oscillations sustained by nonlinearity for the Gaussian wave packet shown in Fig. 4.5, under the same parameters, considering weak atom-atom interactions with strength $g = 2.3 \times 10^{-2}E_R$.

In Fig. 4.8, the dynamics generated by Eq. (4.38) are shown. The results reveal that for the same Gaussian wave packet initially placed at two different lattice sites in Fig. 4.5, the dynamics becomes coherent in the presence of weak inter-atomic interactions. Fig. 4.8(a-b) exhibits coherent Bloch oscillations and Fig. 4.8(c-d) showcases sustained dipole oscillations. The inter-

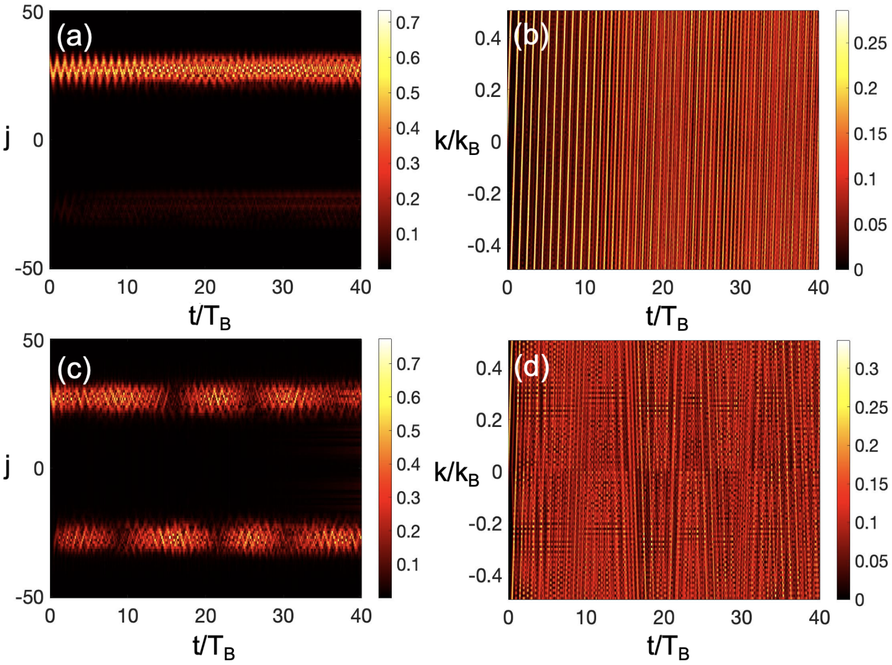

Figure 4.9: Absolute values of the wave packet evolution in real and quasimomentum space. Dynamical tunneling for interacting atoms. The system parameters remain the same as in Fig. 4.7, although the energy mismatch $\varepsilon = 3.6 \times 10^{-4} E_R$ in (a-b) is made stronger $\varepsilon = 2.0 \times 10^{-2} E_R$ in (c-d). The interaction strength is $g = 2.3 \times 10^{-2} E_R$.

action strength is chosen as $g = 2.3 \times 10^{-2} E_R$, which is very close to the tunneling strength. We note that as g is raised above this value Bloch oscillations diminish, although dipole oscillations exhibit such a decay at a much higher value of g. These effects are investigated using variational method in Ref. [81]. The sustained oscillations in the presence of weak interactions provides interesting perspective for experimental investigation [134].

In order to explore the effect of inter-atomic interactions on tunneling dynamics discussed in Sec. 4.2.2, we again consider the energy mismatch effectuated by an additional incommensurate optical potential. Thus, Eq. (4.38) with Hamiltonian (4.35) takes the form

$$i\hbar\dot{\phi}_j = -J(\phi_{j+1} + \phi_{j-1}) + (\Omega\, j^2 + \frac{\varepsilon}{2}\,(-1)^j)\phi_j + g|\phi_j|^2\phi_j. \tag{4.39}$$

The dynamics obtained by solving above equation are depicted in Fig. 4.9. We use the same strength of nonlinearity as was previously shown to suppress dephasing, leading to coherent Bloch oscillations. In Fig. 4.9(a-b), we present the tunneling dynamics by keeping the same energy mismatch as used in Fig. 4.8. The results reveal a significant suppression of tunneling due to inter-atomic interactions, with only a small fraction of the wave packet transferring. This reduction in tunneling suggests a shift in the tunneling splitting induced by the nonlinearity.

To further investigate these effects, in Fig. 4.9(c-d), we examine the tunneling dynamics under an even stronger energy mismatch. Under these conditions, the system exhibits pronounced dynamical tunneling between opposite ends of the parabolic lattice. However, the wave packet transfer does not occur at fixed intervals but instead follows a nontrivial time-dependent pattern, revealing a complex interplay of competing effects. This observation suggests the presence of a more intricate tunneling mechanism, where interactions and external parameters collectively dictate the transport behavior.

These findings highlight the intricate role of nonlinearity and energy mismatches in shaping tunneling dynamics. The observed complex interaction-driven tunneling behavior warrants further investigation and will be explored in future work.

Bloch Dynamics in Parametrically Driven Optical Lattices

5

In parabolic optical lattices, Bloch oscillations emerge in a confined region of space where the parabolic trapping potential can be approximated by a locally linear potential, and the space-dependent force from the parabolic trap remains nearly constant. Although these dynamics dephase quite rapidly, a reconstruction usually follows due to wave packet motion across a finite number of lattice sites during Bloch oscillations. The dephasing is shown to be counteracted by a weak nonlinearity when considering the interacting atoms [81]. The situation becomes more interesting and complex when a time-dependent modulation of either the lattice or the trapping potential is employed. As the parabolic lattice can be effectively described by a quantum pendulum. Thus, the driven parabolic lattice represents a parametric oscillator.

In this chapter, we discuss Bloch dynamics in a parametrically driven parabolic optical lattice. We mainly focus on the case where a time-periodically modulated parabolic trap drives the lattice. This case refers to as a parametrically-forced parabolic optical lattice where the driving provides a spatially- and temporally-modulated force. As a near-resonant temporal modulation of a constant force in the presence of an optical lattice drives super-Bloch oscillations. Accordingly, we employ a resonant driving of Bloch-like oscillations and different dynamics which are similar but characteristically different from super-Bloch oscillations.

5.1 Parametrically Driven Optical Lattices

Parametric oscillators are widely studied across various fields of physics and engineering. They play a crucial role in quantum optics, condensed matter physics, and nonlinear dynamics. Examples include parametrically driven harmonic oscillators [135], Josephson junctions in superconducting circuits [136], and parametrically amplified signals in opto-mechanical systems [137]. These oscillators are characterized by the periodic modulation of certain system parameters, leading to rich dynamical behavior, including resonance, instability, and synchronization phenomena.

Considering a 1D-optical lattice which can be described by the Hamiltonian

$$\hat{H} = \frac{p^2}{2M} + V_0 \cos(2k_L x), \tag{5.1}$$

one may introduce the following dimensionless quantities

$$t' = \omega t, \quad x' = 2k_L x, \quad p' = \frac{2k_L}{M\omega} p, \quad V_0' = V_0 \left(\frac{4k_L^2}{M\omega^2} \right). \tag{5.2}$$

With these definitions the dimensionless effective Hamiltonian

$$H' = \frac{p'^2}{2} - V_0' \cos(x'), \tag{5.3}$$

corresponds to a mathematical pendulum [103]. When either the amplitude or phase of the optical lattice is modulated in time, it behaves as a driven pendulum, and thus it is a parametric oscillator. Classically, driven harmonic oscillators are categorized as parametrically-excited or parametrically-forced oscillators, depending on whether a time-dependent force influences the pendulum's momentum or if its range of motion is enhanced by shaking the pivot [135]. The latter case is commonly known as the Kapitza pendulum [138]. In terms of the lattice problem, the amplitude modulated optical lattice behaves as a parametrically excited oscillator [88, 139]. On the other hand, a phase-modulated optical lattice induces acceleration, directly affecting the momentum term [121]. Therefore, a phase-modulated optical lattice is classified as a parametrically forced oscillator.

As described in Section 4.2, the parabolic optical lattice within the single-band tight-binding representation can also be described by a mathematical pendulum, given by Eq. (4.10). In the context of parabolic lattice, the pendulum momentum corresponds to the position coordinate while the angular position of the pendulum represents the quasimomentum. Thus, the role of position and momentum is interchanged. In this case, a parametric force is achieved by modulating the parabolic trapping potential, which we later show to offer a unique advantage for observing dynamics compared to parametric excitation.

5.2 Chirped Bloch-Harmonic Transport

Let us consider the tight-binding lattice driven by a time-periodically modulated parabolic trapping potential. The Hamiltonian is

$$\widehat{H}_{TB} = -J \sum_{j=-\infty}^{\infty} \left(|j+1\rangle\langle j| + |j\rangle\langle j+1|\right) + \Omega(t) \sum_{j=-\infty}^{\infty} j^2 |j\rangle\langle j|, \tag{5.4}$$

where the time-dependent trapping energy is defined as $\Omega(t) = \Omega_0(1 + \alpha \sin(\omega t + \phi))$, with α, ω, and ϕ representing the strength, frequency and initial phase of the drive, respectively.

Modulating the trapping potential at the Bloch frequency $\nu_B = 2\Omega_0 j_0/\hbar$ gives rise to an oscillatory transport on top of Bloch oscillations, as shown in Fig. 5.1 for $\phi = 0$. These dynamics resemble super-Bloch oscillations although the quasimomentum-space dynamics reveal that the relative phase in this case performs quick oscillations around the center of Brillouin zone rather than transversing across all the quasimomentum values. The quick oscillations of the quasimomentum indicate a relatively small amplitude of oscillations in real-space as compared to super-Bloch oscillations. The relative phase appears due to spatial variations of the Bloch frequency which develops from the coupling between real-space and quasimomentum-space dynamics as indicated by the Modified acceleration relation

$$\frac{dk(t)}{dt} = -\left(\frac{2\Omega(t)}{a^2\hbar}\right) x(t). \tag{5.5}$$

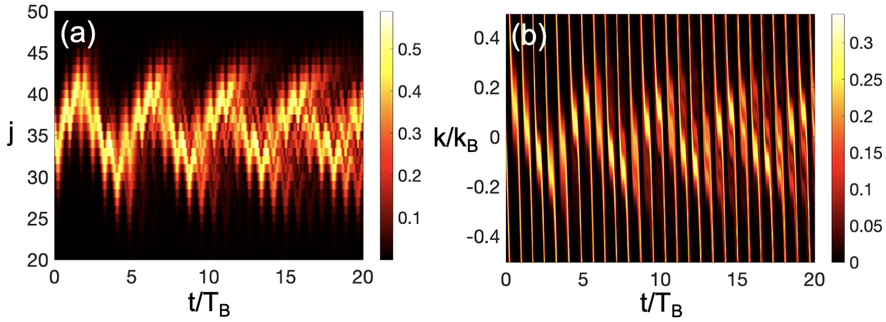

Figure 5.1: Absolute values of the wave packet evolution in real and quasimomentum space. Chirped Bloch-harmonic transport for a broad Gaussian initial state with mean at $j_0 = 30$ and width $\sigma_0 = 2.23$ are shown. The parametric values are $J = 2.4 \times 10^{-4} E_R$, $\Omega_0 = 3.2 \times 10^{-4} E_R$, $\alpha = 1$, $\phi = 0$ and $\hbar\omega = \hbar\nu_B = 2\Omega_0 j_0 = 0.0192 E_R$. The figure is adapted from Ref. [79] with permission.

The spatial variations in Bloch frequency manifest as a variable detuning and thus an oscillatory transport is achieved even in the absence of an external detuning. To classify these dynamics we coin the term chirped Bloch-harmonic transport (CBHT). These dynamics can also exhibit additional dephasing due to spatial anharmonicity. This dephasing leads to decay and later revivals of coherent oscillations, though the decay and revival times differ significantly from those in the static system.

5.2.1 Drive-Phase-Dependent Bloch Dynamics

Next we show that different chosen initial drive phases significantly effect CBHT. The dynamics for different phase shifts are shown in Fig. 5.2. We see that a $\phi = -\pi/2$ phase shift leads to fully coherent CBHT, as shown in Fig. 5.2(a). Such a driving of the system reveals a fast relative phase which appears more confied near the center of the Brillouin zone, see Fig. 5.2(b). Thus the amplitude of the CBHT is further reduced. This results in a suppressing of dephasing and thus coherent CBHT is achieved. The dynamics for an opposite drive phase $\phi = \pi/2$ are shown in Fig. 5.2(c) where rapid large space asymmetric spreading of wave packet is observed. The spreading ceases in few Bloch periods. As the wave packet stretches in space, two distinct regions of unequal density emerge. On one end, where the density is higher and aligned with the direction of the force, the wave packet exhibits purely breathing dynamics. On the opposite end, with lower density, it undergoes anharmonic breathing. These breathing oscillations, occurring half a Bloch period apart, transfer the maximum density to a revival of coherent Bloch oscillations within just six Bloch periods. Additionally, all three types of oscillations coexist simultaneously, with periodic variations in density. Fig. 5.2(d) shows the appearance of modulations near the edges of the Billouin zone with a weak relative phase. Modulations contributing to opposite momenta are also the cause of the spreading dynamics, where the relative phase is the reason for asymmetry.

We note that the spreading dynamics are similar to the ballistically spreading dynamics

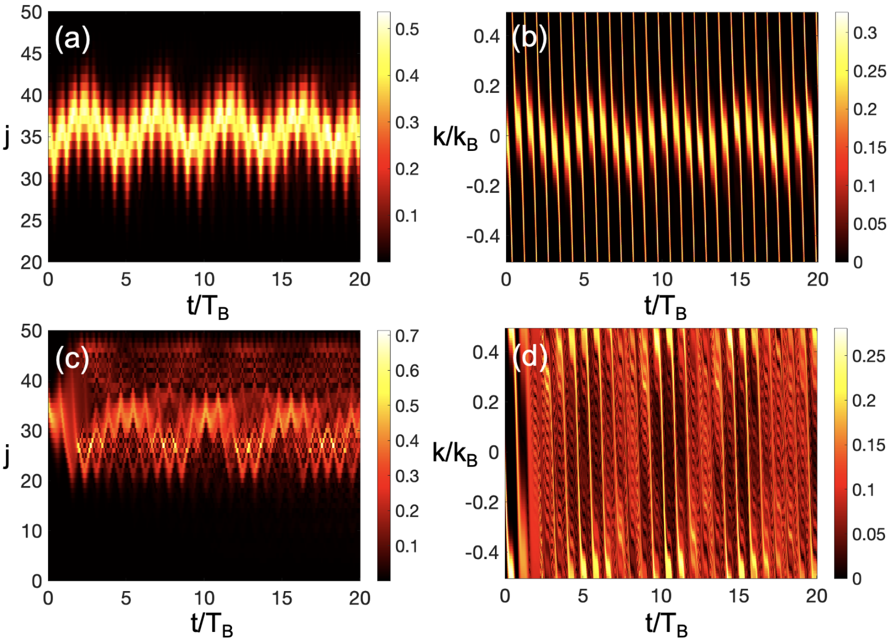

Figure 5.2: Drive-phase-dependent dynamics. Absolute values of the wave packet evolution in real and quasimomentum space for the drive phases $\phi = -\pi/2$ (a-b) and $\phi = \pi/2$ (c-d), exhibiting coherent CBHOs and asymmetric spreading oscillations, respectively. A Gaussian wave packet as in 5.1 is evolved under same parameters, with only the drive phase being changed. The figure is adapted from Ref. [79] with permission.

shown in Fig. 3.5(c-d). However, in a spatially-homogenous driven lattice ballistic spreading appears for both the opposite parity drive phases $\phi = \pm\pi/2$. On the contrary, in the spatially-inhomogeneous lattice with a parabolic trap an asymmetric spreading is obtained for $\phi = \pi/2$, while at $\phi = -\pi/2$ coherent CBHT is achieved.

5.2.2 Local Acceleration Model with Time-Dependent Driving

In this section, we provide a simple analytical model to describe the oscillatory dynamics. Our analytical model is based upon the acceleration relation (5.5), which holds for the weak trapping limit such that the wave packet moves slowly and coherently from one site to another. The acceleration relation is rewritten as

$$k_c(t) = k_c(0) - \frac{2}{a^2}\int_0^t \Omega(t')x_c(t')\,dt'. \tag{5.6}$$

Keeping in view, the coherent harmonic oscillatory transport around a fixed initial position j_0 in real space and assuming that the Bloch frequency remain almost constant during a Bloch oscillation, one may the ansatz $x_c(t) = x_c(0) + \Delta x \cos(\delta\nu t + \gamma)$. Substituting the ansatz in

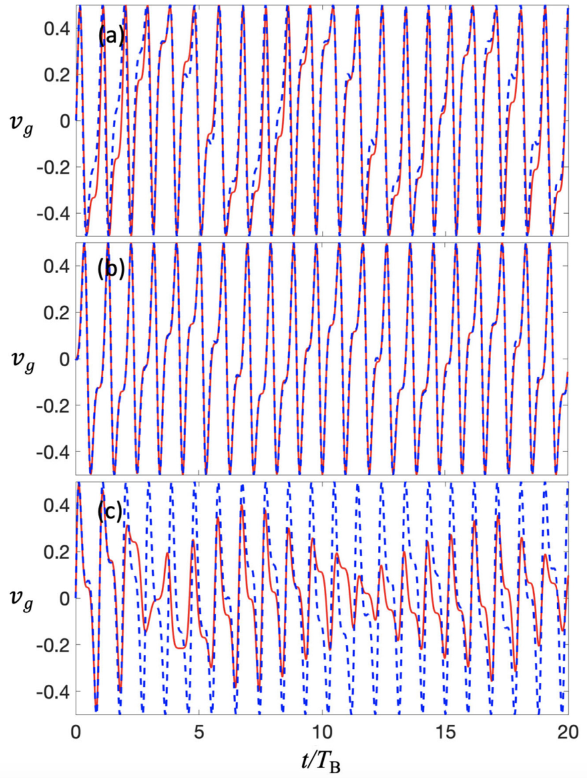

Figure 5.3: Group velocity as a function of time for (a) $\phi = 0$, (b) $\phi = -\pi/2$, and (c) $\phi = \pi/2$. The red line represents the result of numerical calculations, while the dashed blue line depict the dependence obtained from Eq. (9). For (a) the parametric values are $\Delta x = 2.8a$ and $\hbar\delta\nu = 0.14T_B$, while in (b) and (c) $\Delta x = 1.0a$. All the other parameters are the same as stated in Fig. 5.1. The figure is adabted from Ref. [79] with permission.

Eq. (5.6) we get

$$\begin{aligned} k_c(t) &= k_c(0) - \frac{2\Omega_0}{a^2}\left[x_c(0)t + \frac{\Delta x}{\delta\nu}(\cos(\delta\nu t + \gamma) - \cos(\gamma))\right] \\ &+ \frac{2\alpha\Omega_0}{a^2}\left[\frac{x_c(0)}{\omega}(\cos(\omega t + \phi) - \cos\phi)\right. \\ &\left.\mp \frac{\Delta x}{2}\frac{\sin((\omega \pm \delta\nu)t + \phi \pm \gamma) - \sin(\phi \pm \gamma)}{\omega \pm \delta\nu}\right]. \end{aligned} \tag{5.7}$$

where $\delta\nu$ represents the frequency of CBHT and γ denote its phase. As these parameters belong to our ansatz, their values are extracted numerically for further analysis.

To test the above analytical expression, we consider the tight-binding group velocity which is determined perturbatively as

$$v_g = \frac{1}{\hbar}\frac{\partial E(k)}{\partial k}\Big|_{k=k_c(t)} = \frac{2Ja}{\hbar}\sin\left(k_c(t)a\right)\ . \tag{5.8}$$

In Fig. 5.3, we plot Eq. (5.8) and compare it with the numerically calculated group velocity. One can see that the approximate expression closely retraces the relative phase and effectively describes CBHT. For the case of a $\phi = -\pi/2$ drive phase, it shows very good agreement with the numerical results. However, a disagreement arises for $\phi = \pi/2$ due to spreading oscillations and multimode dynamics at this drive phase, which go beyond the scope of semiclassical group velocity. Overall, Eq. (5.8) successfully captures and explains the key aspects of our findings.

Dynamics for Varying Initial Conditions

In this section, we present additional numerical results for the driven Bloch dynamics analyzed in our studies. We investigate how the dynamics are affected by variations in the initial width and initial position of the wavepacket considering the quadratic level spacing provided by the parabolic trap. Moreover, we demonstrate that changing the initial position is equivalent to modifying the Bloch frequency, allowing us to explore CBHT at secondary resonances. Additionally, we examine high-frequency drives and show that, under such conditions, the driven dynamics reduce to Bloch-like oscillations in the stationary system.

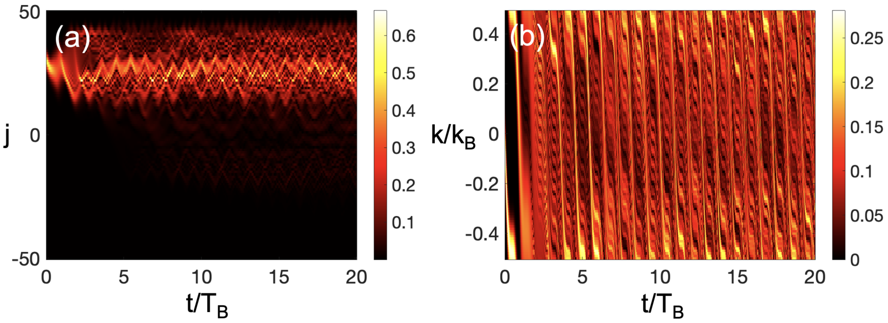

Figure 5.4: Absolute values of the wave packet evolution in real and quasimomentum space for the drive phase $\phi = \pi/2$. Dipole oscillations resulting from asymmetric wave packet spreading. A Gaussian wave packet as in Fig. 5.1 is evolved under same parameters, except that it now starts its journey from a different initial position, $j_0 = 30$.

Figure 5.9 displays our first result, where we analyze the dynamics large amplitude spreading dynamics by choosing a different initial position of the Gaussian wave packet. The fact that this position is relatively closer to the separatrix, $x_c \simeq 17a$, makes it possible for the evolving wave packet to reach the domain of dipole oscillations and mixed dynamics as soon as it comes into the vicinity of the separatrix. In this domain, the affected wave packet moves past the center of the parabolic lattice and starts performing a mix of breathing and dipolar dynamics with a difference of half a Bloch period. This is demonstrated in Fig. 5.9(a), where the wave packet initially performs asymmetric spreading dynamics, as already shown in Fig. 5.9(c-d). However, after a few Bloch periods, a small fraction of density reaches the separatrix, from where it enters the regime of dipolar and breathing dynamics. The dipole oscillating part moves towards its outset again, and in its path, it interferes with subsequent dipole-oscillating fractions. Thus, quantum interferences further complicate the dynamics.

This result suggests that, for driven dynamics emerging near the separatrix, a complex mix of Bloch oscillations, driven Bloch dynamics, and dipole oscillations can be seen. The related k-space dynamics, shown in Fig. 5.9(b), further highlight the complex dynamics. Linear evolution of quasimomentum and metastable momentum is recognizable initially. However, after the first couple of Bloch periods, the next evolution is quite complicated. Nonetheless, a nonconstant relative phase is still visible near the edges of the Brillouin zone. Due to the already very complex multimode dynamics, the oscillatory evolution of dipole oscillating fractions of the wave packet is not discernible in this figure.

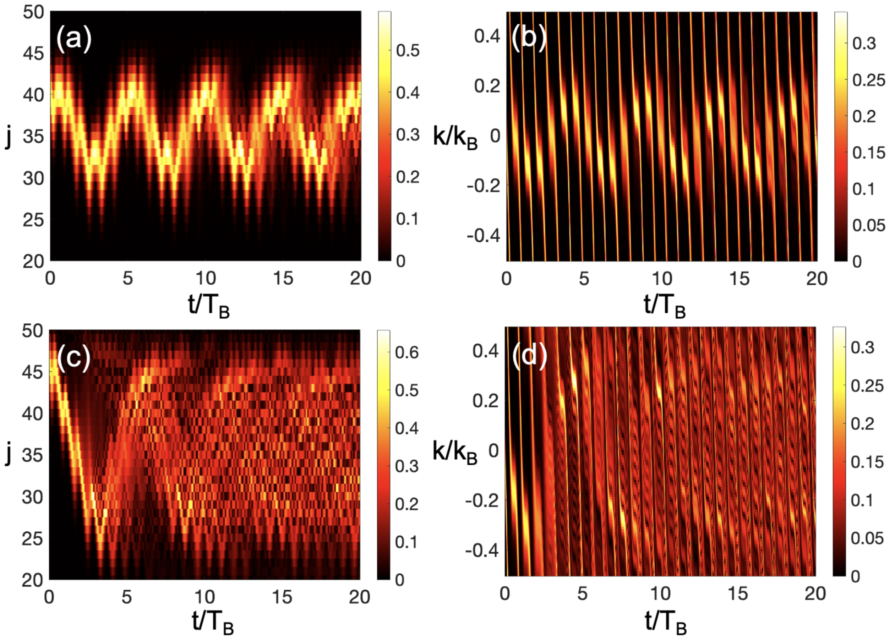

Figure 5.5: Absolute values of the wave packet evolution in real and quasimomentum space for the drive phase $\phi = 0$. Chirped Bloch-harmonic transport around resonant energy state. A Gaussian wave packet as in Fig. 5.1 is evolved under same parameters, except that it now starts its journey from varying initial positions, $j_0 = 40$ (a-b) and $j_0 = 46$ (c-d).

Next, we investigate CBHT for varying initial positions of the wave packet. Figure 5.5(a-b) demonstrates CBHT for a Gaussian wave packet placed at $j_0 = 40$, where, as before, the driving frequency is in resonance with the Wannier-Stark-like state localized at $j_0 = 35$. Under these conditions, CBHT emerges centered around the resonant location $j_0 = 35$, as seen in Fig. 5.5(a). These dynamics remain coherent initially but later undergo dephasing; however, the dephasing times differ from those observed in Fig. 5.1. The k-space dynamics, displayed in Fig. 5.5(b), highlight the evolving relative phase, which exhibits an oscillatory profile. Additionally, dephasing leads to a broadening of the k-space dynamics.

Taking the wave packet further away from the resonant site induces spreading along with CBHT. This is illustrated in Fig. 5.5(c-d) for $j_0 = 46$. The spreading leads to anharmonic breathing, which rapidly becomes affected due to interference with the main density that performs dephased CBHT, and dephases further due to spreading and subsequent interferences. The dephasing leads to a quick collapse of coherent dynamics, as shown in Fig. 5.5(c). The reasons for this quick collapse can be inferred from the k-space evolution shown in Fig. 5.5(d), which reveals a relative phase exploring almost entire Brillouin zone. Thus, with metastable momenta acquiring large quasimomentum values, large-amplitude oscillations occur in real space, and for extensive transport across the lattice, spatial inhomogeneities play a role, leading to dephased dynamics. Thus, the coupling between coordinate position and quasimomentum, as described by the modified acceleration theorem, plays a significant role.

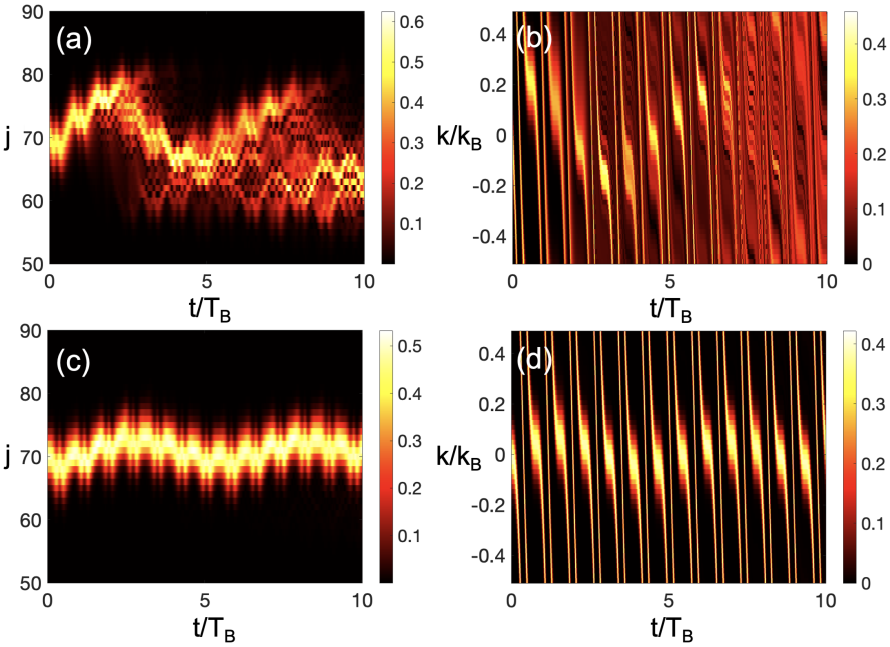

Figure 5.6: Absolute values of the wave packet evolution in real and quasimomentum space for the drive phase $\phi = 0$ (a-b) and $\phi = -\pi/2$ (c-d). Chirped Bloch-harmonic transport at a secondary resonance. A Gaussian wave packet as in Fig. 5.1 is evolved under same parameters, except that it now starts its journey from varying initial positions, $j_0 = 70$.

As the wave packet is set further away from the resonant site, it moves closer to a secondary resonant state, near which the dynamics become increasingly coherent. In Fig.5.6(a-b), we show the dynamics for a Gaussian wave packet with mean $j_0 = 70$. The Bloch frequency at this spatial location is twice the driving frequency. Consequently, the modulation interacts with Bloch oscillations at every other period. As a result, the wave packet undergoes Bloch oscillations, with transport being generated every other period, as shown in Fig.5.6(a). This leads to CBHT, however these dynamics dephase within a few Bloch periods due to the metastable momentum interacting with Bloch oscillations near the center of the Brillouin zone. Here, the wave packet experiences momentum in opposite directions, causing it to spread. The k-space dynamics in Fig. 5.6(b) confirm this effect, as well as the evolving relative phase of CBHT, which quickly becomes unrecognizable due to dephasing.

To further illustrate the sub-harmonic response, we consider the drive phase $\phi = -\pi/2$, at which coherent CBHT was previously observed. The results shown in Fig. 5.6(c-d) display sub-harmonic CBHT. Coherent dynamics in real space and a consistent oscillatory relative phase are revealed in the k-space dynamics. Note that in these cases, the period of CBHT is twice that of CBHT at a primary resonance.

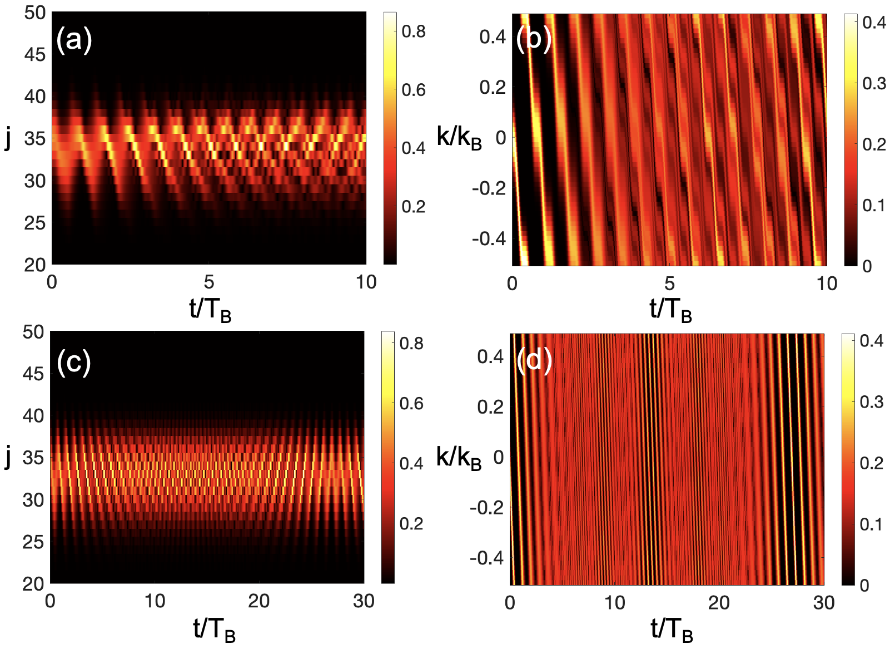

Figure 5.7: Absolute values of the wave packet evolution in real and quasimomentum space for the drive phase $\phi = 0$. Bloch dynamics for rapid driving. A Gaussian wave packet as in Fig. 5.1 is evolved under same parameters, except that a rapid driving is now used, $\omega = 2\nu_B$ (a-b) and $\omega = 10\nu_B$ (c-d).

Next, we illustrate the driven dynamics at high-frequency driving in Fig. 5.7. When the system is subjected to a driving frequency of $\omega = 2\nu_B$, the modulation slightly modifies the dynamics of the stationary system, as shown in Fig. 5.7(a). Here, the wave packet exhibits Bloch-like oscillations with additional modulations induced by the driving, which subtly alter the density distribution over time. The corresponding quasimomentum-space dynamics in Fig. 5.7(b) reveal a rapid emergence of modulation effects. The k-space evolution highlights two distinct oscillatory phases appearing on top of the underlying BOs, which are eventually

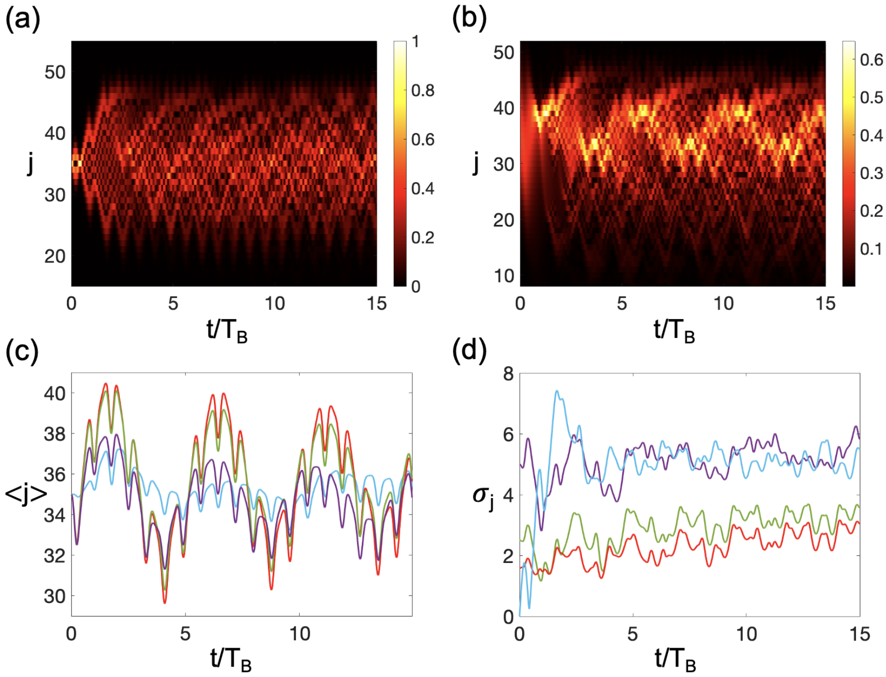

Figure 5.8: Chirped Bloch-harmonic transport for different initial width choices, $\sigma = 0.0446$ (a) and $\sigma = 7.071$ (b). Evolution of the average position (c) and width variance (d) for initial widths $\sigma = 0.0446, 2.236, 3.536$, and 7.071, depicted in blue, red, green, and purple, respectively. These calculations are performed for a Gaussian wave packet, as taken in Fig. 5.1, using the same parameters and with the drive phase set to $\phi = 0$. The figure is adapted from Ref. [79] with permission.

dominated by dephasing. These modulations lead to a fast oscillatory behavior that can be averaged out over time. Accordingly, at sufficiently high driving frequencies, as demonstrated in Fig. 5.7(c-d), the dynamics become almost entirely unaffected, with sustained Bloch-like oscillations in both real and k-space, indicating that the influence of the drive effectively vanishes.

Keeping in view the lattice anharmonicity and the space-dependent variations observed in the dynamics, it is intuitive that the dynamics changes significantly for different initial widths of the wave packet. We demonstrate this effect in Fig. 5.8, where we plot the CBHT dynamics for various initial widths. Figure 5.8(a) shows the real-space evolution of a sharply localized wave packet. This reveals that, similar to super-Bloch oscillations, a sharply localized initial wave packet also exhibits breathing dynamics at first. However, in this case, the wave packet's contraction takes place at half the CBHT period, where it partially contracts remaining away from its outset. This reconstruction of the initial width is followed by successive expansions and contractions that occur in an oscillatory manner around the initial position. Due to this partial breathing motion, the overall dynamics dephase after a few Bloch periods, leading to a collapse. Similarly, for a much wider initial state, the CBHT also exhibits partial spreading motion. Figure 5.8(b) shows that a wide wave packet experiences phase shifts due to lattice anharmonicity, causing it to become sharply localized at the first Bloch period. This narrower wave packet then displays a highly asymmetric long-range breathing motion where a smaller fraction, that observes further splitting, rapidly accelerates in the direction of the force, while a larger portion breathes slowly. In a manner similar to a harmonic oscillator, the wave packet successively transfers its maximum density to new positions, and numerous smaller fractions perform large spatial oscillations. The breathing is eventually followed by complex, multimode dynamics, where a significantly larger portion of the wave packet undergoes CBHT atop a background of mixed motion. Thus, CBHT suffer heavily for very small or large initial widths. To support this observation, in Fig. 5.8(c) and (d) we plot the time-dependence of the mean position and the width of the wave packet for various initial widths. Figure 5.8(c) displays the time evolution of the wave packet's mean position for different initial widths. In this figure, the red curve (corresponding to $\sigma = 2.236$) depicts sustained CBHT with minimal dephasing, indicative of optimal behavior at $\phi = 0$ drive phase . In contrast, a very narrow initial state (represented by the blue curve with $\sigma = 0.0446$) exhibits the strongest decay of CBHT. Meanwhile, the green curve (for $\sigma = 3.536$), shows more pronounced dephasing associated with CBHT, and the extreme case of a wide wave packet shown by the purple curve with $\sigma = 7.071$ indicate a significant decay of CBHT. Furthermore, Fig. 5.8(d) presents the time evolution of the wave packet's width. Once again, the red curve demonstrates that an intermediate width yields only slow-gradual increase while indicating sustained CBHT, whereas the blue curve indicates a rapid high increase in width. The green and purple curves reveal an initial contraction followed by erratic expansion. Together, these results highlight that both the average position and the width variance remain most stable when the initial width is neither too narrow nor too broad. Consequently, sustained CBHT emerges within a moderate width window that is far from the extreme width values leading to either sharply narrow or overly wide wave packets.

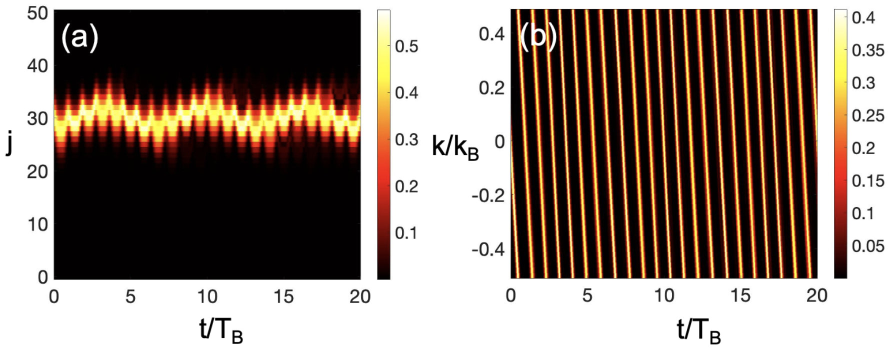

Figure 5.9: Absolute values of the wave packet evolution in real and quasimomentum space. Coherent chirped Bloch-harmonic transport for a lattice amplitude modulation at $\phi = -\pi/2$. The parametric values are kept the same as in Figure 5.1 for comparison.

5.3 Driven Bloch Dynamics in an Amplitude Modulated Lattice

In this section, we highlight the difference in the mechanism by which driven Bloch dynamics manifest in amplitude-modulated lattices and force-modulated lattices. While both cases exhibit similar dynamics in real space, a crucial distinction arises in the quasimomentum-space evolution. Specifically, in the force-modulated system, a well-defined oscillatory phase appears in the quasimomentum-space dynamics due to the interaction between Bloch oscillations and the modulation. However, the relative phase is implicit when the lattice amplitude is periodically modulated. To demonstrate this, we consider a time dependence of the tunneling parameter $J'(t) = J(1 + \alpha \sin(\omega t + \phi))$ in Eq. (5.4), and suppress the time-dependence of trapping energy.

Figure 5.9 demonstrates that while the real-space wave packet exhibits coherent dynamics, similar to CBHT observed with the trap modulation, the quasimomentum-space dynamics show linear evolution of quasimomentum, reflecting coherent Bloch oscillations and thus provide no information about the interaction with the modulation. Consequently, this different manifestation of driven dynamics sets the two driving scenarios apart. The fundamental reason lies in the nature of the modulation. As with lattice amplitude modulation, the driving induces a periodically modulated tunneling, the modulation effects are not manifested in the quasimomentum-space dynamics.

Floquet Analysis of Driven Bloch Dynamics

6

Floquet theory is a well-known mathematical formalism used to study the behavior of time-periodic systems [140]. In quantum systems, it is particularly useful for understanding the dynamics of systems subjected to periodic modulation [141]. Although generic time-periodic systems are nonintegrable, the Floquet formalism enables a non-perturbative treatment of their spectral and dynamical properties through the concept of Floquet states and quasienergies [142].

In this chapter, we analyze driven Bloch dynamics by employing Floquet theory. Although the Floquet states strictly depend upon the switch-on protocols for the time-periodic modulation [143], using the customary example of an instantaneous turn-on, we obtain the Floquet spectrum of the resonantly driven parabolic optical lattice [89].

The Floquet states are often classified based on their analogy to the dynamics of the classical counterpart of the driven system [144]. Accordingly, we compare and contrast the dynamics of Floquet states to those of a driven pendulum to which the driven parabolic lattice effectively maps. The driven pendulum exhibits regular dynamics associated with nonlinear resonances that are visualized as regular islands in a partly-chaotic phase space [145]. The quantum dynamics corresponding to a nonlinear resonance can be effectively described by the Mathieu equation, thereby mapping the time-dependent system onto a stationary system [146]. Thus, we demonstrate the emergence of effective states from the unperturbed states [90].

Floquet states are characterized by time-independent coefficients, ensuring that their occupation probabilities remain constant throughout the evolution. If the drive is turned on with different phases, the occupation probability distribution changes, leading to the population of states with different characteristics. We demonstrate in detail that it is the varying occupation of Floquet states that gives rise to the drive-phase-dependent dynamics presented in the previous chapter [79].

6.1 Floquet States and their Properties

Let us consider a time-periodically driven system represented by the Hamiltonian $H(t) = H(t+T)$. Then, the time-dependent Schrödinger equation

$$i\hbar\frac{\partial}{\partial t}|\psi(t)\rangle = H(t)|\psi(t)\rangle, \tag{6.1}$$

possesses a complete set of solutions given by the Floquet states $|\psi_\ell(t)\rangle$, that are separable into the product of a phase factor $e^{-i\varepsilon_\ell t/\hbar}$ and time-periodic Floquet functions $|u_\ell(t+T)\rangle = |u_\ell(t)\rangle$

such that

$$|\psi_\ell(t)\rangle = e^{-i\varepsilon_\ell t/\hbar}|u_\ell(t)\rangle, \tag{6.2}$$

where ℓ represents the quantum number labeling the states and the real quantity ε_ℓ is analogous to the eigenvalues of a time-independent system, commonly referred to as the quasienergy.

Substituting Eq. (6.2) into the Schrödinger equation yields

$$\left(H(t) - i\hbar\frac{\partial}{\partial t}\right)|u_\ell(t)\rangle = \varepsilon_\ell|u_\ell(t)\rangle, \tag{6.3}$$

which determines the Floquet functions $|u_\ell(t)\rangle$ and the quasienergy ε_ℓ in a suitable extended Hilbert space. Taking on a particular solution $|u_\ell(t)\rangle$ to Eq. (6.3) with eigenvalue ε_ℓ, the function $e^{im\omega t}|u_\ell(t)\rangle$, where ω is the driving frequency and $m = 0, \pm1, \pm2, \ldots$, remains a valid solution to the eigenvalue equation, preserving the same periodicity while shifting the eigenvalues by $m\hbar\omega$. Consequently, the quasienergy is not considered as a single value ε_ℓ but rather as a set of an equally spaced ladder $\varepsilon_\ell + m\hbar\omega$. As a result, the quasienergy spectrum extends infinitely in both directions, forming Brillouin zones of energies, with each Floquet state's quasienergy having a representative within every Brillouin zone of width $\hbar\omega$. This also leads to an irregular ordering of Floquet states based on the magnitude of their quasienergies.

An alternative formulation exists in terms of the one-period evolution operator, which, in terms of the Floquet solutions (6.2), is expressed as [147]

$$U(T,0) = \sum_\ell e^{-i\varepsilon_\ell T/\hbar}|u_\ell(T)\rangle\langle u_\ell(0)| = \sum_\ell e^{-i\varepsilon_\ell T/\hbar}|u_\ell(0)\rangle\langle u_\ell(0)|, \tag{6.4}$$

where in the second equality the time-periodicity of Floquet functions $|u_\ell(t)\rangle$ is employed. Thus, the eigenvectors of $U(T,0)$ corresponds to the Floquet states at t=0, $|\psi_\ell(0)\rangle \equiv |u_\ell(0)\rangle \equiv |\ell\rangle$. The states after one complete period are

$$|\psi_\ell(T)\rangle = U(T,0)|\psi_\ell(0)\rangle = e^{-i\varepsilon_\ell T/\hbar}|\psi_\ell(0)\rangle. \tag{6.5}$$

The eigenvalues η_ℓ obtained from $U(T,0)$ provide the quasienergies through the relation $\varepsilon_\ell = i\hbar\log(\eta_\ell)/T$ [148]. Since all eigenvalues of the unitary operator $U(T,0)$ lie on the unit circle, it can be expressed as

$$U(T,0) = e^{-iGT/\hbar}, \tag{6.6}$$

where G is a self-adjoint operator having real eigenvalues with the dimension of an energy. Keeping in view the periodic ladder structure of quasienergies, the definition of $U(T,0)$ is not unique. Despite this ambiguity, the presence of G allows for the introduction of a unitary operator

$$P(t) = U(t,0)e^{iGt/\hbar}, \tag{6.7}$$

which is periodic in time $P(t+T) = P(t)$. This lead us to define the time evolution operator as

$$U(t,0) = P(t)e^{-iGt/\hbar}. \tag{6.8}$$

The above factorization of the time-evolution operator embodies the fundamental idea of the

Floquet theorem for quantum systems with periodic time dependence [121,140,149,150]. Thus, a wave function $|\phi(0)\rangle$ evolves according to

$$\begin{aligned}|\Phi(t)\rangle &= U(t,0)|\Phi(0)\rangle \\ &= \sum_{\ell} c_{\ell} P(t) e^{-iGt/\hbar}|\ell\rangle \\ &= \sum_{\ell} c_{\ell} P(t)|\ell\rangle e^{-i\varepsilon_{\ell}t/\hbar} \\ &= \sum_{\ell} c_{\ell}|u_{\ell}(t)\rangle e^{-i\varepsilon_{\ell}t/\hbar}, \end{aligned} \tag{6.9}$$

where the Floquet functions are introduced as $|u_{\ell}(t)\rangle = P(t)|\ell\rangle$, the coefficients are given by $c_{\ell} = \langle \ell|\Phi(0)\rangle$ which are time-independent and, therefore, generally provide the constant occupation probabilities $|c_{\ell}|^2$. Hence, any solution to the Schrödinger equation can be expressed as a superposition of Floquet states.

In the following section, we analyze the dynamics of a resonantly driven parabolic optical lattice by examining and comparing its classical and Floquet description. We apply Eq. (6.9) for various drive phases and show how variations in occupation probability distributions lead to distinct dynamics.

6.2 Floquet Dynamics of Driven Parabolic Optical Lattices

Let us again refer to the single-band tight-binding lattice driven by a periodically modulated trapping potential. If the trapping potential is time-periodically modulated with a frequency ω and a relative modulation strength α, the combined system is described by the Hamiltonian

$$\widehat{H}(t) = \widehat{H}_0 + \widehat{H}_{int}(t), \tag{6.10}$$

with

$$\widehat{H}_0 = -J \sum_{j=-\infty}^{\infty} (|j+1\rangle\langle j| + |j\rangle\langle j+1|) + \Omega_0 \sum_{j=-\infty}^{\infty} j^2 |j\rangle\langle j|, \tag{6.11}$$

and

$$\widehat{H}_{int}(t) = \alpha\Omega_0\, f(t)\, \sin(\omega t + \phi) \sum_j j^2 |j\rangle\langle j|, \tag{6.12}$$

where the dimensionless function $f(t)$ represents a switch-on function describing the way the drive is turned on within a time interval from $t_i = 0$ to t_f, such that

$$f(t) = \begin{cases} 0\,, & t < 0 \\ 1\,, & t > t_f\,. \end{cases} \tag{6.13}$$

For example, the extreme case of a sudden turn-on is represented by a Heaviside function function

$$f(t) = \Theta(t)\,. \tag{6.14}$$

Additionally, defining the instant $t_i = 0$ as the turn-on moment gives physical significance to the drive phase ϕ.

6.2.1 Classical Pendulum Dynamics

Let us first describe the classical counterpart of the driven system. Expressing the Hamiltonian system (6.10) in the Bloch basis, leads us to write

$$\widehat{H}(t) = \; -2J\cos\left(\widehat{k}a\right) + \Omega(t)(\widehat{x}/a)^2. \tag{6.15}$$

The classical dynamics generated by this Hamiltonian can be described by mapping it to a mathematical pendulum. In this regard, we treat the operators $\widehat{x}$ and $\widehat{k}$ as continuous variables x and k, and note that the product kx remains dimensionless. However, since the product of two canonically conjugate variables must have the dimension of action, we employ the de Broglie relation $p = \hbar k$, that takes us to the Hamiltonian function

$$H_{cl}(t) = \; -2J\cos(p\lambda) + \Omega(t)(x/a)^2. \tag{6.16}$$

where $\lambda = a/\hbar$. This expression clearly represents a driven pendulum; however, the usual roles of position and momentum are interchanged. Additionally, the system behaves as if it has a time-dependent effective mass, varying periodically as $1/\Omega(t)$. The resulting equations of motion are

$$\begin{aligned} \dot{p} &= -\frac{2\Omega(t)}{a^2}\,x, \\ \dot{x} &= 2J\lambda\sin\left(p\lambda\right)\,. \end{aligned} \tag{6.17}$$

In the study of Hamiltonian systems with periodic time dependence, a common approach is to analyze the dynamics emerging from the above set of equations using stroboscopic Poincaré surfaces of sections. For this, the coupled evolution of position and momentum coordinate is determined numerically starting with an appropriately chosen set of initial conditions (p_i, x_i) in phase space. The resulting trajectories are then sampled at intervals corresponding to the driving period $T = 2\pi/\omega$. The stroboscopic Poincaré sections obtained for the system (6.17) are displayed in Fig. 6.1 for varying values of the drive strength α. For a significantly weak driving strength $\alpha = 0.01$, for which $\Omega(t) \approx \Omega_0$, the dynamical equations reproduce the well-known phase portrait of the undriven pendulum, as shown in Fig. 6.1(a). We note that as the driving strength is raised, the phase space trajectories, which are in $1:1$ resonance with the drive start to curl around and give rise to new fixed points in addition to previous ones. This is illustrated for $\alpha = 0.25$ in Fig. 6.1(b), where the resonance-induced fixed points appear in pairs at $x/a \simeq \pm 35$ due to resonance effect on both sides of the parabolic lattice. The emergence of resonance-induced fixed points, (at least) one hyperbolic and one elliptic fixed point, is in accordance with the Poincaré-Birkhoff theorem. As the drive strength increases further, a prominent chaotic region emerges, engulfing the separatrix of the undriven pendulum. Fig. 6.1(c) illustrates this scenario at a driving strength of $\alpha = 5$, where stochastic behavior begins to develop at the resonance-induced hyperbolic fixed points. The region of periodic orbits surrounding the elliptic fixed points remains well-ordered and is gradually overtaken by chaos

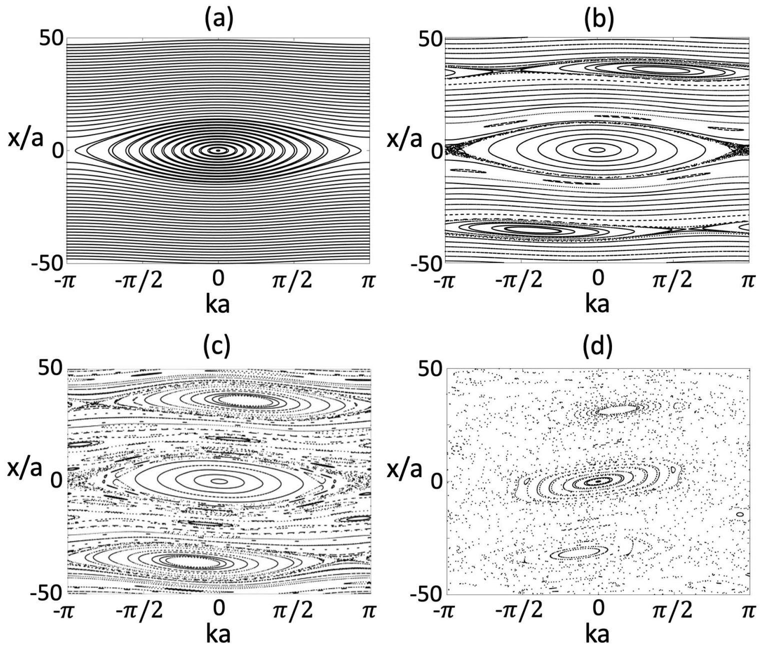

Figure 6.1: Stroboscopic Poincaré sections for the classical pendulum system (6.16) under strictly periodic driving at $f(t) = 1$, with parameters $J/\hbar\omega = 1.071$ and $\Omega_0/\hbar\omega = 0.0143$. The driving strengths are $\alpha = 0.01, 0.25, 1.00$, and 5.00 for panels (a)-(d), respectively. All sections are plotted at $t = -\phi/\omega \bmod 2\pi/\omega$. The figure is taken from [90] with permission.

as the driving strength increases, as depicted in Fig. 6.1(d) for $\alpha = 5$. At sufficiently strong driving, the chaotic region expands throughout the entire phase space, with the resonant fixed points, which encircle regular curves, becoming fully immersed in the chaotic sea [144].

6.2.2 Mathieu Approximation and Near-Resonant Floquet States

In order to form a connection with the classical dynamics and to build the basis for later discussion of phase-dependent occupation probabilities, we introduce the Mathieu approximation, which offers a general description of the system's characteristics at resonant driving.

The formal development of the Mathieu-approximation begins with the eigenenergies E_ℓ and eigenstates $|\varphi_\ell\rangle$ of the undriven system. The spectrum of energies for the stationary parabolic optical lattice is described in Sec. 4.2. The eigenstates are categorized as states resembling harmonic oscillator-eigenfunctions at low energy and states localized at positions $x \pm n_0 a$ in a Wannier-Stark-like manner at high energy. These high-energy states correspond to eigenvalues that are approximately equal to the on-site energy $\Omega_0 j_0^2$ and due to the spatial-symmetry of the trap these states appear in pairs. As the stationary system free from any external perturbations furnishes a minuscle energy splitting between high energy states, therefore the coupling between these states can be ignored. Thus, one can consider the states restricted to only one side of the parabolic lattice. In addition to this restriction, it is assumed that the energy spacing between consecutive levels varies slowly so that the first derivative can be taken as $E'_\ell \equiv E_{\ell+1} - E_\ell$. Further, suppose that there exists a certain eigennumber r, the energy of which is matched by the energy of the driving field, such that one can write,

$$E'_r = \hbar\omega. \tag{6.18}$$

Under these conditions, the following ansatz for the near-resonant Floquet states can be considered

$$|\psi(t)\rangle = e^{-iE_r t/\hbar} \sum_\ell c_\ell(t)\, |\varphi_\ell\rangle e^{-i(\ell-r)(\omega t+\phi-\pi/2)}. \tag{6.19}$$

The factor $e^{-i(\ell-r)(\phi-\pi/2)}$ ensures the synchronization of the Floquet states with the drive phase. Inserting this ansatz into the time-dependent Schrödinger equation gives [89]

$$i\hbar\, \dot{c}_\ell(t) + \frac{1}{2}(\ell-r)^2 E''_r c_\ell(t) = E_\ell c_\ell(t) + \Lambda V[c_{\ell+1}(t) + c_{\ell-1}(t)], \tag{6.20}$$

where $V = V_{\ell+1} \approx V_{\ell-1}$ are the off-diagonal matrix elements which are approximately constant near the potential minimum in the tight-binding approximation. Additionally, this involves approximating the energies using a second-order Taylor expansion, accounting for the quadratic level spacing of the parabolic lattice. Furthermore, in the spirit of the rotating-wave approximation, only the secular terms are retained. Note that these approximations are fairly justified within the context of the system under discussion.

Introducing the Fourier representation

$$c_\ell(t) = \frac{1}{\pi} \int_o^\pi dz f(z) e^{i(\ell-r)2z} e^{-iWt/\hbar} \approx f_{(\ell-r)}\; e^{-iWt/\hbar}, \tag{6.21}$$

where we also separate the time-dependent amplitudes into Fourier coefficients of a π-periodic function and a time dependent phase factor carrying energies W. The use of π-periodic functions directly takes us to the standard form of the Mathieu equation [97]

$$f''(z) + \frac{8W}{E''_r}\, f(z) - \frac{8V}{E''_r}\, f(z)\cos(2z) = 0. \tag{6.22}$$

Thus, the energies W are given by

$$W_m = \frac{E''_r}{8} \gamma_m(q), \tag{6.23}$$

where γ_m represents the Mathieu characteristic energies [97]

$$\gamma_m(q) = \begin{cases} a_m(q); & m = 0, 2, 4...... \\ b_{m+1}(q); & m = 1, 3, 5......, \end{cases} \tag{6.24}$$

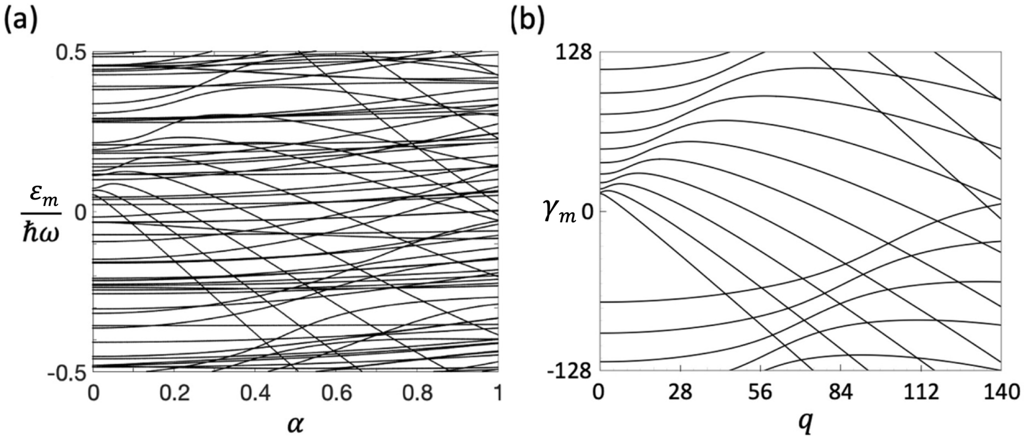

Figure 6.2: (a) One Brillouin zone of exact quasienergies, computed numerically and taken modulo $\hbar\omega$. The quasienergies are plotted as a function of the increasing driving strength under resonant driving condition. The curve with the strongest descent characterizes the ground state $m = 0$. The parameters remain the same as in Fig. 6.1. (b) Approximate quasienergies determined by Eq. (6.24). Note that the spectrum of quasienergies is (almost) two-fold degenerate and the states corresponding to the other representatives of energies that fold back on to the spectrum lie at the opposite arm of the parabolic lattice. The figure is taken from [90] with permission.

and $q = 8V/E_r''$ is the Mathieu-characteristic parameter.

Along the same lines, $f(z)$ are the π-periodic Mathieu functions and the Fourier coefficients of these functions plugged into Eq. (6.19) provide the near-resonant Floquet states

$$|\psi_m(t)\rangle = \sum_\ell f^m_{(\ell-r)} |\varphi_\ell\rangle e^{-i(\ell-r)(\omega t+\phi-\pi/2)} e^{-i(E_r+W_m t/\hbar)}. \tag{6.25}$$

Hence, the quasienergies are

$$\varepsilon_m = E_r + W_m, \quad \text{mod} \quad \hbar\omega, \tag{6.26}$$

where W_m corresponds to the energies of a pendulum associated with the Mathieu equation (Eq. (6.22)).

In Fig. 6.2 the numerically obtained quasienergies of the driven system and the Mathieu characteristic energies are displayed. Although the above procedure involves a series of approximations, the resulting predictions prove to be strikingly accurate. Thus, a near-resonant driving establishes a distinct hierarchy of states which are covered by the Mathieu equation. This way the time-dependent system reduces to an effective time-independent one. The emergence of these ordered Mathieu states holds important implications for the dynamics, which we will explore later in this chapter.

6.2.3 Phase Space Quantization

A correspondence between Floquet states and the classical phase space can be established through a semiclassical perspective. Specifically, one can quantize the classical phase space by applying Bohr-Sommerfeld-like quantization conditions to the periodic orbits surrounding the elliptic fixed points, yielding a semiclassical approximation to the Floquet states. In the extended phase space (k, x, t), which also incorporates time t, the periodic orbits form invariant tubes around the stable elliptic fixed point. The quantization condition [146, 151]

$$\oint_{\gamma_m} k\,dx = 2\pi\left(m + \frac{1}{2}\right), \quad m = 0, 1, 2, \ldots, \tag{6.27}$$

where γ_m winds once around the invariant tube at a fixed time t, selects those tubes that support a Floquet state. This naturally leads to a reordering of the Floquet states based on a new quantum number, corresponding to the number of quantized tubes residing within the resonance zone. The state corresponding to $m = 0$ then represents the innermost quantized tube and can therefore be regarded as a ground state. Likewise, the state with $m = 1$ is associated with the adjacent tube in the hierarchy established by Eq. (6.27), making it the first excited state, followed by subsequently ordered states. Essentially, the integer m in the quantization rule Eq. (6.27) directly aligns with the quantum number m used to label the Mathieu states.

Moreover, Eq. (6.27) suggests that each Floquet state occupies an area of 2π in the (k, x) phase-space plane at any given instant. As a result, the resonant zones observed in Fig. 6.1(c), when considered collectively, are expected to accommodate approximately 10 pairs of nearly degenerate Floquet states.

6.2.4 Visualizing the Floquet States in Real-Space

To support the above formulation, a similar line of reasoning can be presented in a purely quantum yet alternative manner. For this, we rely on a particular visualization of Floquet states which uses the Wannier basis. Intrinsically, Floquet states do not have a predefined ordering, however they can be labeled based on their energy expectation values averaged over one driving period. Although this requires computing the mean energy at every instant of time, a reasonable ordering can still be achieved by labeling the states according to instantaneous expectation values $\langle u_\ell(t_0)|\widehat{H}_0|u_\ell(t_0)\rangle$, where t_0 refers to the time at which the drive vanishes. While this ordering scheme is not perfect, it provides a meaningful order compared to an arbitrary ordering. The instantaneous ordering scheme is implemented as

$$\langle u_\ell(t_0)|\widehat{H}_0|u_\ell(t_0)\rangle \leq \langle u_{\ell+1}(t_0)|\widehat{H}_0|u_{\ell+1}(t_0)\rangle \tag{6.28}$$

for $\ell = 0, 1, 2, \ldots$. To visualize the Floquet states the tight-binding system provides distinct advantage of the representation in terms of the Wannier basis. Thus Floquet states can be expressed in the discretized real-space. In Fig. 6.3, we display the lowest 120 unperturbed states and Floquet states visualized in Wannier space. The unperturbed spectrum is once again presented for comparison. As described in Sec. 4.2, the unperturbed states correspond to the phase space of the undriven pendulum, i.e., Fig. 6.1(a). In this context, regular states are characterized

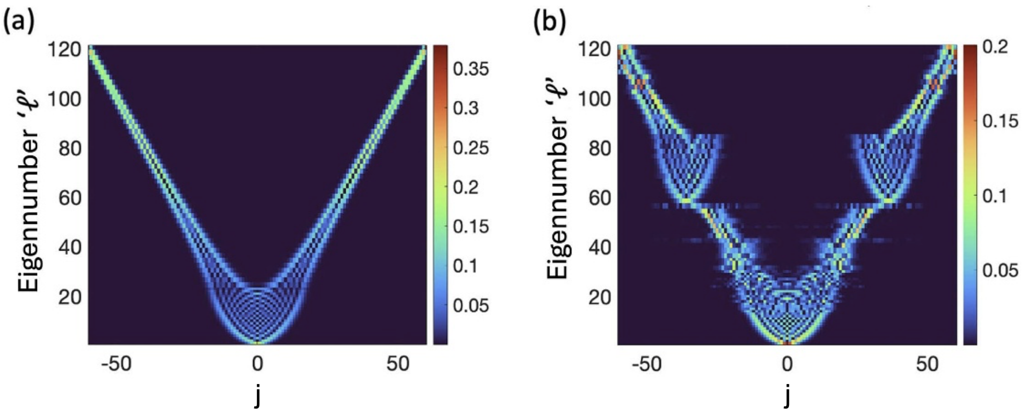

Figure 6.3: Unperturbed eigenstates of the parabolic optical lattice (a) and Floquet states in the presence of external driving (b), visualized in real-space through the Wannier basis. The parametric values remain the same as in Fig. 6.1. In addition, the unperturbed eigenstates correspond to Fig. 6.1(a), while the Floquet states connect with Fig. 6.1(c). The figure is taken from [90] with permission.

as harmonic oscillator-like at low energies and doubly-degenerate Wannier-Stark-like localized states at high energies, as shown in Fig. 6.3(a). Similarly, the lowest and highest Floquet states in Fig. 6.3(b) are also harmonic oscillator-like and Wannier-Stark-like localized states, appearing as remnants of the undriven system, though the Wannier-Stark-like Floquet states are significantly broadened. The states in the middle are much involved. In particular, the Floquet states near the critical index, where states change their nature in the undriven system, appear blurred, corresponding to the intricate region of classical motion depicted in Fig. 6.1(c). A closer look at the intermediate states reveals states corresponding to secondary resonances. However, the main highlight remains the ordered states centered around $j = \pm 35$, which correspond to the spatial locations where the center of the resonant island lies in Fig. 6.1(c). These states reflect the effect of resonance and confirm the predictions of the Mathieu approximation. Thus, the driven system provides a broad range of states that can be harnessed to achieve different dynamics.

6.2.5 Classical Characterization of Floquet States

To demonstrate the exact connection between the classical dynamics and the Floquet states we plot the phase-space distributions of these states. For this purpose, we again consider the Husimi representation Eq. (4.14). Fig. 6.4 displays the comparison between color-coded density plots of the Husimi Q-function for the Floquet states and the stroboscopic Poincaré phase space of the driven quantum pendulum. Evidently, the harmonic oscillator-like Floquet states are attached to the regular invariant tubes.

In Fig. 6.4(a) and (b) the ground state and the second excited state of the driven quantum pendulum are shown, which fall onto the elliptical curves in an orderly manner. Fig. 6.4(c) highlights a state that belongs to a chain of islands. This state presents a distinct feature, i.e.,

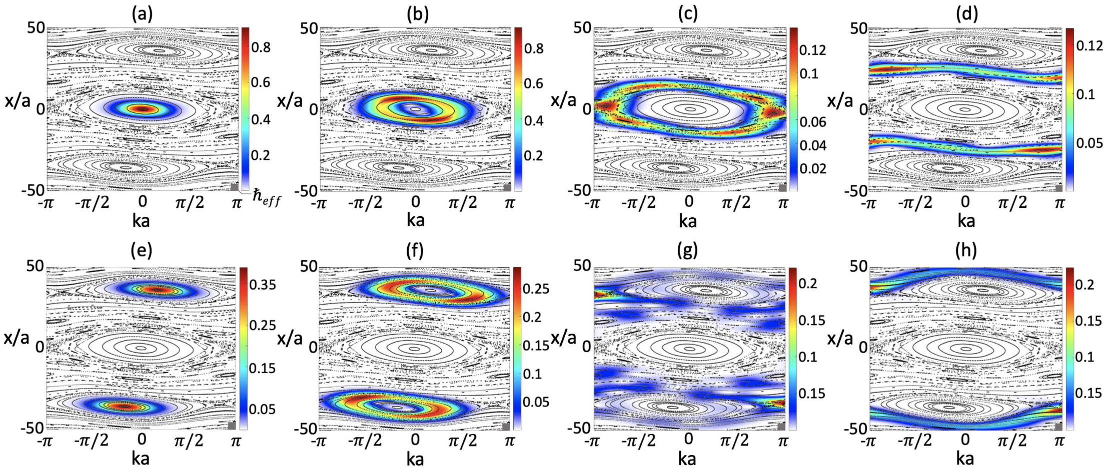

Figure 6.4: Color-coded Husimi distributions of the Floquet states labelled by the index $\ell = 0, 10, 15, 45, 58, 65, 85$, and 86, which are ordered using the instantaneous energy ordering scheme, ((a)-(h)) superimposed on the stroboscopic Poincaré map taken from Fig. 6.1(c). The figure is taken from [90] with permission.

it maintains coherence even though it evolves through the chaotic region. Fig. 6.4(d) shows a state that is linked to vibrational trajectories. This state exhibits a Bloch oscillations-like evolution, a signature of regular motion, suggesting a stable, periodic progression within the phase space. The Husimi-distriutions of the resonant Floquet states are shown in Fig. 6.4(e) and (f). In this case, the total density lies inside the resonance-induced regular islands. These states possess Floquet micro-motion similar to Bloch oscillations, on top of which harmonic oscillations are observed between the periods. Next, in Fig. 6.4(g), we see a chaotic state populating the stochastic region outside the resonant zone. This state reflects the chaotic dynamics induced by the resonance in the driven pendulum, further indicating the transition from regular to chaotic behavior. In (h), another vibrational state is shown, which, like the state in (d), follows Bloch-like evolution, signaling a regular, stable behavior in the system.

Therefore, the Floquet states can be broadly categorized as ‘regular’, ‘resonant-regular’, and ‘chaotic’. In the following we show that the different occupations of these states leads to different dynamics.

6.2.6 Floquet State Occupation Probabilities for Sudden Turn On

Typically the occupation probabilities of Floquet states do depend strongly on the drive turn on function $f(t)$. However, the Floquet states are associated with a strictly periodic driving and, as such, do not rely on the function $f(t)$. To investigate how the occupation probabilities change with the sudden activation of modulation with different phases, we disregard the actual switch-on process (6.13) and use $f(t) = 1$, which refers to strictly periodic driving and thus the Floquet description holds. As these states repeat themselves after a period, therefore they remain unaffected by the drive phase. Given an initial wave packet $|\Phi(0)\rangle$ at $t = 0$,

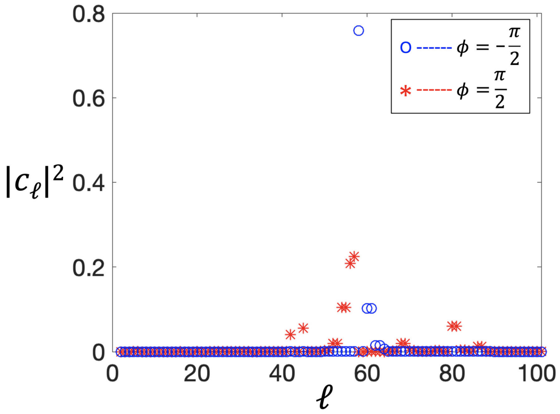

Figure 6.5: Floquet-state occupation probabilities $|c_\ell|^2$ obtained after a sudden turn-on of the trap modulation for initial Gaussian wave packets (3.32) with width $\sigma = 2.23$, centered at $j_0 = 35$, with $\phi = \pm\pi/2$. Once again, the parameters are fixed as in Fig. 6.1(c). The figure is taken from [90] with permission.

which is considered the moment of a sudden turn-on, the expansion coefficients are obtained by projecting this initial state onto the Floquet states, such that

$$c_\ell = \langle u_\ell(0)|\Phi(0)\rangle. \tag{6.29}$$

As Floquet states can be synchronized with the argument of the drive by writing $|\widetilde{u}_\ell(\omega t + \phi)\rangle$ instead of $|u_\ell(t)\rangle$, selecting different phases ϕ at $t = 0$ corresponds to sampling the Floquet states at various points in their evolution. As a result, the expansion coefficients, and consequently the occupation probabilities, depend on the drive phase ϕ [90].

We take an initial Gaussian state (3.32) as employed in previous chapters to demonstrate the wave packet dynamics. The parameters of the system and Gaussian state are kept the same to match the conditions in Sec. 5.2.1.

The occupation probabilities are shown in Fig. 6.5 for the initial Gaussian state with mean position $j_0 = 35$. This position corresponds to the resonance zone in Fig. 6.1(c). In this case, for $\phi = -\pi/2$, only a few Floquet states that correspond to the regular-resonant island are populated. A significant portion of the occupation is concentrated on the resonant ground state with $\ell = 58$. In contrast, for $\phi = \pi/2$, occupation is shared by many more states, particularly those associated with the hyperbolic fixed point of the resonant pendulum. The high density observed at the hyperbolic fixed point is attributed to the scarring effect, which can be perceived as the slowing down of the motion near the classical turning points of the pendulum.

To illustrate the resulting wave packet dynamics, we analyze the periodic evolution of the most significantly occupied Floquet states, as shown in Figs. 6.6 and 6.7. Additionally, we present the quasiperiodic solutions that emerge from the superposition of multiple Floquet states. In Figs. 6.6(a) and (b), we depict the absolute values of the one-period evolution for the Floquet states at indices $\ell = r = 58$ and $\ell = 60$, which exhibit the highest occupation in

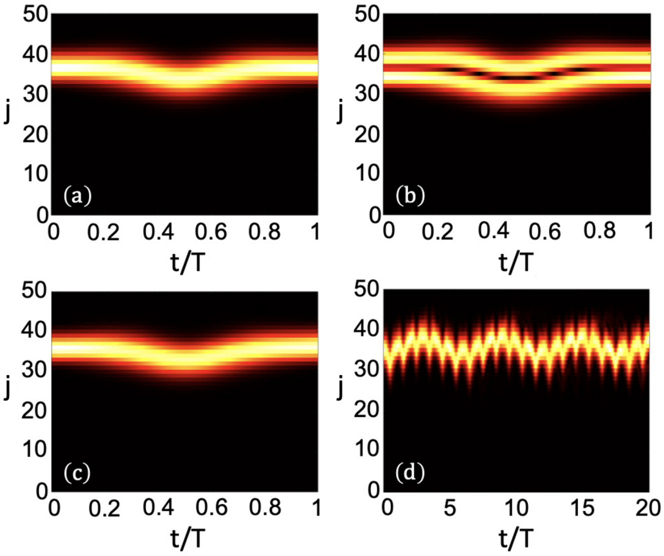

Figure 6.6: Absolute values of the one-period evolution of the maximally-occupied Floquet states corresponding to $\ell = r = 58$ in (a) and $\ell = 60$ in (b) for the case with $\phi = -\pi/2$. (c) One period evolution generated by the superposition of all the occupied Floquet states and (d) the corresponding long-time dynamics. The figure is taken from [90] with permission.

Fig. 6.5 for the case $\phi = -\pi/2$. These states belong to the Mathieu hierarchy, with Fig. 6.6(a) corresponding to the effective Floquet ground state ($m = 0$) and Fig. 6.6(b) representing the first excited state ($m = 1$). Their slow oscillatory motion within one driving period reflect Bloch-like dynamics along the arms of the parabolic lattice [79–81].

In contrast, Fig. 6.6(c) illustrates the one-period evolution generated by the Gaussian wave packet, comprising a superposition of all occupied Floquet states. Since the Floquet ground state dominates the occupation probability, the overall evolution closely resembles its dynamics. However, over extended timescales, small implicit variations accumulate, leading to observable net transport of the wave packet across the lattice, as demonstrated in Fig. 6.6(d). Because only a limited number of Floquet states within the $1:1$ resonant island contribute to the dynamics, the wave packet retains coherence, generating subharmonic motion with a period equivalent to the period of the regular island.

In Fig. 6.7(a)-(d), the absolute values of the one-period evolution for Floquet states with indices $\ell = 45$, 54, 57, and 81 are shown. These states carry a significant share of population, as shown in Fig. 6.5 for $\phi = -\pi/2$. These are the separatrix states located on the broken separatrix surrounding the regular resonant island on the positive axis. The state shown in Fig. 6.7(a) exhibits intricate, mixed dynamics. In contrast, Fig. 6.7(b) shows breathing motion along the separatrix. Like Fig. 6.7(a), the state in Fig. 6.7(c) also displays several modes, with complex dynamics. The phase space evolution of these two states is similar to Fig. 6.4(g), and therefore, these are considered chaotic states. Fig. 6.7(d) shows a highly excited state of the

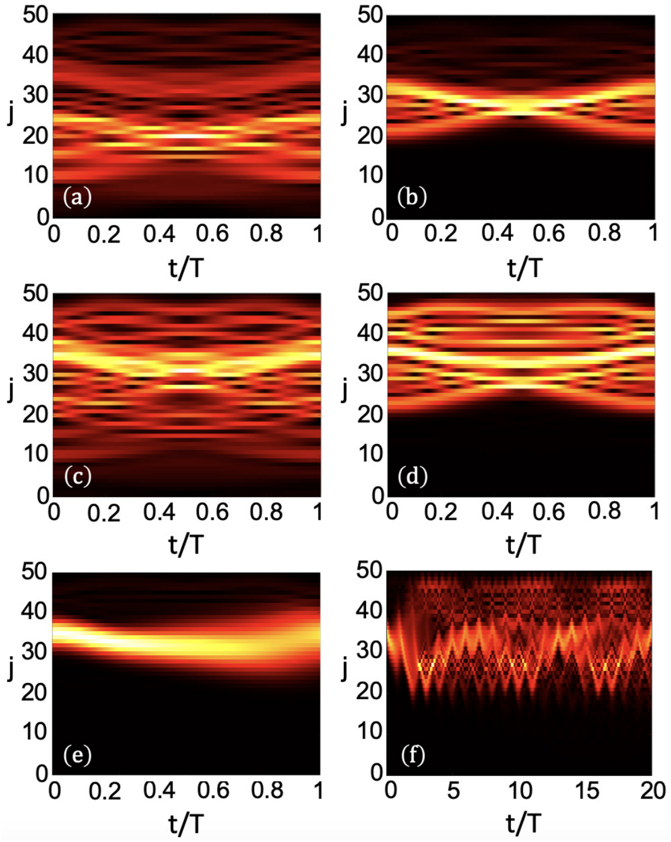

Figure 6.7: Absolute values of the one-period evolution of the maximally occupied Floquet states corresponding to $\ell = 45$ in (a), $\ell = 54$ in (b), $\ell = 57$ in (c) and $\ell = 81$ in (d), for the case with $\phi = \pi/2$. (e) One period evolution generated by the superposition of all occupied Floquet states and (f) the corresponding long-time dynamics. The figure is taken from [90] with permission.

resonance-induced pendulum, located near the separatrix.

Given the high population of separatrix states, we expect to see nonuniform spreading motion when all states are superimposed. This spreading motion is clearly visible in the propagated Gaussian wave packet in Fig. 6.7(e). The resulting quasiperiodic evolution leads to further spreading and recombinations, producing complex dynamics, as shown in Fig. 6.7(f). These dynamics are a combination of Bloch-breathing and -oscillatory modes, reflecting the persistent Bloch-like oscillatory behavior seen in the these examples [79]. However, the variation in the dynamics emerges from the diverse nature of the states triggered by the external periodic driving. Thus, by controlling the drive phase, one can tune the occupation of Floquet states thus giving rise to different dynamics.

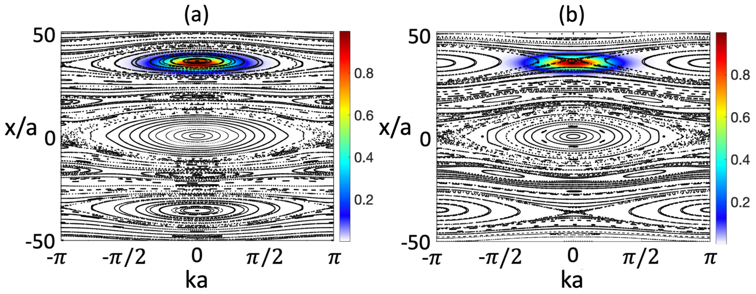

Figure 6.8: Color-coded Husimi distribution of the initial Gaussian state superimposed on the Poincaré sections traced under the opposite phase drive cases with $\phi = -\pi/2$ (a) and $\phi = \pi/2$ (b). All other parameters remain the same as in Fig. 6.1(c). The figure is taken from [90] with permission.

6.2.7 Role of Floquet States and the Poincaré Orbit Topology

A clear picture on the varying occupation probabilities of Floquet states can be obtained by analyzing the Poincaré surfaces of section traced at times corresponding to the driving phase. This is illustrated in Fig. 6.8, where the Poincaré phase space is plotted at $\omega t = \pm\pi/2$, revealing different positions for the regular resonant islands. The Poincaré sections are shown superposed on the Husimi distribution of the initial Gaussian state. In Fig. 6.8(a), for $\phi = -\pi/2$, the initial Gaussian wave packet intersects the regular resonant island, highlighting the occupation of near-resonant Floquet states. On the other hand, for $\phi = \pi/2$, Fig. 6.8(b) shows the emergence of separatrix states as the wave packet overlaps with the separatrix trajectory at the hyperbolic fixed point. These observations emphasize changing occupation probabilities with the drive phase

This also leads us to conclude that the quantum dynamics corresponding to a classical regular island differ significantly from those outside it. Moreover, these dynamics can be accessed by properly choosing the drive phase. The topology of classical Poincaré phase space provides a general overview of the dynamical regimes of the driven parabolic optical lattice. Besides the phase-dependent dynamics it also evince sub- or super-harmonic responses and chaotic dynamics. However, there exist collapse and revivals are fully quantum mechanical and that are beyond the classical description.

Summary and Outlook 7

In this thesis, we have explored the collective dynamics of ultracold atoms in a one-dimensional optical lattice subjected to both static and time-dependent external potentials.

In Chapter 3, we introduce (the reader to) Bloch oscillations, which play a central role in the various dynamical phenomena explored in this thesis. The Bloch oscillations phenomenon is known to demonstrate different manifestations of wave packet dynamics as the system conditions are changed. Time-periodic driving is a commonly used tool to modify the system's characteristics which introduces novel features that are unachievable in the undriven scenario. The time-periodic driving of an optical lattice with an external linear potential that vanishes at every drive period, generates a cycle average transport of a localized wave packet. This transport dies out completely at specific ratios of the driving amplitude and its frequency, a phenomenon known as dynamical localization. These dynamics are described using the dispersion relation for the driven system and the tight-binding group velocity averaged over one period. We describe the emergence of these dynamics on top of Bloch oscillations when the oscillating linear potential retains a static component, even at vanishing drive strengths, which is resonant with the drive. Thus, we demonstrate super-Bloch oscillations, which arise as a result of the interplay between the static and driven components of the potential, leading to an amplified oscillatory motion of the wave packet.

Bloch dynamics are characterized by spatially-periodic potentials and spatially-constant forces. However, systems exist where these conditions are nullified or are asymptotically modified. We consider the latter and explore how changed a spatial-inhomogeneity modifies Bloch oscillations or even super-Bloch oscillations. In this pursuit, in Chapter 4, we first consider disordered lattices, where a quasi-disorder is seen to bring about collapse and revivals of Bloch oscillations. Further, localized disorder at distinct lattice sites acts as a scatterer, disrupting the amplitude of the wave packet and leading to a progressive loss of density. Besides this, a global inhomogeneity is explored, which uses a global parabolic trap over the periodic optical lattice. The parabolic potential provides a space-dependent force, although for weakly curved traps, the force can be considered as constant in a restricted region of space. This furnishes dynamics very similar to Bloch oscillations, although the evolving wave packet dephase due to anharmonicity of the spectrum. The dephasing engenders collapse and revival dynamics. In this regime, Wannier-Stark-like states emerge which due to the trap symmetry appears in pairs localized on opposite sides of the parabolic lattice. These states intrinsically carry a minuscule energy mismatch, which permits tunneling to the other arm at exceedingly large time scales. We show that the system augmented by a quasi-disorder, induced by an additional weak incommensurate potential, provides a unique control over the tunneling time. That is by carefully choosing the incommensurate potential one engineers a tunable energy-mismatch between the states while preserving the two-fold degeneracy. In this manner, Bloch oscillations-like dynamics manifest a beating motion between the opposite ends of the parabolic lattice. This kind of barrier free wave packet connection is known as dynamical tunneling, which in the present set up holds significant promise for the realization of long-range macroscopic tunneling. We also found that, while Bloch-like oscillations in the parabolic lattice stabilize with the inclusion of weak atom-atom interactions, the tunneling dynamics in the bichromatic parabolic lattice are counteracted. Nonetheless, a dominant disorder with large energy mismatch reactivates the tunneling dynamics where the tunneling follows an unusual pattern in time. Accordingly, the interacting system is worthy of further attention. Hence, while the spatially-inhomogeneous system is expected to destroy the coherent Bloch motion. The present analysis suggests that it also adds additional features and novel manifestations of these dynamics.

Next, as Bloch oscillations are seen to emerge in the parabolic lattice, a straightforward extension would be to investigate these in the presence of external time-periodic driving. This we address in Chapter 5. Keeping in view, the near-resonance condition for super-Bloch oscillation, we employ the resonantly drive the Bloch-like oscillations with a time-periodically modulated parabolic trap. Our studies reveal that this brings about dynamics similar to Bloch oscillations, although here important differences exist. In the driven parabolic lattice, the strongly amplified transport is generated due to a coupling between the mean position and the mean quasimomentum of the evolving wave packet, which manifest as parametrically oscillating Bloch frequency. This is inferred by a modified acceleration theorem which predicts a relative phase even in the absence of an external detuning. It furnishes a non-constant, yet oscillatory, phase factor between the modulation and the Bloch oscillations with which the modulation interacts with Bloch oscillations at only a partial region of the Brillouin zone. Thus, this phase is similar yet different from the constant relative phase of the super-Bloch oscillations, with which the modulation explores quasimomentum values across the entire Brillioun zone and thus a large transport is generated. However, this comes at a cost, that is with super-Bloch oscillations a constant detuning always furnishes an inversely proportional amplitude. However, with the oscillations in the parabolic system, these we call chirped Bloch-harmonic transport (CBHT), the direct relation breaks down, as the amplitude and frequency is determined by the coupling. Thus, CBHT can be utilized to generate comparatively small amplitude oscillations at smaller effective frequencies. Further, we note that the relative phase appears confined to different regions of the Brillouin zone if the drive phase is varied. For an opposite parity drive, this leads to significantly contrasting dynamics which for one phase are fully coherent and are totally delocalized at other. Thus we note that the dynamics change with the phase of the drive, which is again in contrast with super-Bloch oscillations. Furthermore, different regions of the parabolic lattice exhibit varying strengths of lattice anharmonicity and coupling between position and quasimomentum; thus, the dynamics change depending on the initially choosen wave packet and system conditions . Hence, driven parabolic optical lattices presents rich dynamics, which can be accessed by suitably choosing the initial conditions.

The coupling between the coordinate position and the quasimomentum can be deduced in a classical manner through the phase space. Thus, we note that the classical dynamics of the system provides important information about the system's dynamics. At a nonlinear resonance regions of periodic dynamics appear in the stroboscopically determined phase space of the driven system. Related to these regular regions exist harmonic oscillator-like states which are covered by a Mathieu equation in a purely quantum mechanical manner. For a proper comparison of the quantum dynamics to the classical ones, we consider the Floquet formalism under which the periodically driven system can be effectively described by Floquet states which repeat over a period. As the Floquet picture applies to systems with a strictly periodic drive, therefore we assume an instantaneous turn on of the drive with different phases and analyze the Floquet spectrum. The analysis shows that the Floquet states can be categorized by comparing their dynamics to the classical dynamics of the system. Given the different nature of the observed Floquet states, the dynamics of an initial wave packet vary depending on the changing occupation probabilities of these states. Coherent dynamics appears for the population of states belonging to the regular regions in phase space, while wave packet spreading occurs for states lying in a chaotic region. We demonstrate that the occupation probabilities change if the initial phase of the drive is varied or parameters of the wave packet are changed. Thus, Floquet theory provides important information about the wave packet dynamics in the driven parabolic lattice, where a general overview of the dynamics can be obtained from the classical dynamics of the system. These results are described in Chapter 6.

The ability to engineer spatially-inhomogeneous periodic potentials in cold atom optical lattice systems presents exciting opportunities to explore novel quantum transport phenomena. The interplay between decay, revivals, and tunneling dynamics in such systems offers a rich landscape for investigating quantum coherence, long-range tunneling, and macroscopic quantum effects. The enhancement of tunneling splitting through bichromatic lattices, while preserving state degeneracy, opens pathways for controlled manipulation of quantum states.

Looking ahead, this exploration may lay the ground for interesting and challenging future work, concerning, e.g., the inclusion of time-periodic driving to study the dynamical tunneling between distant regular islands in a partly chaotic phase space, or the investigation of ramifications of many-body interactions.

Exploring the impact of resonant driving on Bloch-like oscillations in spatially inhomogeneous lattices with parabolic traps may further refine our understanding of quantum transport and spreading dynamics. This also offer a new paradigm for lattice dynamics not accessible in traditional solid-state systems, but open to experimental verification with ultracold atom experiments.

Additionally, the Floquet framework serves as a powerful tool for explaining phase-dependent dynamics and understanding long-time evolution in driven systems. Investigations into nonlinear Floquet states and their connections to time crystals remain largely unexplored and could reveal new regimes of quantum behavior. The connection between classical and quantum dynamics in driven optical lattices also offers a compelling avenue for studying quantum-classical correspondence.

Overall, these findings lay the groundwork for further experimental and theoretical developments, opening new possibilities for exploring quantum coherence, control, and transport in driven optical lattices and beyond.

Bibliography

---

[1] A. Einstein, Quantentheorie des einatomigen idealen Gases, Sitzung der physikalisch-mathematischen Klasse, 3 (1925).

[2] S. N. Bose, Plancks Gesetz und Lichtquantenhypothese, Z. Phys. **26**, 178 (1924).

[3] J. C. Maxwell, On physical lines of force, Phil. Mag. **4**, 23 (1861).

[4] P. N. Lebedev, Experimental examination of light pressure, Ann. d. Phys. (Leipzig) **6**, 433 (1901).

[5] E. F. Nicols and G. F. Hull, The pressure due to radiation, Phys. Rev. **17**, 26 (1903).

[6] P. N. Lebedev, The pressure of light on gases. An experimental study for the theory of comet's tails, Ann. d. Phys. (Leipzig) **32**, 411 (1910).

[7] P. L. Kapitza and P. A. M. Dirac, The reflection of electrons from standing light waves, Proc. Cambridge Phil. Soc. **29**, 297 (1933).

[8] O. R. Frisch, Experimenteller Nachweis des Einsteinschen Strahlungsrückstosses, Z. Phys. **86**, 42 (1933).

[9] A. Einstein, Zur Quantentheorie der Strahlung, Phys. Z. **18**, 121 (1917).

[10] F. Saif and S. Watanabe, *Optical Forces on Atoms* (IOP Publishing, Bristol, 2023).

[11] A. Ashkin, Acceleration and trapping of particles by radiation pressure, Phys. Rev. Lett. **24**, 156 (1970).

[12] T. W. Hänsch and A. L. Schawlow, Cooling of gases by laser radiation, Opt. Commun. **13**, 68 (1975).

[13] D. J. Wineland and H. Dehmelt, Proposed $10^{14}\Delta\nu < \nu$ laser fluorescence spectroscopy on TI^+ mono-ion oscillator, Bull. Am. Phys. Soc. **20**, 637 (1975).

[14] C. J. Foot, Laser cooling and trapping of atoms, Contemp. Phys. **32**, 369 (1991).

[15] M. H. Anderson, J. R. Ensher, M. R. Matthews, C. E. Wieman, and E. A. Cornell, Observation of Bose-Einstein condensation in a dilute atomic vapors, Science **269**, 198 (1995).

[16] K. B. Davis, M. O. Mewes, M. R. Andrews, N. J. van Druten, D. S. Durfee, D. M. Kurn, and W. Ketterle, Bose-Einstein condensation in a gas of sodium atoms, Phys. Rev. Lett. **75**, 3969 (1995).

[17] C. C. Bradley, C. A. Sackett, J. J. Tollet, and R. Hulet, Bose-Einstein condensation of Lithium: Observation of limited condensate number, Phys. Rev. Lett. **78**, 985 (1997).

[18] F. London, On the Bose-Einstein condensation, Phys. Rev. **54**, 947 (1938).

[19] E. P. Gross, Structure of a quantized vortex in Boson systems, Nuovo Cim. **20**, 454 (1961).

[20] L. P. Pitaevskii, Vortex Lines in an imperfect Bose gas, J. Exptl. Theoret. Phys. (U.S.S.R.) **13**, 451 (1961).

[21] N. N. Bogoliubov, On the theory of superfluidity, J. Phys. (U.S.S.R) **11**, 23 (1947).

[22] S. M. Inouye, M. R. Andrews, J. Stenger, H.-J. Miesner, D. M. Stamper-Kurn, and W. Ketterle, Observation of Feshbach resonances in a Bose-Einstein condensate, Nature **392**, 151 (1998).

[23] P. R. Courteille, R. S. Freeland, D. Heinzen, F. van Abeelen, and B. Verhaar, Observation of a Feshbach resonance in cold atom scattering, Phys. Rev. Lett. **81**, 69 (1998).

[24] M. Theis, G. Thalhammer, K. Winkler, M. Hellwig, G. Ruff, R. Grimm, and J. H. Denschlag, Tuning the scattering length with an optically induced Feshbach resonance, Phys. Rev. Lett. **93**, 123001 (2004).

[25] C. Chin, R. Grimm, P. Julienne, and E. Tiesinga, Feshbach resonances in ultracold gases, Rev. Mod. Phys. **82**, 1225 (2010).

[26] M. Greiner, O. Mandel, T. Esslinger, T. W. Hänsch, and I. Bloch, Quantum phase transition from a superfluid to a Mott insulator in a gas of ultracold atoms, Nature **415**, 39 (2002).

[27] J. Struck, C. Ölschläger, R. L. Targat, P. Soltan-Panahi, A. Eckardt, M. Lewenstein, P. Windpassinger, and K. Sengstock, Quantum simulation of frustrated magnetism in triangular optical lattices, Science **425**, 996 (2011).

[28] P. Soltan-Panahi, J. Struck, P. Hauke, A. Bick, W. Plenkers, G. Meineke, C. Becker, P. Windpassinger, M. Lewenstein, and K. Sengstock, Multi-component quantum gases in spin-dependent hexagonal lattices, Nature Phys. **7**, 434 (2011).

[29] G.-B. Jo, J. Guzman, C. Thomas, P. Hosur, A. Vishwanath, and D. Stamper-Kurn, Ultracold atoms in a tunable optical Kagome lattice, Phys. Rev. Lett. **108**, 045305 (2012).

[30] J. Brachmann, W. Bakr, J. Gillen, A. Peng, and M. Greiner, Inducing vortices in a Bose-Einstein condensate using holographically produced light beams, Opt. Express **19**, 12984 (2011).

[31] Y. Takahashi, Quantum simulation of quantum many-body systems with ultracold two-electron atoms in an optical lattice, Proc. Jpn. Acad. Ser. B **98**, 141 (2022).

[32] J. Hubbard, Electron correlations in narrow energy bands, Proc. R. Soc. Lond. A **276**, 238 (1963).

[33] M. P. A. Fisher, P. B. Weichman, G. Grinstein, and D. S. Fisher, Boson localization and the superfluid-insulator transition, Phys. Rev. B **40**, 546 (1989).

[34] O. Morsch, J. H. Müller, M. Cristiani, D. Ciampini, and E. Arimondo, Bloch oscillations and mean-field effects of Bose-Einstein condensates in 1D optical lattices, Phys. Rev. Lett. **87**, 140402 (2001).

[35] Y.-J. Lin, R. L. Compton, K. J. Garcia, J. V. Porto, and I. B. Spielman, Synthetic magnetic fields for ultracold neutral atoms, Nature **462**, 628 (2009).

[36] M. Aidelsburger, M. Atala, M. Lohse, J. T. Barreiro, B. Paredes, and I. Bloch, Realization of the Hofstadter Hamiltonian with ultracold atoms in optical lattices, Phys. Rev. Lett. **111**, 185301 (2013).

[37] G. Jotzu, M. Messer, R. Desbuquois, M. Lebrat, T. Uehlinger, D. Greif, and T. Esslinger, Experimental realisation of the topological Haldane mode, Nature **515**, 216 (2014).

[38] O. Mandel, M. Greiner, A. Widera, T. Rom, T. W. Hänsch, and I. Bloch, Coherent transport of neutral atoms in spin-dependent optical lattice potentials, Phys. Rev. Lett. **91**, 010407 (2003).

[39] M. Endres, H. Bernien, A. Keesling, H. Levine, E. R. Anschuetz, A. Krajenbrink, C. Senko, V. Vuletic, M. Greiner, and M. D. Lukin, Atom-by-atom assembly of defect-free one-dimensional cold atom array, Science **354**, 1024 (2016).

[40] D. Barredo, V. Lienhard, S. de Léséleuc, T. Lahaye, and A. Browaeys, Synthetic three-dimensional atomic structures assembled atom by atom, Nature **561**, 79 (2018).

[41] W. S. Bakr, J. I. Gillen, A. Peng, S. Fölling, and M. Greiner, A quantum gas microscope for detecting single atoms in a Hubbard-regime optical lattice, Nature **462**, 74 (2009).

[42] J. F. Sherson, C. Weitenberg, M. Endres, M. Cheneau, I. Bloch, and S. Kuhr, Single-atom-resolved fluorescence imaging of an atomic Mott insulator, Nature **467**, 68 (2010).

[43] N. Poli, F.-Y. Wang, M. G. Tarallo, A. Alberti, M. Prevedelli, and G. M. Tino, Precision measurement of gravity with cold atoms in an optical lattice and comparison with a classical gravimeter, Phys. Rev. Lett. **106**, 038501 (2011).

[44] R. Bouchendira, P. Cladé, S. Guelatti-Khélifa, F. Nez, and F. Biraben, Precision determination of the fine structure constant from atomic recoil, Frontiers in Optics 2012/Laser Science XXVIII , LW2I.3 (2012).

[45] M. Takamoto, F.-L. Hong, R. Higashi, and H. Katori, An optical lattice clock, Nature **435**, 321 (2005).

[46] A. M. Rey, Ultra-cold bosonic atoms in optical lattices: An overview, Rev. Acad. Colomb. Cienc. Ex. Fis. Nat. **45**, 666 (2021).

[47] M. Jan, Anderson localization in low-dimensional optical lattices, PhD thesis, Jagiellonian University, 2023.

[48] R. Gati, A bosonic Josephson junction, J. Phys. B **40**, 10 (2007).

[49] R. N. Palmer, A. Klein, and D. Jaksch, Optical lattice quantum Hall effect, Phys. Rev. A **78**, 013609 (2008).

[50] H. Habibian, A. Winter, S. Paganelli, H. Rieger, and G. Morigi, Bose-glass phases of ultracold atoms due to cavity backaction, Phys. Rev. Lett. **110**, 075304 (2013).

[51] M. Tarnowski, F. N. Ünal, N. Fläschner, B. S. Rem, A. Eckardt, K. Sengstock, and C. Weitenberg, Measuring topology from dynamics by obtaining the Chern number from a linking number, Nat. Commun. **10**, 1728 (2019).

[52] A. Zenesini, H. Lignier, D. Ciampini, O. Morsch, and E. Arimondo, Coherent control of dressed matter waves, Phys. Rev. Lett. **102**, 100403 (2009).

[53] A. Eckardt, M. Holthaus, H. Lignier, A. Zenesini, D. Ciampini, O. Morsch, and E. Arimondo, Exploring dynamic localization with a Bose-Einstein condensate, Phys. Rev. A **79**, 013611 (2009).

[54] M. Martinez, O. Giraud, D. Ullmo, J. Billy, D. Guéry-Odelin, B. Georgeot, and G. Lemarié, Chaos-assisted long-range tunneling for quantum simulation, Phys. Rev. Lett. **126**, 174102 (2021).

[55] E. Haller, R. Hart, M. J. Mark, J. G. Danzl, L. Reichsöllner, and H.-C. Nägerl, Inducing transport in a dissipation-free lattice with Super Bloch oscillations, Phys. Rev. Lett. **104**, 200403 (2010).

[56] M. Arnal, G. Chatelain, M. Martinez, N. Dupont, O. Giraud, D. Ullmo, B. Georgeot, G. Lemarié, J. Billy, and D. Guéry-Odelin, Chaos-assisted tunneling resonances in a synthetic Floquet superlattice, Sci. Adv. **6**, eabc4886 (2020).

[57] N. Dupont, L. Gabardos, F. Arrouas, N. Ombredane, J. Billy, B. Peaudecerf, and D. Guéry-Odelin, Hamiltonian ratchet for matter-wave transport, Phys. Rev. Lett. **131**, 133401 (2023).

[58] N. Dupont, G. Chatelain, L. Gabardos, M. Arnal, J. Billy, B. Peaudecerf, D. Sugny, and D. Guéry-Odelin, Quantum state control of a Bose-Einstein condensate in an optical lattice, PRX Quantum **2**, 040303 (2021).

[59] Y. Ke, S. Hu, B. Zhu, J. Gong, Y. Kivshar, and C. Lee, Topological pumping assisted by Bloch oscillations, Phys. Rev. Res. **2**, 033143 (2020).

[60] W. Liu, S. Hu, L. Zhang, Y. Ke, and C. Lee, Correlated topological pumping of interacting bosons assisted by Bloch oscillations, Phys. Rev. Res. **5**, 013020 (2023).

[61] F. Bloch, Über die Quantenmechanik der Elektronen in Kristallgittern, Z. Phys. **52**, 555 (1929).

[62] C. Zener, Non-adiabatic crossing of energy levels, Proc. R. Soc. A **137**, 696 (1932).

[63] C. Zener, A theory of the electrical breakdown of solid dielectrics, Proc. R. Soc. Lond. A **145**, 523 (1934).

[64] G. H. Wannier, Wave functions and effective Hamiltonian for Bloch electrons in an electric field, Phys. Rev. **117**, 432 (1960).

[65] T. Hartmann, F. Keck, H. J. Korsch, and S. Mossmann, Dynamics of Bloch oscillations, New J. Phys. **6**, 2 (2004).

[66] M. Glück, A. R. Kolovsky, and H. J. Korsch, Wannier–Stark resonances in optical and semiconductor superlattices, Phys. Rep. **366**, 103 (2002).

[67] J. Feldmann, K. Leo, J. Shah, D. A. B. Miller, J. E. Cunningham, T. Meier, G. von Plessen, A. Schulze, P. Thomas, and S. Schmitt-Rink, Optical investigation of Bloch oscillations in a semiconductor superlattice, Phys. Rev. B **46**, 7252(R) (1992).

[68] M. B. Dahan, E. Peik, J. Reichel, Y. Castin, and C. Salomon, Bloch oscillations of atoms in an optical potential, Phys. Rev. Lett. **76**, 4508 (1996).

[69] U. Peschel, T. Pertsch, and F. Lederer, Optical Bloch oscillations in waveguide arrays, Opt. Lett. **23**, 1701 (1998).

[70] V. Grecchi and A. Sacchetti, Acceleration theorem for Bloch oscillators, Phys. Rev. B **63**, 212303 (2001).

[71] F. Dreisow, G. Wang, M. Heinrich, R. Keil, A. Tünnermann, S. Nolte, and A. Szameit, Observation of anharmonic Bloch oscillations, Opt. Lett. **36**, 3963 (2011).

[72] A. R. Kolovsky and H. J. Korsch, Dynamics of interacting atoms in driven tilted optical lattices, J. Sib. Fed. Univ. Math. Phys. **3**, 311 (2010).

[73] K. Kudo and T. S. Monteiro, Theoretical analysis of super-Bloch oscillations, Phys. Rev. A **83**, 053627 (2011).

[74] S. Arlinghaus and M. Holthaus, Generalized acceleration theorem for spatiotemporal Bloch waves, Phys. Rev. B **84**, 054301 (2011).

[75] E. Díaz, A. García Mena, K. Asakura, and C. Gaul, Super-Bloch oscillations with modulated interaction, Phys. Rev. A **87**, 015601 (2013).

[76] X. Hu, S. Wang, C. Qin, C. Liu, L. Zhao, Y. Li, H. Ye, W. Liu, S. Longhi, P. Lu, and B. Wang, Observing the collapse of super-Bloch oscillations in strong-driving photonic temporal lattices, Adv. Photonics **6**, 046001 (2024).

[77] Z. A. Geiger, K. M. Fujiwara, K. Singh, R. Senaratne, S. V. Rajagopal, M. Lipatov, T. Shimasaki, R. Driben, V. V. Konotop, T. Meier, and D. M. Weld, Observation and uses of position-space Bloch oscillations in an ultracold gas, Phys. Rev. Lett. **120**, 213201 (2018).

[78] Q.-R. Zhu, S.-L. Chen, S.-J. Li, X.-T. Fang, L. Cao, and Z.-K. Hu, Generalized Bloch oscillations of ultracold lattice atoms subject to higher-order gradients, Phys. Rev. A **100**, 053603 (2019).

[79] U. Ali, M. Holthaus, and T. Meier, Chirped Bloch-harmonic oscillations in a parametrically forced optical lattice, Phys. Rev. Res. **5**, 043152 (2023).

[80] A. V. Ponomarev and A. R. Kolovsky, Dipole and Bloch oscillations of cold atoms in a parabolic lattice, Laser Phys. **16**, 367 (2005).

[81] J. Brand and A. R. Kolovsky, Emergence of superfluid transport in a dynamical system of ultra-cold atoms, Eur. Phys. J. D **41**, 331 (2007).

[82] J. F. Sherson, S. J. Park, P. L. Pedersen, N. Winter, M. Gajdacz, S. Mai, and J. Arlt, The pump–probe coupling of matter wave packets to remote lattice states, New Journal of Physics **14**, 083013 (2012).

[83] P. L. Pedersen, M. Gajdacz, N. Winter, A. J. Hilliard, J. F. Sherson, and J. Arlt, Production and manipulation of wave packets from ultracold atoms in an optical lattice, Phys. Rev. A **88**, 023620 (2013).

[84] T. Yamakoshi and S. Watanabe, Wave-packet dynamics of noninteracting ultracold Bosons in an amplitude-modulated parabolic optical lattice, Phys. Rev. A **91**, 063614 (2015).

[85] J. Heinze, J. S. Krauser, N. Fläschne, B. Hundt, S. Götze, A. P. Itin, L. Mathey, K. Sengstock, and C. Becker, Intrinsic photoconductivity of ultracold Fermions in optical lattices, Phys. Rev. Lett. **110**, 085302 (2013).

[86] T. Yamakoshi, S. Watanabe, S. Ohgoda, and A. P. Itin, Dynamics of Fermions in an amplitude-modulated lattice, Phys. Rev. A **93**, 063637 (2016).

[87] K. M. Fujiwara, K. Singh, Z. Geiger, R. Senaratne, S. V. Rajagopal, M. Lipatov, and D. M. Weld, Transport in Floquet-Bloch bands, Phys. Rev. Lett. **122**, 010402 (2019).

[88] A. Cao, R. Sajjad, E. Q. Simmons, C. J. Fujiwara, T. Shimasaki, and D. M. Weld, Transport controlled by Poincaré orbit topology in a driven inhomogeneous lattice gas, Phys. Rev. Res. **2**, 032032(R) (2020).

[89] U. Ali, M. Holthaus, and T. Meier, Wave packet dynamics in parabolic optical lattices: From Bloch oscillations to long-range dynamical tunneling, Phys. Rev. Res. **7**, 013141 (2025).

[90] U. Ali, M. Holthaus, and T. Meier, Floquet dynamics of ultracold atoms in optical lattices with a parametrically modulated trapping potential, New J. Phys. **26**, 123016 (2024).

[91] V. Letokhov and V. Minogin, Quantum motions of ultracooled atoms in resonant laser field, Phys. Lett. A **61**, 370 (1977).

[92] R. Loudon, *The Quantum Theory of Light*, 2nd ed. (Oxford University Press, Oxford, 1983).

[93] R. Graham, M. Schlautmann, and P. Zoller, Dynamical localization of atomic-beam deflection by a modulated standing light wave, Phys. Rev. A **45**, R19 (1992).

[94] O. Morsch and M. Oberthaler, Dynamics of Bose-Einstein condensates in optical lattices, Rev. Mod. Phys. **78**, 179 (2006).

[95] N. Ashcroft and N. Mermin, *Solid State Physics* (Harcourt, Fort Worth, 1976), https://onlinelibrary.wiley.com/doi/pdf/10.1002/piuz.19780090109.

[96] C. Kittel, *Introduction to Solid State Physics* (Wiley, New York, 2005).

[97] M. Abramowitz and I. A. Stegun, *Handbook of Mathematical Functions* (Dover Publications Inc., New York, 1972).

[98] B. J. Dąbrowska-Wüster, E. A. Ostrovskaya, T. J. Alexander, and Y. S. Kivshar, Multi-component gap solitons in spinor Bose-Einstein condensates, Phys. Rev. A **75**, 023617 (2007).

[99] W. Kohn, Analytic properties of Bloch waves and Wannier functions, Phys. Rev. **115**, 809 (1959).

[100] C. Salomon, G. V. Shlyapnikov, and L. F. Cugliandolo, *Many-Body Physics with Ultracold Gases: Lecture Notes of the Les Houches Summer School: Volume 94, July 2010, Lecture Notes of the Les Houches Summer School* Vol. 94 (OUP, Oxford, 2013).

[101] W. Zwerger, Mott–Hubbard transition of cold atoms in optical lattices, J. Opt. B: Quantum Semiclass. Opt. **5**, S9 (2003).

[102] I. Bloch, J. Dalibard, and W. Zwerger, Many-body physics with ultracold gases, Rev. Mod. Phys. **80**, 885 (2008).

[103] M. Ayub, K. Naseer, M. Ali, and F. Saif, Atom optics quantum pendulum, J. Russ. Laser Res. **30**, 205 (2009).

[104] J. Heinze, S. Götze, J. S. Krauser, B. Hundt, N. Fläschner, D.-S. Lühmann, C. Becker, and K. Sengstock, Multiband spectroscopy of ultracold Fermions: Observation of reduced tunneling in attractive Bose-Fermi mixtures, Phys. Rev. Lett. **107**, 135303 (2011).

[105] J. K. Freericks and H. Monien, Strong-coupling expansions for the pure and disordered Bose-Hubbard model, Phys. Rev. B **53**, 2691 (1996).

[106] G. G. Batrouni, V. Rousseau, R. T. Scalettar, M. Rigol, A. Muramatsu, P. J. H. Denteneer, and M. Troyer, Mott domains of Bosons confined on optical lattices, Phys. Rev. Lett. **89**, 117203 (2002).

[107] D. A. Hryniuk and M. H. Szymańska, Tensor-network-based variational Monte Carlo approach to the non-equilibrium steady state of open quantum systems, Quantum **8**, 1475 (2024).

[108] H. Saito, Solving the Bose-Hubbard model with machine learning, J. Phys. Soc. Jpn. **86**, 093001 (2017).

[109] R. Micnas and S. Robaszkiewicz, Superconductivity in systems with local attractive interactions, Condens. Matter Phys. **1**, 89 (1998).

[110] C. Lagoin, U. Bhattacharya, T. Grass, R. W. Chhajlany, T. Salamon, K. Baldwin, L. Pfeiffer, M. Lewenstein, M. Holzmann, and F. Dubin, Extended Bose-Hubbard model with dipolar excitons, Nature **609**, 485 (2022).

[111] N. Götting, F. Lohof, and C. Gies, Moiré-Bose-Hubbard model for interlayer excitons in twisted transition metal dichalcogenide heterostructures, Phys. Rev. B **105**, 165419 (2022).

[112] R. Fazio and H. van der Zant, Quantum phase transitions and vortex dynamics in superconducting networks, Phys. Rep. **355**, 235 (2001).

[113] O. A. Prośniak, M. Łącki, and B. Damski, Critical points of the three-dimensional Bose-Hubbard model from on-site atom number fluctuations, Sci. Rep. **9**, 8687 (2019).

[114] A. D. Greentree, C. Tahan, J. H. Cole, and L. C. L. Hollenberg, Quantum phase transitions of light, Nature Phys. **2**, 856 (2006).

[115] D. Jaksch, C. Bruder, J. I. Cirac, C. W. Gardiner, and P. Zoller, Cold Bosonic atoms in optical lattices, Phys. Rev. Lett. **81**, 3108 (1998).

[116] M. Holthaus, Bloch oscillations and Zener breakdown in an optical lattice, J. Opt. B: Quantum Semiclass. Opt. **2**, 589 (2000).

[117] H. Jones and C. Zener, The general proof of certain fundamental equations in the theory of metallic conduction, Proc. R. Soc. Lond. A **144**, 101 (1934).

[118] J. B. Krieger and G. J. Iafrate, Time evolution of Bloch electrons in a homogeneous electric field, Phys. Rev. B **33**, 5494 (1986).

[119] A. M. Bouchard and M. Luban, Bloch oscillations and other dynamical phenomena of electrons in semiconductor superlattices, Phys. Rev. B **52**, 5105 (1995).

[120] D. Witthaut, M. Werder, S. Mossmann, and H. J. Korsch, Bloch oscillations of Bose-Einstein condensates: Breakdown and revival, Phys. Rev. E **71**, 036625 (2005).

[121] M. Holthaus, Floquet engineering with quasienergy bands of periodically driven optical lattices, J. Phys. B: At. Mol. Opt. Phys. **49**, 013001 (2016).

[122] S. Walter, The influence of disorder on Bloch oscillations in a system of ultracold atoms in an optical lattice, PhD thesis, Stony Brook University, 2009.

[123] L. Duan, Periodic jumps in binary lattices with a static force, Phys. Rev. B **108**, 174306 (2023).

[124] S. Walter, D. Schneble, and A. C. Durst, Bloch oscillations in lattice potentials with controlled aperiodicity, Phys. Rev. A **81**, 033623 (2010).

[125] G. Torres-Vega, J. D. Morales-Guzmán, and A. Zúñiga-Segundo, Special functions in phase space: Mathieu functions, J. Phys. A Math. Gen. **31**, 6725 (1998).

[126] C. Hooley and J. Quintanilla, Single-atom density of states of an optical lattice, Phys. Rev. Lett. **93**, 080404 (2004).

[127] A. M. Rey, G. Pupillo, C. W. Clark, and C. J. Williams, Ultracold atoms confined in an optical lattice plus parabolic potential: A closed-form approach, Phys. Rev. A **72**, 033616 (2005).

[128] D. McKay, M. White, and B. DeMarco, Lattice thermodynamics for ultracold atoms, Phys. Rev. A **79**, 063605 (2009).

[129] A. Ponomarev, Dynamics of cold Fermi atoms in one-dimensional optical lattices, PhD thesis, University of Freiburg, 2008.

[130] K. Husimi, Some formal properties of the density matrix, Proc. Phys.-Math. Soc. Jpn. **22**, 264 (1940).

[131] K. W. Mahmud, L. Jiang, E. Tiesinga, and P. R. Johnson, Bloch oscillations and quench dynamics of interacting Bosons in an optical lattice, Phys. Rev. A **89**, 023606 (2014).

[132] M. J. Davis and E. J. Heller, Quantum dynamical tunneling in bound states, J. Chem. Phys. **75**, 246 (1981).

[133] R. Carretero-González, D. J. Frantzeskakis, and P. G. Kevrekidis, Nonlinear waves in Bose–Einstein condensates: physical relevance and mathematical techniques, Nonlinearity **21**, R139 (2008).

[134] R. Driben, V. V. Konotop, T. Meier, and A. V. Yulin, Bloch oscillations sustained by nonlinearity, Sci. Rep. **7**, 3194 (2017).

[135] L. D. Landau and E. Lifshitz, *Mechanics* (Butterworth-Heinemann, Oxford, 1976).

[136] J. Clarke and F. K. Wilhelm, Superconducting quantum bits, Nature **453**, 1031 (2008).

[137] M. Aspelmeyer, T. J. Kippenberg, and F. Marquardt, Cavity optomechanics, Rev. Mod. Phys. **86**, 1391 (2014).

[138] P. Kapitza, Dynamic stability of the pendulum with vibrating suspension point, Zh. Eksp. Teor. Fiz. **21**, 588 (1951).

[139] P. Weinberg, M. Bukov, L. D'Alessio, A. Polkovnikov, S. Vajna, and M. Kolodrubetz, Adiabatic perturbation theory and geometry of periodically-driven systems, Phys. Rep. **688**, 1 (2017).

[140] G. Floquet, Sur les équations différentielles linéaires à coefficients périodiques, Ann. Sci. Éc. Norm. Supér. **12**, 47 (1883).

[141] J. H. Shirley, Solution of the Schrödinger equation with a Hamiltonian periodic in time, Phys. Rev. **138**, B979 (1965).

[142] H. Sambe, Steady states and quasienergies of a quantum-mechanical system in an oscillating field, Phys. Rev. A **7**, 2203 (1973).

[143] M. Grifoni and P. Hänggi, Driven quantum tunneling, Phys. Rep. **304**, 229 (1998).

[144] A. J. Lichtenberg and M. A. Lieberman, *Regular and Chaotic Dynamics* (Springer, Berlin, 1992).

[145] B. V. Chirikov, A universal instability of many-dimensional oscillator systems, Phys. Rep. **52**, 263 (1979).

[146] H. P. Breuer and M. Holthaus, A Semiclassical theory of quasienergies and Floquet wave functions, Annals Phys. **211**, 249 (1991).

[147] W. Wustmann, Statistical mechanics of time-periodic quantum systems, PhD thesis, Dresden University of Technology, 2010.

[148] H. J. Korsch and M. Glück, Computing quantum eigenvalues made easy, Eur. J. Phys. **23**, 413 (2002).

[149] G. Birkhoff and G. Rota, *Ordinary Differential Equations* (Wiley, New York, 1978).

[150] J. K. Hale, *Ordinary Differential Equations* (Wiley, New York, 1989).

[151] M. C. Gutzwiller, *Chaos in Classical and Quantum Mechanics* (Springer, New York, 1990).

[152] I. Gradshteyn and I. Ryzhik, *Table of integrals, series, and products*, 7th ed. (Academic Press, New York, 2014).

Appendix A

A.1 Eigenstates of the Parabolic Optical Lattice

As given by Eq. (4.8), the eigenstates of the parabolic optical lattice are related to the π-periodic Mathieu functions through a Fourier transform. This equation is written as

$$\varphi_j^\ell = \begin{cases} \frac{1}{\pi}\sqrt{\frac{2}{\pi}} \int_0^\pi ce_\ell(\theta, -q) e^{-2ij\theta}\, d\theta, & \text{even} \\ \frac{1}{\pi}\sqrt{\frac{2}{\pi}} \int_0^\pi se_{\ell+1}(\theta, -q) e^{-2ij\theta}\, d\theta, & \text{odd} \end{cases}, \tag{A.1}$$

which we solve using the trigonometric Fourier expansion of Mathieu functions,

$$ce_\ell\left(\theta, -q\right) = \sum_{m=0}^{\infty} A_m^\ell(-q) \cos\left(2m\theta\right), \tag{A.2}$$

$$se_{\ell+1}\left(\theta, -q\right) = \sum_{m=0}^{\infty} B_m^{\ell+1}(-q) \sin\left(2m\theta\right), \tag{A.3}$$

such that

$$\varphi_j^\ell = \begin{cases} \frac{1}{\pi}\sqrt{\frac{2}{\pi}} \sum\limits_{m=0}^{\infty} A_m^\ell(-q) \int_0^\pi \cos(2m\theta) e^{-2ij\theta}\, d\theta, & \text{even} \\ \frac{1}{\pi}\sqrt{\frac{2}{\pi}} \sum\limits_{m=0}^{\infty} B_m^{\ell+1}(-q) \int_0^\pi \sin(2m\theta) e^{-2ij\theta}\, d\theta, & \text{odd} \end{cases}. \tag{A.4}$$

Hence, Eq. (A.1) is simplified as

$$\varphi_j^\ell = \begin{cases} \frac{1}{\sqrt{2\pi}} \sum\limits_{m=0}^{\infty} A_m^\ell(-q)\, \delta(j+m), & \text{even} \\ \frac{1}{\sqrt{2\pi}} \sum\limits_{m=0}^{\infty} B_m^{\ell+1}(-q)\, \delta(j+m), & \text{odd} \end{cases}, \tag{A.5}$$

with the coefficients $A_l^\ell(-q)$ and $B_l^{\ell+1}(-q)$ given by

$$A_m^\ell(q) = \frac{2}{\pi} \int_0^\pi ce_r(\theta, -q) \cos(2l\theta)\, d\theta, \tag{A.6}$$

$$B_m^{\ell+1}(q) = \frac{2}{\pi} \int_0^\pi se_{r+1}(\theta, -q) \sin(2l\theta)\, d\theta. \tag{A.7}$$

These are the Fourier coefficients of π-periodic Mathieu functions. The asymptotic expansions of these functions provide an analytical representation of the eigenstates and eigenenergies

[127].

A.1.1 Low Energy Solutions ($\ell < \ell_c$)

In the limit $4J \geq \Omega$, the asymptotic expansions for the eigenstates and eigenenergies in Eq. (A.4) can be expressed as [97,127]

$$\varphi_j^{(2\ell)} \approx A_\ell \exp\left[-\xi^2\left(\frac{1}{2}+\frac{3+2\ell}{16\sqrt{q}}\right)+\frac{\xi^4}{48\sqrt{q}}\right] \tag{A.8}$$

$$\times \sum_{k=0}^{\ell} h_k^{(\ell)} \xi^{2k}\left[1+\frac{(3k-k^2+10k\ell)}{24\sqrt{q}}\right], \tag{A.9}$$

$$\varphi_j^{(2\ell+1)} \approx A_\ell \exp\left\{-\xi^2\left[\frac{1}{2}+\frac{3+2\ell}{16\sqrt{q}}\right]+\frac{\xi^4}{48\sqrt{q}}\right\} \tag{A.10}$$

$$\times \sum_{k=0}^{\ell} \tilde{h}_k^{(\ell)} \xi^{2k+1}\left[1+\frac{(7k-k^2+10k\ell)}{24\sqrt{q}}\right], \tag{A.11}$$

where

$$\xi = j^{\frac{1}{4}}\frac{4}{\sqrt{q}}, \quad h_k^{(\ell)} = (-1)^\ell k 2^{2k} 2\ell!/(2k)!(\ell-k)! \tag{A.12}$$

$$\tilde{h}_k^{(\ell)} = (-1)^\ell k 2^{2k+1}(2\ell+1)!/(2k+1)!(\ell-k)! \tag{A.13}$$

and A_ℓ is a normalization constant. The coefficients $h_k^{(\ell)}$ and $\tilde{h}_k^{(\ell)}$ are associated with the Hermite polynomial $H_\ell(x)$ through

$$H_{2\ell}(x) = \sum_{k=0}^{\ell} h_k^{(\ell)} x^{2k}, \quad H_{2\ell+1}(x) = \sum_{k=0}^{\ell} \tilde{h}_k^{(\ell)} x^{2k+1}. \tag{A.14}$$

The eigenenergies are approximately given by

$$E_\ell^{\text{low}} \approx \frac{\Omega}{4}\left\{-2q+4\sqrt{q}\left(\ell+\frac{1}{2}\right)-\frac{(2\ell+1)^2+1}{8}\right. \tag{A.15}$$

$$\left.-\frac{[(2\ell+1)^3+3(2\ell+1)]}{2^7\sqrt{q}}+O\left(\frac{1}{q}\right)\right\}. \tag{A.16}$$

If higher-order corrections $1/\sqrt{q}$ and above are neglected, and only the first two terms in the eigenenergy expression are considered, the eigenstates and eigenenergies simplify to

$$E_\ell = -\frac{\Omega q}{2}+\Omega\sqrt{q}\left(\ell+\frac{1}{2}\right), \tag{A.17}$$

$$\varphi_j^{(\ell)} \approx \sqrt{\frac{\sqrt{2}}{2^\ell \ell! \sqrt{q\pi^2}}} \exp\left(-\frac{\xi^2}{2}\right) H_\ell(\xi). \tag{A.18}$$

These solutions correspond to the eigenvalues and eigenenergies (shifted by $-\Omega q/2$) of a harmonic oscillator with an effective trapping frequency ω^* and an effective mass m^*, given by

$$\hbar\omega^* = \Omega\sqrt{q} = \hbar\omega_T\sqrt{\frac{m}{m^*}}, \tag{A.19}$$

$$m^* = \frac{\hbar^2}{2Ja^2}. \tag{A.20}$$

The harmonic oscillator nature of the lowest energy eigenstates in the parabolic optical lattice is consistent with the fact that near the bottom of the Bloch band, the dispersion relation follows the free-particle form with m replaced by m^*.

A.1.2 High Energy Solutions ($\ell \geq \ell_c$)

The asymptotic expansions of eigenenergies and eigenstates in this regime are [97, 127]

$$E^{\text{high}}_{\ell=2r} \approx E^{\text{high}}_{\ell=2r-1} \approx \frac{\Omega}{4}\left\{(2r)^2 + \frac{q^2}{2[(2r)^2-1]} + \frac{q^4(7+5(2r)^2)}{32[(2r)^2-1]^3[(2r)^2-4]} + \dots\right\}, \tag{A.21}$$

$$\begin{aligned}\varphi_j^{(\text{high})\ell=2r} \approx \varphi_j^{(\text{high})\ell=2r-1} \approx A_\ell\Bigg\{ & \delta_{j,r} - \frac{q}{4}\left(\frac{\delta_{j,r-1}}{2r-1} - \frac{\delta_{j,1+r}}{1+2r}\right) \\ & + \frac{q^2}{32}\left[\frac{\delta_{j,r-2}}{(2r-2)(2r-1)} - \frac{2(1+4r^2)\delta_{j,r}}{(2r-1)^2(1+2r)^2}\right. \\ & \left. + \frac{\delta_{j,2+r}}{(1+2r)(2+2r)}\right]\Bigg\} \pm \{j \to -j\}.\end{aligned} \tag{A.22}$$

For $\ell \gg \sqrt{q}$, only the first term in Eq. (A.21) plays a significant role, which represents the well-known free-particle energies. Since free-particle wavefunctions are extended in space, their Fourier coefficients should be well-localized functions, which highlight the localization character of eigenstates in this regime.

A.2 Velocity of the Wave Packet's Mean Position

Let us consider the single band tight-binding Hamiltonian,

$$\hat{H} = -J\sum_{j=-\infty}^{\infty}(\hat{a}_j^\dagger \hat{a}_{j+1} + \text{h.c.}) + \Omega\sum_{j=-\infty}^{\infty} j^2\, \hat{a}_j^\dagger \hat{a}_j. \tag{A.23}$$

Introducing the transformation operator,

$$\hat{U}(t) = e^{i(\Omega \sum_j j^2\, \hat{a}_j^\dagger \hat{a}_j)t/\hbar}, \tag{A.24}$$

which follows,

$$\hat{U}^\dagger(t)\; \hat{a}_j\; \hat{U}(t) = \hat{a}_j\; e^{i(\Omega\, j^2\, \hat{a}_j^\dagger \hat{a}_j)t/\hbar}, \tag{A.25}$$

and

$$\hat{U}^\dagger(t)\; \hat{H}\; \hat{U}(t) = i\hbar\frac{\partial}{\partial t} + \Omega\sum_j j^2\, \hat{a}_j^\dagger \hat{a}_j. \tag{A.26}$$

Using the identities,

$$\hat{a}_j(t) = e^{\frac{i}{\hbar}(\Omega j^2)t}\hat{a}_j(t) \qquad ; \qquad \hat{a}_{j+1}(t) = e^{\frac{i}{\hbar}(\Omega(j+1)^2)t}\hat{a}_{j+1}(t) \tag{A.27}$$

the Hamiltonian (A.23) is expressed as,

$$\hat{H}'(t) = -J\sum_j \left(\hat{a}_{j+1}^\dagger \hat{a}_j\; e^{-\frac{i}{\hbar}(2\Omega j)t} + \text{h.c.}\right). \tag{A.28}$$

Expressing the field operators in terms of Wannier states the above hamiltonian can be written as

$$\hat{H}'(t) = -J\sum_j \left(|j+1\rangle\langle j|\; e^{-\frac{i}{\hbar}(2\Omega j)t} + |j\rangle\langle j+1|\; e^{\frac{i}{\hbar}(2\Omega j)t}\right). \tag{A.29}$$

Let us define the operators,

$$\hat{k}(t) = \sum_j |j\rangle\langle j+1| e^{\frac{i}{\hbar}(2\Omega j)t}, \qquad \hat{k}(t)|j\rangle = |j-1\rangle e^{\frac{i}{\hbar}(2\Omega j)t}, \tag{A.30}$$

and

$$\hat{x} = a\hat{\mathrm{J}} = a\sum_j j\; |j><j|, \tag{A.31}$$

which leads us to redefine the Hamiltonian (A.29) is rewritten as,

$$\hat{H}(t) = -J[\hat{k}(t) + \hat{k}^\dagger(t)]. \tag{A.32}$$

Using the commutators,

$$[\hat{k}(t),\; \hat{\mathrm{J}}] = \hat{k}(t), \qquad [\hat{k}^\dagger(t),\; \hat{\mathrm{J}}] = \hat{k}^\dagger(t), \qquad [\hat{k}(t),\; \hat{k}^\dagger(t)] = 0. \tag{A.33}$$

The time evolution of the position operator is given by,

$$\hat{x}^o = \frac{i}{\hbar}[\hat{H}(t),\; \hat{x}], \tag{A.34}$$

$$\hat{x}^o = -\frac{iJ}{\hbar}[\{\hat{k}(t) + \hat{k}^\dagger(t)\},\ a\hat{\mathsf{J}}], \tag{A.35}$$

$$v(t) = -\frac{iJa}{\hbar}[\hat{k}(t),\ \hat{\mathsf{J}}] - \frac{iJa}{\hbar}[\hat{k}^\dagger(t),\ \hat{\mathsf{J}}], \tag{A.36}$$

$$= -\frac{iJa}{\hbar}\hat{k}(t) - \frac{iJa}{\hbar}\{-\hat{k}^\dagger(t)\}, \tag{A.37}$$

$$= \frac{iJa}{\hbar}\{\hat{k}^\dagger(t) - \hat{k}(t)\}, \tag{A.38}$$

$$= \frac{iJa}{\hbar}\{\hat{k}^\dagger(t) - \hat{k}(t)\}, \tag{A.39}$$

$$v(t) = \frac{iJa}{\hbar}\sum_j (|j+1>< j|\ e^{-\frac{i}{\hbar}(2\Omega j)t} + h.c.). \tag{A.40}$$

Thus, we have the time-dependent velocity,

$$v(t) = \frac{2Ja}{\hbar}\ Im\left[\sum_j (|j+1>< j|\ e^{-\frac{i}{\hbar}(2\Omega j)t})\right]. \tag{A.41}$$

We calculate the mean velocity as

$$\bar{v}(t) = \frac{2Ja}{\hbar}\left[Im\left(\sum_j \langle\psi(0)|j+1\rangle\ \langle j|\psi(0)\rangle e^{-\frac{i}{\hbar}(2\Omega j)t}\right)\right], \tag{A.42}$$

$$\bar{v}(t) = \frac{2Ja}{\hbar}\left[Im\left(\sum_{j,k',k} \langle\psi(0)|k'\rangle\langle k'|j+1\rangle\ \langle j|k\rangle\langle k|\psi(0)\rangle e^{-\frac{i}{\hbar}(2\Omega j)t}\right)\right], \tag{A.43}$$

$$\bar{v}(t) = \frac{2Ja}{\hbar}\left[Im\left(\sum_{j,k',k} \langle\psi(0)|k'\rangle\ \left(\frac{a}{2\pi}e^{-ik'a}\ e^{-ijk'a}\ e^{ijkd}\right)\ \langle k|\psi(0)\rangle\ e^{-\frac{i}{\hbar}(2\Omega j)t}\right)\right], \tag{A.44}$$

$$\bar{v}(t) = \frac{2Ja}{\hbar}\left[Im\left(\sum_{j,k',k} \langle\psi(0)|k'\rangle\left(\frac{a}{2\pi}e^{ija\left(k-k'-\frac{2\Omega}{\hbar a}t\right)}\right)\langle k|\psi(0)\rangle e^{-ik'a}\right)\right], \tag{A.45}$$

$$\bar{v}(t) = \frac{2Ja}{\hbar}\left[Im\left(\sum_{k',k}\langle\psi(0)|k'\rangle\delta\left(k-k'-\frac{2\Omega}{\hbar a}t\right)\langle k|\psi(0)\rangle e^{-ik'a}\right)\right]. \tag{A.46}$$

This implies $k' = k - 2\Omega t/\hbar a$ by which the above equation reduces to

$$\bar{v}(t) = \frac{2Ja}{\hbar}\left[Im\left(\sum_k \langle\psi(0)|k - 2\Omega t/\hbar a\rangle\ \langle k|\psi(0)\rangle\ e^{-ika}\ e^{-\frac{i}{\hbar}2\Omega t}\right)\right], \tag{A.47}$$

$$\bar{v}(t) = \frac{2Ja}{\hbar}\left[Im\left(\sum_{k,j',j}\ \psi^{\dagger}_{j'}\psi_j\langle j'|k-2\Omega t/\hbar a\rangle\ \langle k|j\rangle\ e^{-ika}\ e^{-\frac{i}{\hbar}2\Omega t}\right)\right], \tag{A.48}$$

$$\bar{v}(t) = \frac{2Ja}{\hbar}\left[Im\left(\sum_{k,j',j}\psi^{\dagger}_{j'}\psi_j\left(\frac{a}{2\pi}e^{ij'a(k-\frac{2\Omega}{\hbar a}t)}e^{-ijka}e^{-ika}e^{-\frac{i}{\hbar}2\Omega t}\right)\right)\right], \tag{A.49}$$

$$\bar{v}(t) = \frac{2Ja}{\hbar}\left[Im\left(\sum_{j',j}\ \psi^{\dagger}_{j'}\psi_j\ \left(\frac{a}{2\pi}\ \sum_{k}e^{ik(j'-j-1)}\ e^{-\frac{i}{\hbar}2\Omega t(j'-1)}\right)\right)\right], \tag{A.50}$$

$$\bar{v}(t) = \frac{2Ja}{\hbar}\left[\mathrm{Im}\left(\sum_{j',j}\psi^{\dagger}_{j'}\psi_j\delta(j'-j-1)e^{-\frac{i}{\hbar}2\Omega t(j'-1)}\right)\right]. \tag{A.51}$$

Thus $j' = j+1$ and the above equation simplifies to

$$\bar{v}(t) = \frac{2Ja}{\hbar}\left[Im\left(\sum_{j}\ \psi^{\dagger}_{j+1}\ \psi_j\ \ e^{-\frac{i}{\hbar}(2\Omega j)t}\right)\right]. \tag{A.52}$$

Let us take

$$|\psi(0)\rangle = \sum_j \psi_j|j\rangle, \tag{A.53}$$

with

$$\psi_j = e^{-\left(\frac{(j-j_o)^2}{\sigma_0^2}+ik_0aj\right)}, \tag{A.54}$$

which is normalized to unity. With this, the order parameter is

$$\psi^{\dagger}_{j+1}\psi_j = e^{-\left(\frac{(j-j_o+1)^2+(j-j_o)^2}{2\sigma_0^2}\right)}e^{-ik_0a}, \tag{A.55}$$

and thus

$$\bar{v}(t) = -\frac{2Ja}{\hbar}\left[\sum_j e^{-\left(\frac{2(j-j_0)^2+2(j-j_0)+1}{2\sigma_0^2}\right)}\sin\left(k_0a+\frac{2\Omega t}{\hbar}j\right)\right]. \tag{A.56}$$

Taking $m = j - j_0$ the above equation is rewritten as

$$\bar{v}(t) = -\frac{2Ja}{\hbar}\left[\sum_{m=-\infty}^{\infty} e^{-\left(\frac{2m^2+2m+1}{2\sigma_0^2}\right)}\sin\left(k_0a+\frac{2\Omega t}{\hbar}(m+j_0)\right)\right], \tag{A.57}$$

where $m = j - j_0$. Approximating the summation over spatial index m by an integral and using the standard integral [152],

$$\int_{-\infty}^{\infty} e^{-(ax^2+2bx+c)}\sin\left(px^2+2qx+r\right)dx = \frac{\sqrt{\pi}}{(a^2+p^2)^{\frac{1}{4}}}\ e^{\left(\frac{a(b^2-ac)-(aq^2-2bpq+cp^2)}{a^2+p^2}\right)}$$

$$\times \sin\left(\frac{1}{2}\arctan\frac{p}{a} - \frac{p(q^2-pr)-(pb^2-2abq+a^2r)}{a^2+p^2}\right), \tag{A.58}$$

the above equation is simplified as,

$$\bar{v}(t) \approx -\frac{2\sqrt{\pi}Jd\sigma_0}{\hbar}e^{-\left(\frac{\Omega^2\sigma_0^2}{\hbar^2}t^2-\frac{1}{2\sigma_0^2}\right)}\sin\left(k_0a+\frac{2\Omega j_0}{\hbar}t\right), \tag{A.59}$$

where $\nu = 2\Omega j_0/\hbar$ is the frequency of oscillations.

Danksagung:

I would like to express my deepest gratitude to **Prof. Dr. Torsten Meier** for giving me the opportunity to work on my PhD project in his Computational Optoelectronics and Photonics research group. His excellent supervision, continuous guidance, expert advice, unmatched patience, and unwavering support have played a pivotal role in shaping my work. I am especially thankful for his kind and supportive nature, which made my time in his group both productive and enjoyable. His assessments and ideas on physical problems of all kinds always helped me a lot and often gave me the impetus for new approaches.

Since an early stage of my doctoral studies, I have been fortunate to receive dedicated guidance from **Prof. Dr. Martin Holthaus**. His extensive experience and insightful discussions have greatly enriched my work. I would like to express my heartfelt gratitude for his invitations to Oldenburg, which initiated many extremely fruitful discussions on important topics of research. His holistic view of the field, keen assessment of results, and ability to refine and highlight key perspectives have been truly unmatched. I would like to express my deep gratitude to him for his invaluable support.

Also, I thank **Prof. Dr. Hans Jürgen Korsch** for answering my questions and providing important guidance throughout my research career. I would also like to sincerely thank **PD Dr. Axel Pelster** for the insightful discussions that introduced me to new research directions and applications of my work.

I wish to convey thanks to my colleagues **Dr. Christian Offen** and **Dr. Boris Wembe** in the Department of Mathematics, Paderborn University, for providing me with an introduction to advanced computational approaches. Their guidance has been instrumental in making accurate computations within short times.

A heartfelt thank you to **Dr. Didier Belobo Belobo** for his encouragement, thought-provoking discussions, and academic guidance, which have been a significant source of motivation.

I would also like to extend my deep appreciation to all of my group members, who helped cultivate a friendly and collaborative research environment, making my time as a PhD student all the more enjoyable. My sincere gratitude to **Dr. Matthias Reichelt** for his thoughtful guidance during my initial numerical computations, **Dr. Denis Kopylov** for stimulating discussions, and **Dr. Hendrik Rose** for thoughtful conversations in different research areas.

I thank **Ms. Simone Lange**, the group's secretary, for her kindness and unwavering administrative support, which allowed me to concentrate more effectively on my research.

I further extend my gratitude to **DAAD and Paderborn University** for their financial support through a PhD scholarship and for covering conference travel, thesis printing, and publication costs. Their support has played a crucial role in my professional and academic development. I also thank the **Paderborn Center for Parallel Computing (PC^2)** for providing essential computational resources that greatly facilitated my research.

Finally, I should extend my heartfelt gratitude to my family and my wife for their unconditional love, patience, and support. It is the encouragement shown by them that has become my strength in overcoming challenges and staying inspired during this entire journey.